



Universiteit Utrecht

INSTITUTE FOR THEORETICAL PHYSICS

MASTER'S THESIS

Electronic structure calculations of in-plane bent graphene nanoribbons

Author:
SIMON STUIJ

Supervisors:
PROF. CRISTIANE MORAIS SMITH
DR. VLADIMIR JURIČIĆ

APRIL 1, 2015

Abstract

The electronic properties of graphene are influenced by both geometric confinement and strain. In this thesis, we study the electronic structure of in-plane bent graphene nanoribbons, a confined strained graphene system. We develop a tight-binding model that has a small computational cost and is based on three parameters: hopping, overlap and an exponential decay rate. This model predicts that the bandgap of armchair graphene nanoribbons after bending behaves similarly to the bandgap after a uniform longitudinal strain, and in general is not very sensitive to bending. However, it also predicts that the edge states within zigzag graphene nanoribbons are sensitive to bending and develop an effective 1D chain dispersion. Because the slope of the dispersion is connected to the velocity of the electrons at the edge, this means that the edge states change from localized to delocalized upon increasing the degree of bending. We also take the first steps in an analysis of bent graphene nanoribbons using the massless Dirac fermion continuum description of graphene by combining boundary conditions and a pseudo-magnetic field.

Contents

1	Introduction	1
2	Electronic structure of graphene	5
2.1	Graphene: carbon in a honeycomb lattice	5
2.2	Tight-binding model of graphene	6
3	Electronic structure of graphene nanoribbons	15
3.1	Geometry of graphene nanoribbons	15
3.2	Tight-binding model of graphene nanoribbons	16
4	Electronic structure of bent graphene nanoribbons	22
4.1	Geometry of bent graphene nanoribbons	22
4.2	Tight-binding model of bent graphene nanoribbons	28
4.3	Spectra of bent graphene nanoribbons and comparison with uniform strain	29
4.4	Bent armchair ribbons: Band-gap behaviour	37
4.5	Bent zigzag ribbons: Edge state dispersion	39
5	Continuum model for bent graphene nanoribbons	45
5.1	Dirac fermions in graphene	45
5.2	Dirac fermions in straight ribbon geometry	47
5.3	Dirac equation with pseudo-magnetic field	51
6	Conclusions and outlook	60
6.1	Conclusions	60
6.2	Outlook	62
	Appendices	64
A	Relation between orbital- and orthogonal-hopping parameters in graphene	65
B	Comparing the spectra of graphene, periodic ribbons and finite ribbons	67

<i>CONTENTS</i>	iii
C Bloch's theorem for lattice-preserving deformations	73
Bibliography	76

Chapter 1

Introduction

Ever since the synthesis of graphene by Geim and Novoselov in 2004, graphene has been hailed as a wonder material both on a fundamental level for its unique properties and because of its potential applications [1, 2]. Interest has not waned, as can for instance be seen from the continuing stream of publications, increasing number of centers dedicated to graphene research, startup companies and big funding schemes such as the graphene flagship.

Many of graphene's remarkable features stem from two facts. The first is that graphene's charge carriers have a linear dispersion for low energy and can be effectively described as Dirac fermions. The other fact is that graphene is a two-dimensional ultra thin membrane. In this thesis, we study the interplay between these two properties through a specific case: in-plane bent graphene nanoribbons (GNRs). A study of this specific system fits naturally in two somewhat separate areas of research in graphene.

The first is the study of GNRs. GNRs were already studied before the advent of graphene through research inspired by carbon nanotubes (CNTs). The electronic properties of GNRs are very sensitive to their termination. In particular, zigzag graphene nanoribbons (ZGNRs) show localised edge states with interesting properties [3]. More general is the development of a bandgap for all ribbons, though the size and cause of this bandgap exhibit an interesting dependence on the termination and width of the ribbon [4]. Because of their bandgap, GNRs have been proposed as a potential material for electronics and have been used to create a field-effect transistor out of graphene [5].

The second research area to which bent GNRs are related is the study of deformations in graphene. Interest in this topic originated mainly from the theoretical prediction that strain couples as a pseudo magnetic field (a magnetic field that preserves time-reversal symmetry) to the Dirac fermions of graphene. This was initially studied in the light of deformations in CNTs [6]. After the rise of graphene, this field grew in prominence by the vision of using strain as a way to tune graphene's properties and use it in developing an all-graphene electronics. This pursuit is called strain engineering [7]. Experi-

mental evidence of the pseudo-magnetic field was found by the observation of “pseudo”-Landau levels in strained graphene [8].

Graphene systems that are both geometrically confined and strained, thus combining these two research areas, have recently been studied with a focus on the resulting mechanical properties [9]. In this study, the paper-art analogy that exist for graphene (see Fig. 1.1) is taken to include *kirigami*. This analogy describes the study of straight GNRs as the art of *paper cutting* graphene. Graphene *origami* (the traditional Japanese art of folding paper) is the study of strain in graphene. These two come together in graphene *kirigami* in which both cutting and folding is allowed. A bent GNR is a very specific and not so complicated type of graphene *kirigami*, but because it is a relatively simple system, it is possible to study its electronic properties in depth. For this reason, the system is a good probe to understand how electronic effects that arise from confinement and termination of graphene combine with effects from strain. Another motivation to study this system is that more complicated graphene *kirigami* could consist in part of bent GNRs. Knowing what is to be expected in this simple case, therefore, helps to understand more complicated graphene *kirigami*.

The direct inspiration to study the specific case of bent GNRs was the experimental synthesis of such a ribbon in an affiliated research group, see Fig. 1.2. Their research consisted of growing an armchair graphene nanoribbon (AGNR) which had 14 carbon atoms in its unit cell. Using the tip of an atomic-force microscope, they were able to bent the ribbon by pushing one end of the ribbon. Electronic transport measurements were made before and after bending using a scanning tunneling microscope. From these measurements, a dependence of the bandgap with respect to the bending angle could be deduced. Though the preliminary results require further confirmation by performing more measurements, they found that the bandgap decreases slightly with bending (Fig. 1.2). This thesis is not meant as an analysis of these results, as they have been carefully discussed in Ref. [12] and also agree with first-principle predictions from Ref. [13].

Instead the goal of this thesis is to investigate more broadly the effects of bending on GNRs and we will not limit ourselves to one specific GNR. We will, however, only consider the effects on the electronic band structure. The band structure will primarily be calculated using a tight-binding model that takes three parameters into account: hopping, overlap, and a decay parameter. This, as we will argue, represents a minimal model that can describe bent GNRs. Next to that, we attempt to describe the electronic structure using an effective Dirac-fermion continuum description of graphene.

This thesis is organised as follows. In Chapter 2 and Chapter 3 we review the electronic structure of graphene and GNRs using tight-binding theory. Chapter 4 is the main chapter of this thesis, where the electronic structure of bent GNRs is studied using tight-binding theory. Specifically, we look at the effect on the bandgap structure for AGNR and at the effect on the edge states

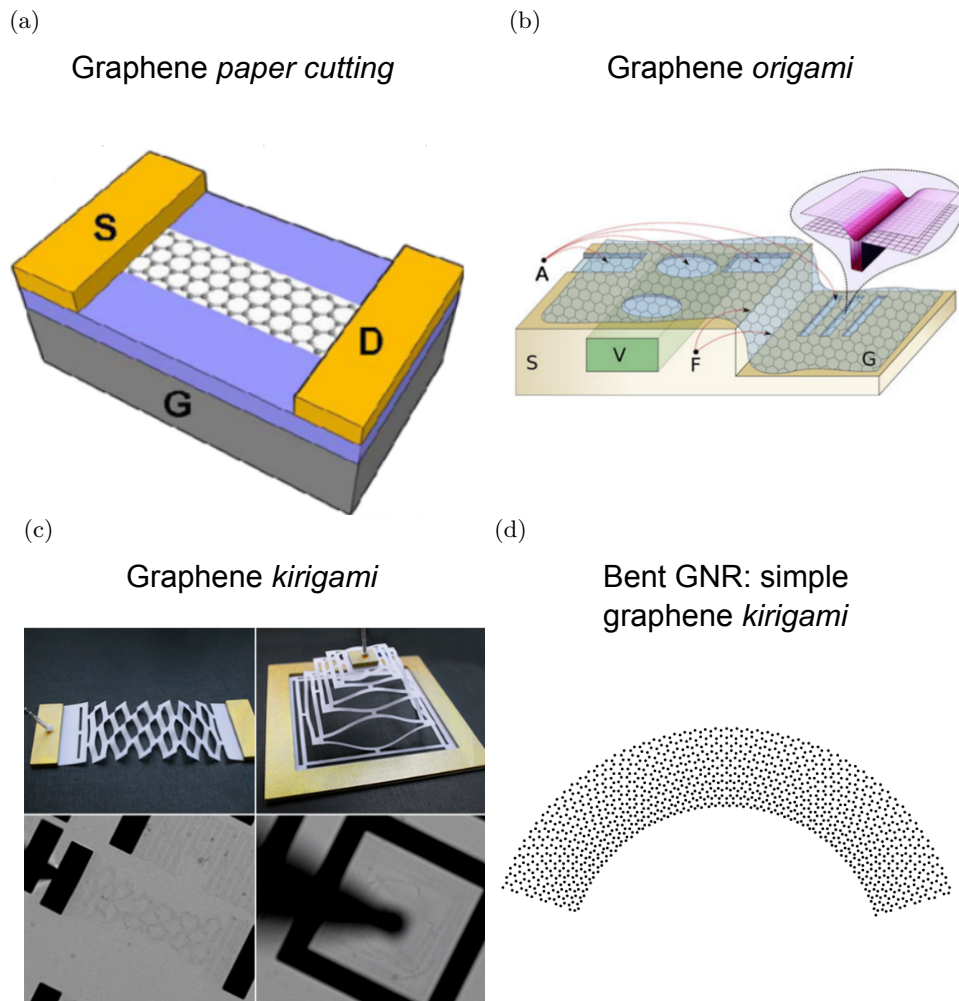


Figure 1.1: (a) A graphene transistor made from GNRs (cut graphene), figure adapted from Ref. [5]. (b) Strain engineering (graphene origami) by patterning the substrate, figure adapted from Ref. [7]. (c) Mechanical response of cut and stretched graphene (graphene kirigami) [9][10], figure adapted from Ref. [11] (d) A bent GNR, a simple building block of graphene kirigami and the system we will study in this thesis.

for ZGNR. An important result is an emerging band structure for the edge states that results from bending. In Chapter 5, we study bent graphene ribbons using the effective Dirac theory of graphene. This theory is first reviewed for graphene and GNRs, in which the Dirac equation is supplemented with appropriate boundary conditions. Then, an attempt is made to combine it with the gauge field method for describing strained graphene with the boundary conditions to describe bent GNRs. At this stage, however, it is not clear

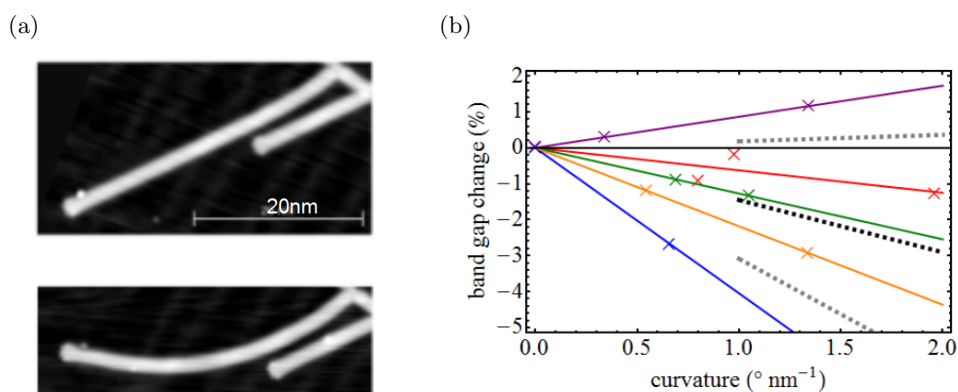


Figure 1.2: (a) Experimental realization of an in-plane bent GNR (armchair ribbon with 14 atoms in the unit cell), adapted from Ref. [12] (b) Band gap dependence on bending for 5 ribbons; crosses are data points from the measurements and lines are linear fittings through the data points. Different color represent different ribbons (black line at zero is axes). The thick black dotted line is the average of the 5 ribbons and the thin dotted lines are the standard deviation. Bending is measured in units of degree nm^{-1} (the amount of degrees 1 nm of ribbon is curved).

to what extent this combination is appropriate. Conclusion are provided in Chapter 6.

Chapter 2

Electronic structure of graphene

This chapter reviews the electronic structure of graphene using tight-binding theory. First, the lattice geometry of graphene is introduced. Then, a tight-binding theory with orthogonal basis states is considered. Next, we study graphene in a tight-binding theory with non-orthogonal basis states. We argue that a minimal model that can be expected to give reasonable results for bent GNRs uses non-orthogonal basis states and exponentially decaying parameters.

2.1 Graphene: carbon in a honeycomb lattice

Graphene, a 2D allotrope of carbon, consists of carbon atoms arranged in a honeycomb lattice. The configuration of the electrons in a carbon atom is $1s^2 2s^2 2p^2$. The four electrons in the second shell are valence electrons, which can hybridize. In graphene, these electrons hybridize into 3 sp^2 orbitals that form covalent σ bonds. These σ bonds are triangular and are responsible for the honeycomb structure of graphene. The remaining valence electron is in the p_z orbital, which points perpendicularly to the lattice plane and forms π bonds.

A honeycomb consists of two inequivalent triangular sublattices, labeled A and B , see Fig.2.1a. The sublattice sites are connected to each other by the nearest neighbor (NN) vectors. For the orientation chosen here, these are given by $\delta_1 = \frac{a}{2}(1, \sqrt{3})$, $\delta_2 = \frac{a}{2}(1, -\sqrt{3})$ and $\delta_3 = -a(1, 0)$, with $a = 0.142$ nm denoting the distance between NNs. The lattice vectors of the honeycomb are given by $\mathbf{a}_1 = \frac{a}{2}(3, \sqrt{3})$ and $\mathbf{a}_2 = \frac{a}{2}(3, -\sqrt{3})$, which form a triangular Bravais lattice. We can define a unit cell with a diamond shape enclosing two inequivalent sublattice sites, see Fig.2.1a. We use lower case, \mathbf{r}_i , for sites of the honeycomb lattice with $i \in 1, \dots, \bar{N}$ and \bar{N} the number of lattice sites in the honeycomb. We will use upper case, \mathbf{R}_l , for sites of the Bravais lattice

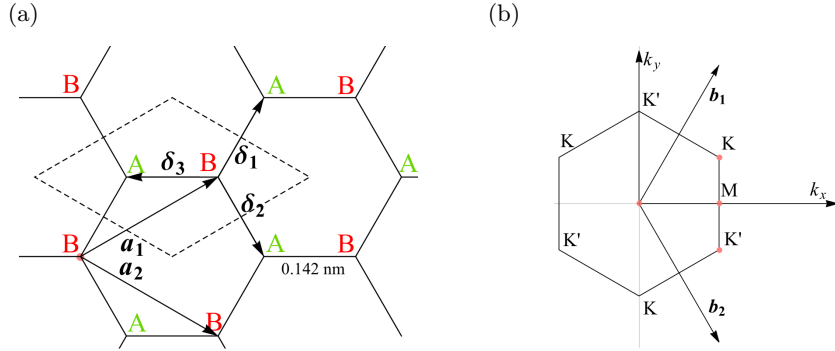


Figure 2.1: (a) The graphene honeycomb lattice. Depicted are the diamond shaped unit cell, lattice vectors and nearest-neighbor vectors. (b) Reciprocal space, showing the reciprocal lattice vectors and the hexagonal first Brillouin zone of the triangular Bravais lattice.

with $l \in 1, \dots, N$ and $N = \bar{N}/2$. Thus, if \mathbf{r}_i is an A lattice site $\mathbf{r}_i = \mathbf{R}_l + \delta_A$ and if $\mathbf{r}_{i'}$ is a B lattice site $\mathbf{r}_{i'} = \mathbf{R}_{l'} + \delta_B$. Here $\delta_{A/B}$ is the position of the A/B lattice site in the unit cell. We will assume that the origin of our coordinate system coincides with the first Bravais lattice site and the A sublattice site such that $\delta_A = (0, 0)$ and $\delta_B = -\delta_3$.

The reciprocal lattice vectors are given by $\mathbf{b}_1 = \frac{2\pi}{3a}(1, \sqrt{3})$ and $\mathbf{b}_2 = \frac{2\pi}{3a}(1, -\sqrt{3})$. From these, we can determine the Brillouin zone (BZ), which turns out to be a hexagon, see Fig. 2.1b. The corners of the hexagon can be divided into two inequivalent sets of points K and K' , which can be represented by the vectors $K_{\pm} = \pm(\mathbf{b}_1 - \mathbf{b}_2)/3$.

2.2 Tight-binding model of graphene

The electronic properties of graphene are dominated by the electrons in the π bonds that are due to the p_z atomic orbitals. This suggests that we can effectively describe the band structure by a tight-binding model of electrons restricted to a single state per honeycomb site. In most standard treatments of tight-binding in graphene, the dispersion relation is derived from a second-quantized Hamiltonian [14]. We first use this approach to derive the spectrum for orthogonal basis states. However, it turns out to be useful to derive the spectrum also from non-orthogonal basis states. It is more convenient to do this starting from a first-quantized Hamiltonian.

Tight-binding model using orthogonal basis states

For a general number of hopping parameters, the second-quantized tight-binding Hamiltonian takes the form

$$H = \sum_{n,n'} \left[\sum_{\langle l,l' \rangle_n} \bar{t}_n (a_l^\dagger b_{l'} + b_{l'}^\dagger a_l) + \sum_{\langle\langle l,l' \rangle\rangle_n} \bar{t}'_n (a_l^\dagger a_{l'} + b_l^\dagger b_{l'}) \right] + \sum_l \bar{\epsilon}_0 (a_l^\dagger a_l + b_l^\dagger b_l). \quad (2.1)$$

Here, a_l^\dagger and b_l^\dagger are creation operators that, respectively, create basis states $|a_l\rangle$ and $|b_l\rangle$ associated with the A and B sublattice site at l . The sum over $\langle l,l' \rangle_n$ runs over those Bravais lattice points l and l' , for which the A and B sublattices are d_n apart, where d_n is the n -th inter-sublattice distance, i.e. $|\mathbf{R}_{l'} + \delta_B - \mathbf{R}_l - \delta_A| = d_n$. The sum over $\langle\langle l,l' \rangle\rangle_n$ runs over those Bravais lattice points l and l' , for which sites at the A sublattice are d'_n apart, where d'_n is the n -th intra-sublattice distance, i.e. $|\mathbf{R}_l - \mathbf{R}_{l'}| = d'_n$ (equivalently for B). We have singled out the on-site energies ϵ_0 , therefore, d'_n is taken to be larger than zero. We assume here that there is no difference between hopping from A to B or from B to A , nor is there a difference in the on-site energy between A and B . This follows from the symmetry of the honeycomb lattice under sublattice exchange.

Usually, the creation operators are taken to create orthogonal basis states and satisfy the standard fermionic anticommutation relations. This approach has the advantage of being quickly solvable by the Fourier transformation,

$$a_l = \frac{1}{\sqrt{N}} \sum_{1BZ} \alpha_{\mathbf{k}} e^{i\mathbf{R}_l \cdot \mathbf{k}}, \quad b_l = \frac{1}{\sqrt{N}} \sum_{1BZ} \beta_{\mathbf{k}} e^{i\mathbf{R}_l \cdot \mathbf{k}}, \quad (2.2)$$

where we have introduced the crystal momentum \mathbf{k} . The sum runs over the first Brillouin zone denoted by $1BZ$. Note that we adopt the convention of using the same phase for defining the a_l and the b_l Fourier transform [15]. We can now rewrite the Hamiltonian (2.1) in terms of the $\alpha_{\mathbf{k}}$ and $\beta_{\mathbf{k}}$ operators and introduce a one-particle state

$$|\bar{\psi}(\mathbf{k})\rangle = (\bar{A}_{\mathbf{k}} \alpha_{\mathbf{k}}^\dagger + \bar{B}_{\mathbf{k}} \beta_{\mathbf{k}}^\dagger) |0\rangle. \quad (2.3)$$

Here, $\bar{A}_{\mathbf{k}}$ and $\bar{B}_{\mathbf{k}}$ are functions of the crystal momentum and $|0\rangle$ is the vacuum state. The Schrödinger equation $H |\bar{\psi}(\mathbf{k})\rangle = \bar{E} |\bar{\psi}(\mathbf{k})\rangle$ can then be written as a matrix eigenvalue problem,

$$\begin{pmatrix} \bar{H}'(\mathbf{k}) & \bar{H}(\mathbf{k}) \\ \bar{H}^*(\mathbf{k}) & \bar{H}'(\mathbf{k}) \end{pmatrix} \begin{pmatrix} \bar{A}_{\mathbf{k}} \\ \bar{B}_{\mathbf{k}} \end{pmatrix} = \bar{E}_{\mathbf{k}} \begin{pmatrix} \bar{A}_{\mathbf{k}} \\ \bar{B}_{\mathbf{k}} \end{pmatrix}, \quad (2.4)$$

with

$$\begin{aligned} \bar{H}(\mathbf{k}) &= \sum_n \bar{t}_n f_n(\mathbf{k}), & f_n(\mathbf{k}) &= \sum_{\langle l \rangle_n} e^{-i\mathbf{k} \cdot \mathbf{R}_l}, \\ \bar{H}'(\mathbf{k}) &= \sum_n \bar{t}'_n g_n(\mathbf{k}), & g_n(\mathbf{k}) &= \sum_{\langle\langle l \rangle\rangle_n} e^{-i\mathbf{k} \cdot \mathbf{R}_l}. \end{aligned} \quad (2.5)$$

Here, the sum over $\langle l \rangle_n$ runs over inter sublattice pairs, these are l such that $|\mathbf{R}_l + \delta_B - \delta_A| = d_n$. The sum over $\langle\langle l \rangle\rangle_n$ runs over intra sublattice pair, these are l such that $|\mathbf{R}_l| = d'_n$. Solving this matrix equation yields the dispersion,

$$\bar{E}_{\mathbf{k}}^\lambda = \bar{H}'(\mathbf{k}) + \lambda|\bar{H}(\mathbf{k})| + \bar{\epsilon}_0. \quad (2.6)$$

The eigenstates corresponding to the dispersion relation (2.6) are given by those $\bar{\psi}_{\mathbf{k}}$ for which $\bar{A}_{\mathbf{k}} = \frac{\bar{H}(\mathbf{k})}{|\bar{H}(\mathbf{k})|} \bar{B}_{\mathbf{k}}$.

Studies have been done in which the hopping parameters between orthogonal states are fitted against ab-initio calculations [16]. A dispersion using these parameters reproduces first-principle calculations very well, as will later be demonstrated. We would, however, like to use a model that is as simple as possible.

A way to reduce the complexity is to take only NN and next nearest-neighbor (NNN) hopping into account. In that case, the dispersion reduces to,

$$\bar{E}_{\mathbf{k}}^\lambda = -3\bar{t}' + \bar{t}'|\gamma_{\mathbf{k}}|^2 + \lambda|\bar{t}\gamma_{\mathbf{k}}| + \bar{\epsilon}_0. \quad (2.7)$$

Here $t(t')$ is the (N)NN hopping parameter and $\gamma_{\mathbf{k}} = 1 + e^{i\mathbf{k}\cdot\mathbf{a}_1} + e^{i\mathbf{k}\cdot\mathbf{a}_2}$. This dispersion is often found in the literature because it captures the most important features of the graphene dispersion, i.e. the linear dispersion and the intra-sublattice hopping that breaks the electron-hole symmetry. There is currently, however, no clear consensus of what hopping parameters to take for the orthogonal dispersion with NN and NNN hopping. One convention is to take $\bar{t} = -2.8$ eV and $-0.02\bar{t} \leq \bar{t}' \leq -0.2\bar{t}$ [14]. We will use the values $\bar{t} = -3.00236$ eV and $\bar{t}' = 0.20509$ eV [16].

The dispersion of graphene along a line connecting high-symmetry points is shown in Fig. 2.2. In this figure, different graphene dispersions and choices of hopping parameters are compared. One can observe the two-parameter orthogonal model of Eq. (2.7) and also the dispersion of Eq. (2.6), where the first 15 hopping parameters of Ref. [16] are used. For both orthogonal bases, $\bar{\epsilon}_0$ has been chosen such that the zero energy is reached at the K and K' points. The figure also depicts the energy dispersion from a first-principle calculation of graphene that was made using QuantumWise software [17]. From the figure we can observe that the 15 parameter orthogonal basis model reproduces very well the dispersion relation obtained by first-principle calculations. The two-parameter orthogonal model captures the essential features, but differs markedly at the M point for the chosen parameters. A fourth dispersion, based on non-orthogonal basis states and exponentially decaying parameters, is also depicted. We will introduce and discuss this dispersion in the next section.

Now, we discuss whether this two-parameter model is convenient to study bent GNRs. To study bent GNRs in a tight-binding scheme, there are two criteria that are important:

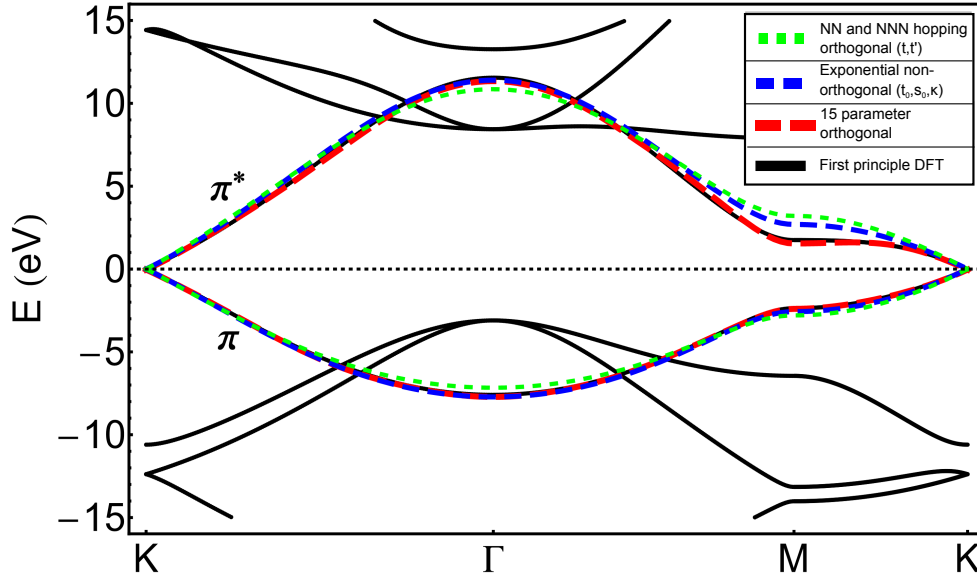


Figure 2.2: Several plots of the dispersion relation for graphene along the line connecting the $\Gamma - M - K - \Gamma$ points. The dashed (shortest dashes) green curve corresponds to the two-parameter orthogonal dispersion given by Eq. (2.7). The NN and NNN hopping parameters are $t = -3.00236$ eV and $t' = 0.20509$ eV, and $\bar{\epsilon}_0$ has been chosen such that the K points are at zero energy. The blue dashed (longer dashes) curve depicts the orbital dispersion with exponentially decaying hopping and overlap parameter, given by Eq. (2.18). We assumed exponential decay for the hopping and overlap parameters, described by Eq. (2.21), with values $t_0 = -2.8$ eV, $s_0 = 0.2$, $\kappa = 2.6$, and $\epsilon_0 = -1.28$ eV, chosen so that the zero energy is at the K points. The black dashed curve with smaller dashes corresponds to an orthogonal-basis dispersion taking into account the first 15 hoppings [16]. The continuous black line corresponds to first-principle calculations, made using the QuantumWise software [17].

1. The model should use parameters that are still valid when a system is geometrically confined, i.e. when graphene is confined to a GNR.
2. We need a relation between the distance between two sites and the hopping parameter between them in order to describe the effect of strain.

As the model is presented above, the second criteria is obviously not satisfied. However, we could introduce some kind of function that would describe how the NN and NNN hopping depend on the distance. An exponential decay has been used, for instance, in Ref. [18]. One confusing issue in this case is, however, that usually the NNN and NN are taken to be opposite sign. Therefore, an exponential decay does not connect the NN and NNN hopping

parameter (this issue was avoided in Ref. [18] by only considering absolute sizes). In fact, checking the orthogonal hopping-parameters of Ref. [16], which are given up to the first 20 neighbors, one can see that these do not satisfy an exponential decay very well, as the signs are not always the same and some more distant hopping-parameters are larger than nearer ones.

However, a more serious problem occurs when we consider the first criterium. Indeed, it is not reasonable to expect that these two hopping parameters will remain the same for sites closer to the edge of the ribbon. To understand this point, we recall that the orthogonal hopping parameters can be expressed in terms of integrals over space of the orthogonal basis functions and the lattice potential. Because of their orthogonality, these states do not represent the p_z orbitals of the different lattice sites. It is however possible to construct a set of orthogonal states from linear combinations of the p_z orbitals that keeps their localized character by using the Löwdin orthogonalization scheme [19]. One can calculate these Löwdin orthogonalized states. They will be identical at each lattice site because of the translational symmetry of the graphene lattice. One finds that if one calculates hopping parameters between these states, they are close to the orthogonal parameters because the p_z orbitals are dominant in graphene. However, if one would calculate the Löwdin orthogonalized basis state for a GNR, these will no longer be the same for every site because translational symmetry is broken in one direction. Therefore, also the hopping parameters will not be identical throughout the lattice.

In conclusion, for our purposes the non-orthogonal basis states are more convenient, and we will therefore use these hereafter.

Tight-binding model using non-orthogonal basis states

In the first-quantized approach, one starts directly from the lattice Hamiltonian given by

$$\mathcal{H} = -\frac{\hbar^2}{2m}\Delta + \sum_l V^{(A)}(\mathbf{r} - \mathbf{R}_l - \delta_A) + V^{(B)}(\mathbf{r} - \mathbf{R}_l - \delta_B). \quad (2.8)$$

Here, l runs over the Bravais lattice and $V^{(A/B)}$ is a potential that is due to the A/B carbon atom. Because of the symmetry of the honeycomb lattice, $V^{(A)}(\mathbf{r}) = V^{(B)}(\mathcal{R}_\pi^z \mathbf{r})$, where \mathcal{R}_π^z represents a rotation by π around the z -axis. The orbital basis states, $\phi^{(j)}$, are eigenstates of the single-atom Hamiltonian, i.e.

$$\left[-\frac{\hbar^2}{2m}\Delta + V^{(j)}(\mathbf{r}) \right] \phi^{(j)}(\mathbf{r}) = \epsilon^{(j)} \phi^{(j)}(\mathbf{r}),$$

where $j \in \{A, B\}$. The orbital basis states also satisfy $\phi^{(A)}(\mathbf{r}) = \phi^{(B)}(\mathcal{R}_\pi^z \mathbf{r})$. Because of this symmetry, it follows that $\epsilon^{(A)} = \epsilon^{(B)}$, which we denote ϵ_0 from now on. In tight-binding, one assumes that the eigenfunctions are given by a

linear combination of the orbital basis states [15],

$$\psi(\mathbf{r}) = \sum_l [A_{\mathbf{R}_l} \phi^{(A)}(\mathbf{r} - \delta_A - \mathbf{R}_l) + B_{\mathbf{R}_l} \phi^{(B)}(\mathbf{r} - \delta_B - \mathbf{R}_l)], \quad (2.9)$$

where l runs over the triangular Bravais lattice. From Bloch's theorem, it follows that the orbital coefficients should satisfy $A_{\mathbf{R}_l} = A_{\mathbf{k}} e^{i\mathbf{k} \cdot \mathbf{R}_l}$ and $B_{\mathbf{R}_l} = B_{\mathbf{k}} e^{i\mathbf{k} \cdot \mathbf{R}_l}$ and thus,

$$\psi_{\mathbf{k}}(\mathbf{r}) = A_{\mathbf{k}} \psi_{\mathbf{k}}^{(A)}(\mathbf{r}) + B_{\mathbf{k}} \psi_{\mathbf{k}}^{(B)}(\mathbf{r}), \quad (2.10)$$

with

$$\psi_{\mathbf{k}}^{(j)}(\mathbf{r}) = \sum_l e^{i\mathbf{k} \cdot \mathbf{R}_l} \phi^{(j)}(\mathbf{r} - \delta_j - \mathbf{R}_l).$$

To find the energy spectrum, we have to look for eigenstates of the Hamiltonian, i.e. states $\psi_{\mathbf{k}}$ that satisfy the time-independent Schrödinger equation $\mathcal{H}\psi_{\mathbf{k}} = E_{\mathbf{k}}\psi_{\mathbf{k}}$. Here, \mathcal{H} is the first-quantized Hamiltonian (2.8). If we multiply the Schrödinger equation by $\psi_{\mathbf{k}}^*$ on both sides and integrate over space, we obtain

$$(A_{\mathbf{k}}^*, B_{\mathbf{k}}^*) \mathcal{H}_{\mathbf{k}} \begin{pmatrix} A_{\mathbf{k}} \\ B_{\mathbf{k}} \end{pmatrix} = E_{\mathbf{k}} (A_{\mathbf{k}}^*, B_{\mathbf{k}}^*) \mathcal{S}_{\mathbf{k}} \begin{pmatrix} A_{\mathbf{k}} \\ B_{\mathbf{k}} \end{pmatrix}, \quad (2.11)$$

with

$$\mathcal{H}_{\mathbf{k}} = \begin{pmatrix} \int d\mathbf{r} \psi_{\mathbf{k}}^{(A)*} \mathcal{H} \psi_{\mathbf{k}}^{(A)} & \int d\mathbf{r} \psi_{\mathbf{k}}^{(A)*} \mathcal{H} \psi_{\mathbf{k}}^{(B)} \\ \int d\mathbf{r} \psi_{\mathbf{k}}^{(B)*} \mathcal{H} \psi_{\mathbf{k}}^{(A)} & \int d\mathbf{r} \psi_{\mathbf{k}}^{(B)*} \mathcal{H} \psi_{\mathbf{k}}^{(B)} \end{pmatrix}$$

and

$$\mathcal{S}_{\mathbf{k}} = \begin{pmatrix} \int d\mathbf{r} \psi_{\mathbf{k}}^{(A)*} \psi_{\mathbf{k}}^{(A)} & \int d\mathbf{r} \psi_{\mathbf{k}}^{(A)*} \psi_{\mathbf{k}}^{(B)} \\ \int d\mathbf{r} \psi_{\mathbf{k}}^{(B)*} \psi_{\mathbf{k}}^{(A)} & \int d\mathbf{r} \psi_{\mathbf{k}}^{(B)*} \psi_{\mathbf{k}}^{(B)} \end{pmatrix}.$$

The energy dispersion is determined by solving the secular equation

$$\det[\mathcal{H}_{\mathbf{k}} - E_{\mathbf{k}}^{\lambda} \mathcal{S}_{\mathbf{k}}] = 0, \quad (2.12)$$

with λ determining the energy band.

In order to solve Eq. (2.12), we can rewrite the first-quantized Hamiltonian matrix as

$$\mathcal{H}_{\mathbf{k}}^{ij} = \bar{N} (\epsilon_0 s_{\mathbf{k}}^{ij} + t_{\mathbf{k}}^{ij}), \quad (2.13)$$

where we have defined the overlap and hopping matrix parameters as

$$s_{\mathbf{k}}^{ij} = \sum_{\mathbf{R}_l} e^{i\mathbf{k} \cdot \mathbf{R}_l} s^{(ij)}(\mathbf{R}_l + \delta_i - \delta_j) = \frac{\mathcal{S}_{\mathbf{k}}^{ij}}{\bar{N}}, \quad \text{with} \quad s^{(ij)}(\mathbf{r}) = \int d\mathbf{r}' \phi^{(i)*}(\mathbf{r}' - \mathbf{r}) \phi^{(j)}(\mathbf{r}'),$$

$$t_{\mathbf{k}}^{ij} = \sum_{\mathbf{R}_l} e^{i\mathbf{k} \cdot \mathbf{R}_l} t^{(ij)}(\mathbf{R}_l + \delta_i - \delta_j), \quad \text{with} \quad t^{(ij)}(\mathbf{r}) = \int d\mathbf{r}' \phi^{(i)*}(\mathbf{r}' - \mathbf{r}) \Delta V^{(j)}(\mathbf{r}') \phi^{(j)}(\mathbf{r}').$$

(2.14)

Here, we have defined the perturbative part of the Hamiltonian corresponding to sublattice A as

$$\Delta V^{(A)}(\mathbf{r}) = \sum_l [V^{(A)}(\mathbf{r} - \mathbf{R}_l) + \sum_l V^{(B)}(\mathbf{r} - \mathbf{R}_l - \delta_B)] - V^{(A)}(\mathbf{r}), \quad (2.15)$$

and $\Delta V^{(B)}(\mathbf{r}) = \Delta V^{(A)}(\mathcal{R}_\pi^z \mathbf{r})$. Sublattice symmetry implies that $t^{(AB)}(\mathbf{r}) = t^{(BA)}(\mathcal{R}_\pi^z \mathbf{r})$ and $t^{(AA)}(\mathbf{r}) = t^{(BB)}(\mathbf{r})$, and the same for the overlaps. From this we can derive that $t_{\mathbf{k}}^{AA} = t_{\mathbf{k}}^{BB}$, $t_{\mathbf{k}}^{AB*} = t_{\mathbf{k}}^{BA}$, $s_{\mathbf{k}}^{AA} = s_{\mathbf{k}}^{BB}$, $s_{\mathbf{k}}^{AB*} = s_{\mathbf{k}}^{BA}$, and $s_{\mathbf{k}}^{AB} t_{\mathbf{k}}^{AB*} = t_{\mathbf{k}}^{AB} s_{\mathbf{k}}^{AB*}$. In order to simplify notation, we will define $t'_{\mathbf{k}} \equiv t_{\mathbf{k}}^{AA}$ and $s'_{\mathbf{k}} \equiv s_{\mathbf{k}}^{AA}$, which correspond to intra-sublattice orbital hopping and overlap respectively, and $t_{\mathbf{k}} \equiv t_{\mathbf{k}}^{AB}$ and $s_{\mathbf{k}} \equiv s_{\mathbf{k}}^{AB}$, which correspond now to inter-sublattice. We can rewrite these expressions in a similar form as Eq. (2.5),

$$\begin{aligned} t_{\mathbf{k}} &= \sum_n t_n f_n(\mathbf{k}), & s_{\mathbf{k}} &= \sum_n s_n f_n(\mathbf{k}), \\ t'_{\mathbf{k}} &= \sum_n t'_n g_n(\mathbf{k}), & s'_{\mathbf{k}} &= \sum_n s'_n g_n(\mathbf{k}). \end{aligned} \quad (2.16)$$

Here, f_n and g_n are defined as in Eq. (2.5) and $t_n = t^{AB}(\mathbf{R}_l + \delta_B - \delta_A)$, $s_n = s^{AB}(\mathbf{R}_l + \delta_B - \delta_A)$, where l is such that $|\mathbf{R}_l + \delta_B - \delta_A| = d_n$, and $t'_n = t^{AA}(\mathbf{R}_l)$, $s'_n = s^{AA}(\mathbf{R}_l)$, where l is such that $|\mathbf{R}_l| = d'_n$. These parameters are the n -th intra- and inter-orbital hopping and overlap parameters respectively. Using these definitions, the problem is reduced to finding the spectrum of the matrix equation

$$\begin{pmatrix} s'_{\mathbf{k}} & s_{\mathbf{k}} \\ s_{\mathbf{k}}^* & s'_{\mathbf{k}} \end{pmatrix}^{-1} \begin{pmatrix} t'_{\mathbf{k}} & t_{\mathbf{k}} \\ t_{\mathbf{k}}^* & t'_{\mathbf{k}} \end{pmatrix} \begin{pmatrix} A_{\mathbf{k}} \\ B_{\mathbf{k}} \end{pmatrix} = (E_{\mathbf{k}}^\lambda - \epsilon_0) \begin{pmatrix} A_{\mathbf{k}} \\ B_{\mathbf{k}} \end{pmatrix}. \quad (2.17)$$

Solving for $E_{\mathbf{k}}^\lambda$ yields the orbital dispersion

$$E_{\mathbf{k}}^\lambda = \frac{H'_{\mathbf{k}} + \lambda |H_{\mathbf{k}}|}{S_{\mathbf{k}}} + \epsilon_0, \quad (2.18)$$

with $\lambda = \pm$. Here, we have introduced

$$H'_{\mathbf{k}} = s'_{\mathbf{k}} t'_{\mathbf{k}} - s_{\mathbf{k}}^* t_{\mathbf{k}}, \quad H_{\mathbf{k}} = s'_{\mathbf{k}} t_{\mathbf{k}} - t'_{\mathbf{k}} s_{\mathbf{k}}, \quad S_{\mathbf{k}} = (s'_{\mathbf{k}})^2 - s_{\mathbf{k}} s_{\mathbf{k}}^*. \quad (2.19)$$

Note the similarity between the dispersion obtained from the orthogonal basis states of Eq. (2.6) and the dispersion given by Eq. (2.18). If the orbital basis states would turn out to be orthogonal the orbital dispersion would be identical to the orthogonal dispersion because $S_{\mathbf{k}}$ would be the identity matrix. In fact, we can show in general that for graphene we can make a mapping from the orbital parameters to the orthogonal parameters that reproduce the same dispersion. This relation is further discussed in Appendix A.

We can illustrate this correspondence by taking only NN and NNN orbital hopping and NN orbital overlap into account and comparing that to Eq. (2.7). We find, after some algebra, that with this assumption Eq. (2.18) reduces to

$$E_{\mathbf{k}}^{\lambda} = \frac{t'(|\gamma_{\mathbf{k}}|^2 - 3) + \lambda|t\gamma_{\mathbf{k}}|}{1 + \lambda|s\gamma_{\mathbf{k}}|} + \epsilon_0. \quad (2.20)$$

For $s \ll 1$ and $t' \ll t$, this relation can be approximated by $E_{\mathbf{k}}^{\lambda} = (t' - st)|\gamma_{\mathbf{k}}|^2 + \lambda t|\gamma_{\mathbf{k}}| + \epsilon_0 - 3t'$. This result is also equivalent to the two-parameter orthogonal dispersion of Eq. (2.7) if we choose our parameters such that $\bar{t}' = t' - st$ and $\bar{t} = t$. If we assume that in the first-quantized formalism the hoppings are negative and the overlaps positive, and that $|st| > |t'|$, \bar{t}' has to be positive. This approximate relation already explains that it was indeed not unreasonable to take a positive \bar{t}' hopping but a negative \bar{t} .

We are looking for a minimal model that satisfies the two criteria that were stated in the previous section: the parameters have to be valid also after confinement and their dependence on the distance should be known. To achieve this aim, we assume that the orbital hopping and overlap parameters satisfy an exponential decay given by

$$t(\mathbf{r}) = \begin{cases} t_0 e^{\kappa(1-|r|/a)} & |r| > 0 \\ 0 & |r| = 0 \end{cases}, \quad s(\mathbf{r}) = \begin{cases} s_0 e^{\kappa(1-|r|/a)} & |r| > 0 \\ 1 & |r| = 0 \end{cases}, \quad (2.21)$$

where a is the NN distance and t_0 and s_0 are the values of the NN hopping and the overlap parameter, respectively. Note that hopping to the same site is zero, and that the overlap of an orbital with itself is one, which means that the orbitals are normalized. The dimensionless constant κ determines the fall-off rate of the hopping. We further assume that the hopping and overlap parameters are proportional to each other, which implies that κ is the same for both.

This model satisfies the two criteria to potentially describe a bent GNR. The first criterion, which demands that the model is still valid in a confined geometry, is satisfied because we here explicitly include the overlap. Therefore, the basis states are not orthogonal and a Löwdin orthogonalization scheme is not necessary. Thus, the basis state will not become site dependent after geometric confinement. The second criterion is satisfied because we assumed an exponential decay.

One could argue that we can also assume $s_0 = 0$. This is basically used in Ref. [18]. However, this model would miss essential features. For instance such a model does not reproduce the correct particle-hole asymmetry. For low energies, however, the overlap becomes unimportant and this model would yield a good estimate.

By fitting the dispersion of Eq. (2.18) to the reference first-principle spectrum, we find that $t_0 = -2.8$ eV, $s_0 = 0.2$, and $\kappa = 2.6$ is a reasonable match, which is also not very far away from the parameters used in [20]. Though

with a more elaborate fitting method, parameters that reproduce the reference spectrum more closely could be found, we settle with these as we are mostly interested in global trends and not in the minute exactness of the spectra.

The dispersion relation, given by Eq. (2.18), along the line connecting high-symmetry points is shown in Fig. 2.2. Here, exponentially decaying hopping and overlap parameters were used and ϵ_0 was chosen such that zero energy lies at the K point. The dispersion displays a linear behavior around the K point and the same asymmetry between the π and π^* band as before. In general, the two-parameter orthogonal dispersion appears to be similar to the exponential non-orthogonal dispersion. At the M point, the different dispersions seem to differ the most. This is not surprising, as it has been shown that the behaviour around the M point is strongly influenced by higher-order hoppings [21].

In conclusion, we can state that a tight-binding model using exponentially decaying hopping and overlap parameters represents a minimal model that still reproduces the spectrum of graphene reasonably well. Therefore we will use this model for the calculations of the electronic structure of bent GNRs considered in this thesis.

Chapter 3

Electronic structure of graphene nanoribbons

This chapter first reviews the geometry of GNRs. Then, we calculate the electronic spectrum of ribbons assuming a periodic boundary condition and using tight-binding theory. Specifically, the bandgap structure of armchair GNRs (AGNRs) and the edge states in zigzag GNRs (ZGNRs) are studied. The assumption of periodic boundary conditions significantly reduces the size of the matrices involved in the calculations. In the appendix B, we argue that long finite ribbons approach the periodic case by comparing their density of states.

3.1 Geometry of graphene nanoribbons

GNRs are pieces of graphene with a rectangular shape. In Figs. 3.1a and 3.1b the lattice points of an AGNR and a ZGNR are depicted, respectively. A GNR is determined by its length, width and the type of terminations on its sides. We can precisely characterize a GNR by defining its 1D lattice vector, \mathbf{a} , and its 1D unit cell, see Fig. 3.1. The vector \mathbf{a} lies parallel to the long side of the ribbon, in such a way that it would be the smallest translational symmetry vector if the length would be infinite. The 1D unit cell is the set of lattice points such that by adding multiples of \mathbf{a} to the 1D unit cell, we can construct the complete ribbon. Two important GNRs are armchair (AGNRs) and zigzag ribbons (ZGNRs). If we assume that the carbon atoms in the GNR are oriented in the same way as for graphene in Section 2.1, then for AGNRs $\mathbf{a} = \mathbf{a}_1 + \mathbf{a}_2 = (3a, 0)$, with \mathbf{a}_1 , \mathbf{a}_2 , and a as defined in that section. ZGNRs satisfy $\mathbf{a} = \mathbf{a}_1 = \frac{a}{2}(3, \sqrt{3})$ in that orientation.

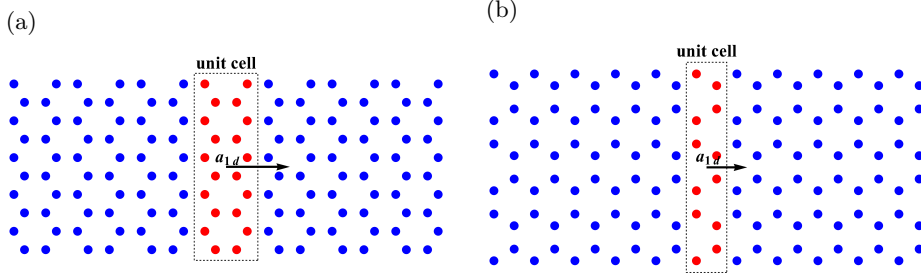


Figure 3.1: (a) Armchair ribbon; the red dots in the dotted box are the points $\mathbf{R}_n + \delta_B$ and $\mathbf{R}_n + \delta_A$ of the 1D unit cell and the vector \mathbf{a} is the 1D lattice vector. The orientation is the same as we took for the description of graphene. (b) Zigzag ribbon, the orientation is now rotated by $\pi/3$ radians.

3.2 Tight-binding model of graphene nanoribbons

As motivated in Chapter 2, we will treat GNRs using a non-orthogonal tight-binding model. We assume here that all dangling bonds at the GNR edges are terminated by hydrogen atoms. This allows us to approximate the GNR also as a system with purely p_z electrons, at least around the Fermi level. If we assume a periodic boundary condition along the ribbon, a GNR can be treated as a 1D crystal. We start with the general tight-binding form of the wavefunction given by Eq. (2.9). In that equation, \mathbf{R}_l now runs over those graphene Bravais lattice points that are inside the ribbon. Note that Eq. (2.9) assumes that for every \mathbf{R}_l both, the associated A and B atom are in the GNR, but this is not necessarily true for every GNR geometry. For AGNR and ZGNR, which we consider here, this is however the case. We could also start without this restriction, but it would make it less obvious to recognize effects that are specifically due to the structure of the honeycomb lattice.

Because of the periodic boundary condition, translation by the lattice vector \mathbf{a} leaves the lattice invariant. We can then use the 1D Bloch's theorem, which states that the components $A_{\mathbf{R}_l}$ and $B_{\mathbf{R}_l}$ in Eq. (2.9) transform as

$$\begin{aligned} A_{\mathbf{R}_l+\mathbf{a}} &= e^{i\mathbf{k}^{1d}\cdot\mathbf{a}} A_{\mathbf{R}_l}, \\ B_{\mathbf{R}_l+\mathbf{a}} &= e^{i\mathbf{k}^{1d}\cdot\mathbf{a}} B_{\mathbf{R}_l}. \end{aligned}$$

Here, \mathbf{k}^{1d} is some vector in the 1D BZ of the 1D lattice spanned by the lattice vector \mathbf{a} . We can write \mathbf{k}^{1d} as $\mathbf{k}^{1d} = k\mathbf{a}/|\mathbf{a}|^2$ with $k \in [0, 2\pi]$, then $\mathbf{k}^{1d} \cdot \mathbf{a} = k$. We now split the sum over \mathbf{R}_l in Eq. (2.9) into a part that is proportional to the lattice vector \mathbf{a} and a part that contains the positions \mathbf{R}_l of the 1D unit cell of this ribbon, see Fig. 3.1. We thus write for $\mathbf{R}_l = t\mathbf{a} + \mathbf{R}_n^{1d}$, where $n \in \{1, \dots, N\}$ and $t \in \{1, \dots, N^u\}$. N is the number of \mathbf{R}_l coordinates and N^u is the number of 1D unit cells that there are in the complete ribbon. With

these definitions, Bloch's theorem states that the eigenstates are of the form

$$\psi_k(\mathbf{r}) = \sum_{n,t} e^{ik \cdot t} A_{k,n} \phi^{(A)}(\mathbf{r} - \delta_A - \mathbf{R}_n^{1d} - t\mathbf{a}) + e^{ik \cdot t} B_{k,n} \phi^{(B)}(\mathbf{r} - \delta_B - \mathbf{R}_n^{1d} - t\mathbf{a}). \quad (3.1)$$

As for the graphene case, we now solve the time-independent Schrödinger equation. We multiply the Schrödinger equation by $\psi_k^*(\mathbf{r})$, and integrate over space to get $\int d\mathbf{r} \psi_k^*(\mathbf{r}) \mathcal{H} \psi_k(\mathbf{r}) = E_k \int d\mathbf{r} \psi_k^*(\mathbf{r}) \psi_k(\mathbf{r})$, where \mathcal{H} is the Hamiltonian given by Eq. (2.8). Using the 1D Bloch form of the eigenstates, we can rewrite this integral equation as

$$u_k^\dagger \mathcal{H}_k u_k = E_k u_k^\dagger \mathcal{S}_k u_k, \quad (3.2)$$

where

$$u_k = \begin{pmatrix} A_{k,1} \\ \vdots \\ A_{k,N} \\ B_{k,1} \\ \vdots \\ B_{k,N} \end{pmatrix}, \quad (3.3)$$

and

$$\mathcal{H}_k = \begin{pmatrix} H_k^{(AA)} & H_k^{(AB)} \\ H_k^{(BA)} & H_k^{(BB)} \end{pmatrix}, \quad (3.4)$$

$$\mathcal{S}_k = \begin{pmatrix} S_k^{(AA)} & S_k^{(AB)} \\ S_k^{(BA)} & S_k^{(BB)} \end{pmatrix}.$$

Here, each $H_k^{(ij)}$ and $S_k^{(ij)}$ is a $N \times N$ matrix. Its components are given by

$$H_{k,mn}^{(ij)} = N^u \left(\epsilon_0 s_{k,mn}^{ij} + t_{k,mn}^{ij} \right), \quad (3.5)$$

where N^u is the number of 1D ribbon unit cells in the \mathbf{a} direction, $m, n \in \{1, \dots, N\}$, and

$$s_{k,mn}^{ij} = \sum_t e^{ik \cdot t} s(\delta_j + t\mathbf{a} + \mathbf{R}_n^{1d} - \delta_i - \mathbf{R}_m^{1d}) = \frac{\mathcal{S}_{k,mn}^{ij}}{N^u}, \quad (3.6)$$

$$t_{k,mn}^{ij} = \sum_t e^{ik \cdot t} t(\delta_j + t\mathbf{a} + \mathbf{R}_n^{1d} - \delta_i - \mathbf{R}_m^{1d}). \quad (3.7)$$

The parameters $t(\mathbf{R})$ and $s(\mathbf{R})$ are defined as in Eq. (2.14). Using this notation, the derivation of the tight-binding model is reduced to solving the matrix equation,

$$s_k^{-1} t_k u_k = (E_k^\lambda - \epsilon_0) u_k. \quad (3.8)$$

where the matrices are of $2N \times 2N$ form. To find the dispersion, we solve the secular equation,

$$\det[t_k - (E_k^\lambda - \epsilon_0)s_k] = 0. \quad (3.9)$$

We can then use the different conventions for t and s to obtain the dispersion relation for ribbons. One aspect that is not considered here, but could be worth investigating, is the possibility to include different hopping values for lattice points on the boundary of the ribbon. This can be argued to be the case, as the p_z -orbitals on the boundary are different due to the chemical termination and the edge atoms can be closer or further apart than the bulk atoms. Note that this is a different argument than the one used to discard orthogonal tight-binding theory for GNRs in Chapter 2. Because the matrices in Eq. (3.9) become large very fast, it is not obvious how to solve Eq. (3.9) analytically and it is more straightforward to rely on numerics. As numeric methods for solving polynomials are not efficient, it turns out to be more convenient to directly solve the matrix equation, Eq. (3.8). In practice, this is done by sampling different k values, then calculating the matrices, and finally solving for the spectrum numerically.

In Ref. [22], however, analytical solutions are presented for the orthogonal NN hopping case. There, it is shown that the spectrum and eigenstates of AGNRs can be expressed in simple closed formulas, reminiscent of the solution for zigzag carbon nanotubes. For ZGNRs, the spectrum and eigenstates can also be expressed as closed functions, but they are more complicated than for AGNRs because they depend on the roots of a non-trivial transcendental equation. We will not reproduce these expressions here. We will however refer to the analytical solution later on to study some specific aspects of the zigzag ribbon.

We will now discuss the spectra of AGNRs and ZGNRs and their characteristic features.

Armchair graphene nanoribbon spectrum

Fig. 3.2 shows the 1D dispersion relation for exponentially decaying hopping and overlap parameters, as defined in Eq. (2.21). Here, we choose the same overlap parameter as for the graphene calculation, $s_0 = 0.2$, and also the same decaying factor $\kappa = 2.6$; ϵ_0 is chosen such that the Fermi energy is at zero. Because we here do not compare to a reference spectra, we have left t_0 unspecified. This procedure is allowed because it can be seen from Eq. (3.9) that the dispersion scales linearly with t_0 when the scale is normalized around the Fermi level. We will adopt this procedure in all future calculations.

The most striking thing of AGNRs is that their band structure is gapped, and the size of the gap depends on the width and type. One can distinguish three types of armchair GNRs:

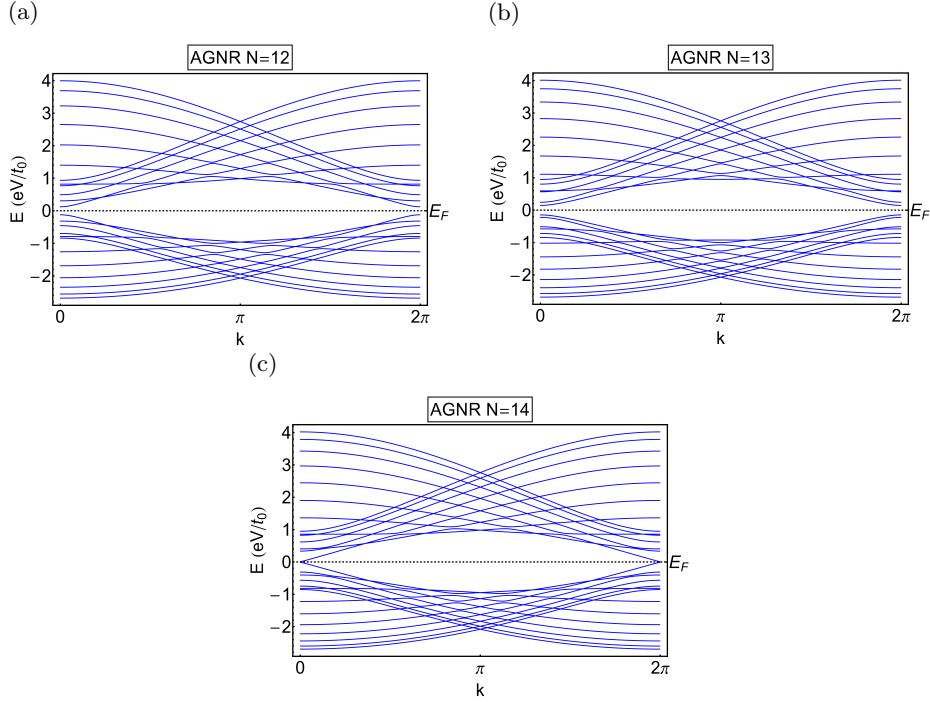


Figure 3.2: Spectra of three different sized AGNRs representing type I ($N = 12$), type II ($N = 13$) and type III ($N = 14$). All spectra were calculated using exponentially decaying hopping and overlap with $t_0 = -1$ eV, $s_0 = 0.2$, $\kappa = 2.6$, and ϵ_0 such that the Fermi energy is at zero.

- Type I has a number N of A, B pairs such that $N = 3p$ for a certain p . In a NN tight-binding description, this type has a bandgap Δ_{3p} .
- Type II has $N = 3p + 1$ and also has a bandgap in NN tight-binding Δ_{3p+1} .
- Type III has $N = 3p + 2$ and is metallic in NN tight-binding $\Delta_{3p+2} = 0$.

The order of sizes of bandgaps within a NN tight-binding description is $\Delta_{3p} \gtrsim \Delta_{3p+1} > \Delta_{3p+2}$. However, if higher order hoppings are introduced, also type III develops a small bandgap. These observations require adjustments in a first-principle treatment, in which case type III develops quite a significant bandgap and the order of the bandgaps is changed to $\Delta_{3p} > \Delta_{3p+1} > \Delta_{3p+2}$ [4].

In Fig. 3.2, spectra of type I,II, and III AGNRs are depicted using the exponentially decaying non-orthogonal parameters.

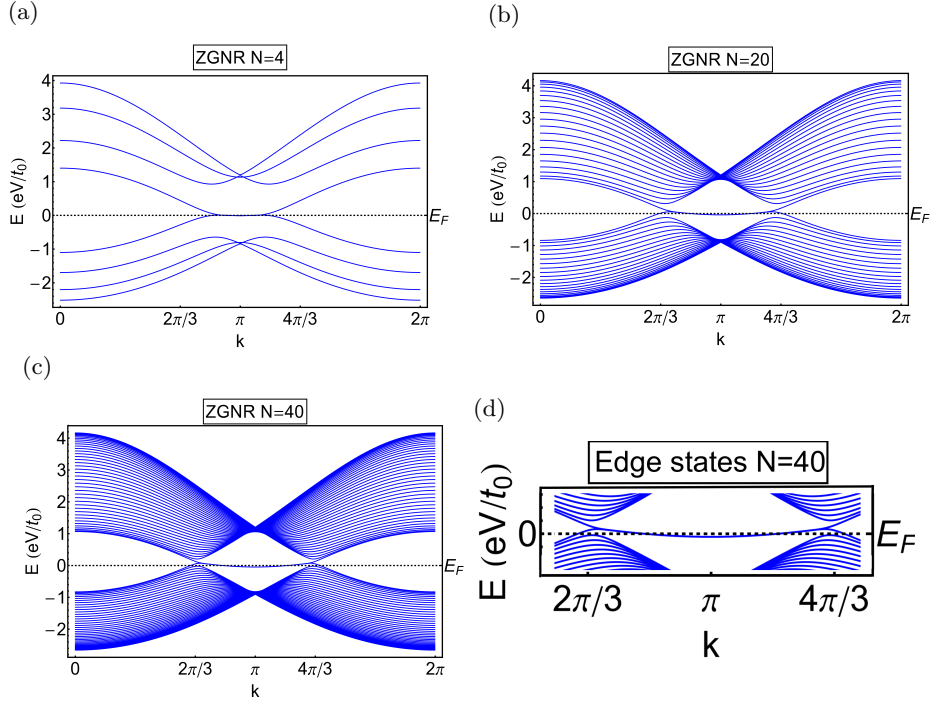


Figure 3.3: (a,b,c) Spectra of different sized ZGNRs with periodic boundary conditions. All spectra are calculated using exponentially decaying hopping and overlap with $t_0 = -1$ eV, $s_0 = 0.2$, $\kappa = 2.6$, and ϵ_0 such that the Fermi energy is at zero. (d) detail of (c) showing the slight dispersion of the edge states.

Zigzag graphene nanoribbon spectrum

In Fig. 3.3, the results of spectra calculations for different sized ZGNRs are shown. We reproduce the most striking feature is the emergence of two almost degenerate bands around the Fermi level [3]. These states are localized on the edge of the GNR. At $k = \pi$, these states are maximally localised on the edge. Toward the $k = 2\pi/3$ and $k = 4\pi/3$ points, the edge states acquire a larger decay length. If one only considers NN hopping, the edge states are degenerate at $k = \pi$. They split between a bonding and antibonding pair of two states localised on either edge if k moves further away from π .

What is remarkable about the results obtained from our tight-binding calculation using exponentially decaying non-orthogonal parameters is that the edge states are dispersive. We can see in Fig. 3.3 that the dispersion is slightly upwardly curved around the $k = \pi$ point. This can be most easily explained from a perturbation theory on the edge state of a semi-infinite graphene sheet with a zigzag edge within a model including only NN hopping. In that case the exact solution is particularly simple [22]. We will not reproduce this here,

but only recall that because the states which are being perturbed are at zero energy, a perturbation by the overlaps is not of first order. However, the NNN neighbor hopping is. Because of the increasing decay length of the state as k deviates from π , it turns out that a negative NNN hopping results in an effective 1D band structure with a positive hopping. This is indeed what is observed in Fig. 3.3. We explained this in detail because this emergence of a 1D band structure is similar to what will be observed later in the bending of a ZGNR. Note also that the orthogonal parameters typically used for graphene assume a positive NNN hopping, which would result in a negative hopping for the effective 1D band structure. If we compare to first-principle studies, which is not depicted here, we however observe that the effective 1D band structure has a positive hopping. This reinforces our claim that non-orthogonal hopping parameters are better suited than orthogonal parameters to study confined geometries.

Another interesting result for the edge states of ZGNRs is obtained when one takes interaction into account. Already in the initial prediction of the zigzag edge states in Ref. [3], it was anticipated from a Hubbard interaction that the edge states will become magnetically polarized. This leads ZGNRs to also develop a bandgap, with the lower state consisting of an edge state in which has spin up on one edge and the opposite spin on the other [4]. This effect was recently experimentally measured [23].

Chapter 4

Electronic structure of bent graphene nanoribbons

This chapter contains the main results concerning the electron properties of bent GNRs from tight-binding theory. First, we introduce the necessary geometrical notions of a bent GNR and define a specific type of bending deformation called a lattice-preserving bending. Then, we describe the two particular lattice-preserving bending deformations that we use. We prove that for lattice-preserving deformations, a tight-binding theory almost identical to the one for straight GNRs can be applied. After introducing these conventions and methods, we present the results of the spectrum calculations for AGNRs and ZGNRs. We also calculate the effect of uniform strain on the spectrum of GNRs and use this result as a reference to analyse in depth the deformations of the spectra of AGNRs and ZGNRs. In particular, we show that the bandgap of AGNR with respect to bending behaves similarly to a compressive uniform strain along the ribbon. Lastly, we discuss an interesting emergent 1D band structure for the edge states of ZGNRs that is tunable by bending.

4.1 Geometry of bent graphene nanoribbons

We can describe a bending, or in fact any type of deformation, by a deformation function $\mathbf{F}(\mathbf{r})$, or equivalently by a displacement function $\mathbf{u}(\mathbf{r})$. These are defined such that the coordinates after bending, \mathbf{R}'_i , of a lattice site i are given by $\mathbf{R}'_i = \mathbf{F}(\mathbf{R}_i) = \mathbf{R}_i + \mathbf{u}(\mathbf{R}_i)$.

We will define a type of bending deformation that we call a lattice-preserving bending. This type of bending deformation allows us to calculate the electronic spectrum of the ribbon using similar tight-binding techniques as we used for the straight GNR. However, this type of bending deformation is still general enough to entail various types of bending. We consider two types of lattice-preserving bending deformations in this thesis: width-preserving bending and bondlength-preserving bending.

To describe a bent ribbon, we introduce some geometrical parameters. First of all, we assume a bending such that the ribbon can be imagined to live inside an annulus segment, see Fig. (4.1). We define: R_{in} (R_{out}), the distance from the center of the annulus to the inner (outer) edge, $W' = R_{out} - R_{in}$, the width of the ribbon after bending and $R = (R_{out} + R_{in})/2$, the mean bending radius. We also define the full bending angle θ_{full} , which describes the curvature of the left side with respect to right side of the ribbon. Then $L' = \theta_{full}R$ is the length of the ribbon and $A' = W'L'$ is the area of the ribbon after bending.

However, R is not a convenient parameter to use for bending because it is not dimensionless. One dimensionless parameter is $\Theta' = W'/2R$, as proposed in Ref. [13]. $\Theta' = 0$ corresponds to a straight ribbon. $\Theta' = 1$ corresponds to a completely bent ribbon with no hole in the middle, i.e. all the lattice sites at the inner edge are on top of each other. For convenience, however, we use a slightly different bending parameter, namely $\Theta = W/2R$. Θ together with W' and L' completely describes the annulus in which the bent ribbon is situated.

We are now ready to define a lattice preserving bending. The points $\mathbf{R}_n^{1d} = \mathbf{F}(\mathbf{R}_n^{1d})$, where $n \in \{1, \dots, N\}$ and \mathbf{R}_n^{1d} are the sites of the undeformed ribbon unit cell. In Fig. (4.1), these are the sites in the dotted region. The definition of a lattice-preserving bending is that each lattice site \mathbf{R}'_i after bending is related to a lattice site in the deformed 1D unit cell rotated by a multiple t of a certain angle. Here, t is such that $\mathbf{R}_i = t\mathbf{a} + \mathbf{R}_n^{1d}$ for some n . The angle with which the unit cell is rotated is the same along the whole ribbon, denoted by θ_{1d} . It satisfies $\theta_{1d} = \theta_{full}/N^u$, where N^u is the number of unit cells in the ribbon. We also define $|\mathbf{a}'| = \theta_{1d}R = L'/N^u$ which is the arc length of the center of the bent unit cell. Choosing the center of the annulus to be in the origin, we can define a lattice-preserving bending in a more compact way. A lattice-preserving bending is a deformation that satisfies the discrete rotational symmetry

$$\mathbf{F}(\mathbf{R}_i + \mathbf{a}) = \mathcal{R}_{-\theta_{1d}}\mathbf{F}(\mathbf{R}_i), \quad (4.1)$$

where $\mathcal{R}_{-\theta_{1d}}$ is the rotation matrix that rotates by θ_{1d} clockwise.

From the previous definitions, we can see that $\theta_{1d} = \Theta|\mathbf{a}'|/(W/2)$. Note that Θ , W' and $|\mathbf{a}'|$ (or L') were also the three parameters that determine the annulus and vice versa. So, if we know the shape of the annulus segment, we only have to know how the bent unit cell looks like to construct the complete ribbon.

The bending parameter Θ has an intuitive interpretation for small values, if the length and width of the ribbon stay approximately the same. In that case, it is equal to the absolute value of the strain at the outer and inner edge of the ribbon in the direction along the ribbon. We can understand this statement by considering two points on the edge of a bent ribbon separated by an angle θ_{1d} . If θ_{1d} is small, their distance apart is $(R \pm W'/2)\theta_{1d} = |\mathbf{a}'|(1 \pm \Theta W'/W)$, where $+$ ($-$) corresponds to the outer (inner) edge. Originally, these points

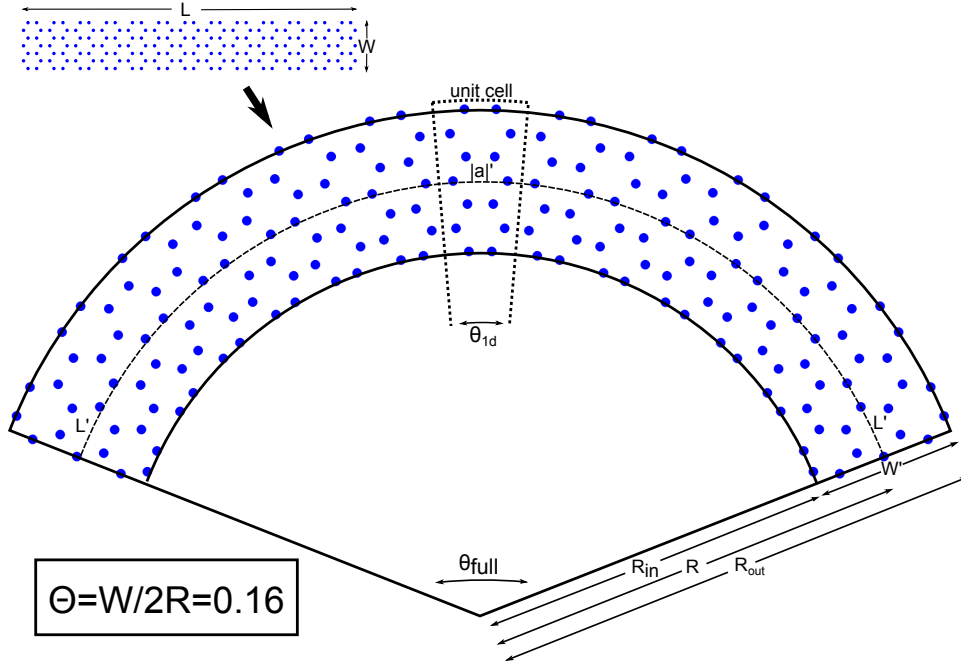


Figure 4.1: Depiction of the parameters R_{in} , R_{out} , R , W , W' , L , L' , $|\mathbf{a}'|$, θ_{1d} , θ_{full} and Θ used to define a lattice preserving bending.

were $|\mathbf{a}|$ apart. Therefore the strain, for small Θ , in the inner edge and outer edge is

$$\epsilon_{in/out} = \frac{|\mathbf{a}'| - |\mathbf{a}|}{|\mathbf{a}|} \pm \Theta \frac{W'|\mathbf{a}'|}{W|\mathbf{a}|}.$$

If $L' \approx L$ and $W' \approx W$, this implies $\epsilon_{in} \approx -\Theta$ and $\epsilon_{out} \approx \Theta$.

One important point is that a lattice-preserving bending still allows for quite a lot of freedom in the type of bending deformations possible. For a certain bending parameter Θ , for instance, bends with a very large θ_{1d} could be created by making L' really long, stretching the ribbon, or W' really small. In order to further restrict the types of bends, we can set extra requirements that should be preserved after bending. One possibility, which we will not use, is to require that the area remains unchanged after bending. In that case $|\mathbf{a}|W = |\mathbf{a}'|W'$ and $\theta_{1d} = \Theta|\mathbf{a}|/(W'/2)$. We, however, require that the distances along the middle of the GNR remain unchanged after bending. In that case $|\mathbf{a}| = |\mathbf{a}'|$. This results in the relation $\theta_{1d} = \Theta|\mathbf{a}|/(W/2)$, which is more convenient for later calculations.

After this general definition of lattice-preserving bending deformations, we will present two specific examples that we will use in our calculations.

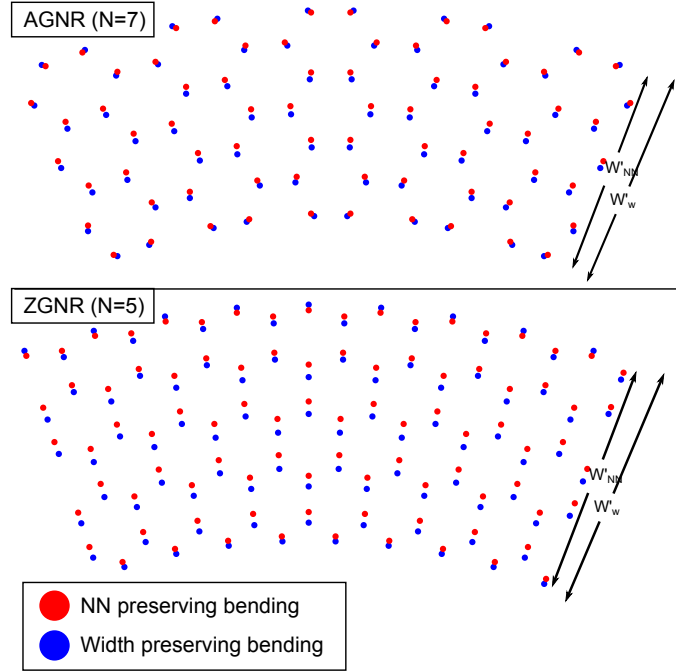


Figure 4.2: (Top panel) A bent AGNR with $N = 7$ and $\Theta = 0.15$ for bondlength-preserving (red dots) and width preserving (blue dots). (Bottom panel) Similar for a ZGNR with $N = 5$ and $\Theta = 0.15$.

Width-preserving bending

We first consider width-preserving bending, shown in Fig. 4.2. We can explicitly describe the deformation function by

$$\mathbf{F}^w(\mathbf{r}, \Theta) = \mathcal{R}_{-r_x 2\Theta/W} \begin{pmatrix} 0 \\ r_y + W/2\Theta \end{pmatrix} = (r_y + R) \begin{pmatrix} \sin(r_x/R) \\ \cos(r_x/R) \end{pmatrix}. \quad (4.2)$$

Here, $\mathbf{r} = (r_x, r_y)$, Θ is the bending parameter, W is the width of the ribbon before bending, $\mathcal{R}_{-r_x 2\Theta/W}$ is the rotation matrix that rotates by $r_x 2\Theta/W$ clockwise, and $R = W/2\Theta$. This deformation assumes that the ribbon has been positioned such that the 1D lattice vector points along the x -direction and the ribbon is balanced in the y -direction such that the middle of the GNR is on the x -axis. Therefore the y coordinate of the undeformed site runs inside $[-W/2, W/2]$. One can easily confirm that this bending satisfies the definition of a lattice preserving bending $\mathbf{F}^w(\mathbf{r} + \mathbf{a}_{1d}, \theta_b) = \mathcal{R}_{-\theta_{1d}} \mathbf{F}^w(\mathbf{r}, \theta_b)$. Note that for $\Theta = 0$, the corresponding displacement function sends the ribbon to a straight ribbon, but positioned at infinity.

We call this type of bending width preserving bending, because the distance between sites in the direction along the width of the GNR is unchanged. Namely, for any r_x and Θ , $W' = \mathbf{F}^w(r_x, W/2, \Theta) \hat{r} - \mathbf{F}^w(r_x, -W/2, \Theta) \hat{r} = W$.

Another feature of this bending is that the strain in the direction along the ribbon increases linearly from the inner to the outer edge. Because of this reason and because we consider a bending equally compressed on the inside as stretched on the outside, this bending has the property that exactly at the middle of the ribbon the strain is zero. One can visualize this bending by imagining horizontally spaced stiff vertical rods of a uniform length connected by a horizontal rod placed in the middle. If one then bends this horizontal rod exactly along a circle, the points on the vertical rods will be described by $\mathbf{F}^w(\mathbf{r}, \Theta)$.

Bondlength-preserving bending

The width-preserving deformation may not be energetically favorable because bond-length deformations require more energy than deformations in the angles between bonds. However, we can construct a lattice-preserving bending that is completely bond-length preserving. We will call this bending the bondlength-preserving bending, $\mathbf{F}^{NN}(\mathbf{r}, \Theta)$.

We construct its operations $\mathbf{F}^{NN}(\mathbf{R}_i, \Theta)$ on specific ribbon sites \mathbf{R}_i recursively, and then show that it indeed satisfies the discrete rotational symmetry condition given by Eq. (4.1), and that it preserves the length of the bonds. We also have to treat the zigzag and the armchair case separately, as for these \mathbf{F}^{NN} is not identical. Here, we consider only these two cases.

Before we explain the construction, we observe some features of \mathbf{F}^{NN} (see Fig. 4.2). The bondlength-preserving bending is similar to the width preserving but has a non-linear strain profile from the bottom to the top of the ribbon. At the inner edge, the ribbon experiences not only longitudinal compressive strain, but also transverse tensile strain. At the outer edge, on the other hand, a compressive transverse strain is present. It is also important to note that the total width becomes reduced. This reduction of width needs to be taken into account when comparing effects of the bondlength-preserving with the width-preserving bending. As a consequence of the reduction of width, the longitudinal strains at the inner (ϵ_{in}) and outer edge (ϵ_{out}) are not identical for the two methods.

Let us now construct \mathbf{F}^{NN} for a ZGNR. We start by constructing the bent 1D unit cell. If we choose our orientation in the right way, we can say that the first site in the bent unit cell is positioned at $\mathbf{R}_1^{1d} = (0, R - W'/2)$. Note that we do not know W' and R yet, but they will be obtained using a recursive procedure outlined below. We can now recursively generate the next atoms in the deformed 1D unit cell using the following rule:

$$\mathbf{R}_i^{1d} = \begin{cases} f(\mathbf{R}_{i-1}^{1d}, \theta_{1d}) \mathcal{R}_{-\theta_{1d}/2} \widehat{\mathbf{R}_{i-1}^{1d}} & \text{if } i \text{ is even} \\ (|\mathbf{R}_{i-1}^{1d}| + a) \widehat{\mathbf{R}_{i-1}^{1d}} & \text{if } i \text{ is odd} \end{cases},$$

$$f(\mathbf{R}_{i-1}^{1d}, \theta_{1d}) = |\mathbf{R}_{i-1}^{1d}| \cos(\theta_{1d}/2) + \sqrt{(a)^2 - |\mathbf{R}_{i-1}^{1d}|^2 \sin^2(\theta_{1d}/2)}.$$

Here, $\widehat{\mathbf{R}}_{i-1}^{1d}$ is the unit vector in the direction of \mathbf{R}_{i-1}^{1d} . We still assume that the distance along the middle of the GNR remains unchanged, and therefore $\theta_{1d} = \Theta|\mathbf{a}'|/(W/2)$. If we follow this recursion until $\mathbf{R}_{2N_u}^{1d}$, where N_u is the number of A sites in the 1D unit cell, we have generated the deformed 1D unit cell \mathbf{R}_i^{1d} . However, we started with \mathbf{R}_1^{1d} defined in terms of the bent GNR width W' , which was unknown. We can now use the identity $W' = |\mathbf{R}_{2N_u}^{1d}| - |\mathbf{R}_1^{1d}|$, which is an equation with W' on both sides, to write out the recursion explicitly. However, this is a rather involved equation. We can, on the other hand, easily find a good approximation iteratively for W' . We start with the assumption that $W' \approx W$. Then, after running the recursion, we calculate the W' of that ribbon. If it differs by more than a set test value, we use that value of W' to generate a new unit cell. This iterative procedure runs until the test condition, that gives the minimal difference between a new and old width, is satisfied. Note also that this deformation does not work for every Θ , as for large enough bending the square root in the definition will become complex. This is understandable, as there should be a maximum bend when the lattice sites on the outer edge of the ribbon are all separated by a . Once the bent unit cell is generated, the complete bent GNR is obtained by copying the unit cell through multiples of rotations by θ_{1d} . Thus, we can describe the bondlength-preserving bending as

$$d^b(\mathbf{R}_i^{1d} + t\mathbf{a}_{1d}, \theta_b) = \mathcal{R}_{-t\theta_{1d}}\mathbf{R}_i^{1d}. \quad (4.3)$$

Here, $t \in \{1, \dots, N_{1d}\}$ and we explicitly used that the lattice sites of a GNR can be described by a site in the 1D unit cell plus a multiple of \mathbf{a} . One can show, using simple trigonometry, that each site now has 3 neighbors that are at a distance equal to a . Due to the construction, it is obvious that the discrete rotational symmetry is satisfied.

In a similar fashion, we can construct a bondlength-preserving bending for an armchair GNR. We again recursively construct a bent 1D unit cell. For the construction, it is convenient to define a reference point $\mathbf{r}_0 = \frac{a}{2}(1, [\sin^{-1}(\theta_{1d}/2) + \tan^{-1}(\theta_{1d}/2)])$. The initial site is now $\mathbf{R}_1^{1d} = (a/2, R_b - W'/2)$. The recursive relation to generate the bent unit cell is

$$\mathbf{R}_i^{1d} = \begin{cases} \mathbf{r}_0 + f(\mathbf{R}_{i-1}^{1d} - \mathbf{r}_0, \theta_b)\mathcal{R}_{-\theta_{1d}/2} \begin{pmatrix} 0 \\ 1 \end{pmatrix} & \text{if } i \text{ is even,} \\ \mathbf{r}_0 + f(\mathbf{R}_{i-1}^{1d} - \mathbf{r}_0, \theta_b) \begin{pmatrix} 0 \\ 1 \end{pmatrix} & \text{if } i \text{ is odd.} \end{cases}$$

Here, f is the same as for the zigzag case. We follow this recursion until $\mathbf{R}_{N_u}^{1d}$, which yields one half of the unit cell. The other half is obtained by the mirror reflection of the generated lattice points through the y -axis. We now use the same iterative process presented in the zigzag case to determine W' . Lastly, a description of the entire ribbon is obtained using Eq. (4.3). Also here, one

can show that each lattice site has three neighbors, which are separated by a distance a , and that the discrete rotational symmetry is satisfied.

4.2 Tight-binding model of bent graphene nanoribbons

As stated before, the bending deformations that we consider satisfy $\mathbf{F}_\theta(\mathbf{r}+\mathbf{a}) = \mathcal{R}_{\theta_{1d}}\mathbf{F}_\theta(\mathbf{r})$. Therefore, the Hamiltonian commutes with the rotation operator that rotates coordinates by θ_{1d} . This symmetry allows us to assume a 1D Bloch-type wavefunction for a bent GNR, given by

$$\psi_k(\mathbf{r}) = \sum_{t,n} e^{itk} c_{\mathbf{k},n} \phi(\mathbf{r} - \mathcal{R}_{-t\theta_{1d}}\mathbf{R}_n'^{1d}). \quad (4.4)$$

where $k \in [0, 2\pi]$, n runs over the atoms in the bent unit cell $\mathbf{R}_n'^{1d} = \mathbf{F}_\theta(\mathbf{R}_n^{1d})$, and t runs over the number of unit cells in the ribbon. Note that we do not distinguish here between A and B lattice sites. Thus, even though the 1D translational symmetry of the nanoribbon is broken by bending, for lattice-preserving bending we can define a quantum number k that allows us to reduce the complexity of our equations in the same way as done for straight ribbons. The k here defined can be directly compared to the k defined in Section 3.2, and for this reason we have chosen to use the same parameter. In Appendix C, a more general corollary of Bloch's theorem is obtained for the so-called lattice-preserving transformations of which a lattice-preserving bending is a special case. In App. C, it is shown that for this type of transformations the eigenstates can always be expressed using a continuous quantum number $k \in [0, 2\pi]$.

From the time-independent Schrödinger equation, we can derive a matrix equation for the vector of orbital components $c_{\mathbf{k}}$ and the corresponding secular equation,

$$(s_k^\theta)^{-1} t_k^\theta c_{\mathbf{k}} = (E_k^\theta - \epsilon_0) c_{\mathbf{k}}, \quad (4.5)$$

$$\det[t_k^\theta - (E_k^\theta - \epsilon_0) s_k^\theta] = 0. \quad (4.6)$$

Here, t_k and s_k are $2N_u \times 2N_u$ matrices with components

$$s_{k,mn}^\theta = \sum_t e^{ikt} s(\mathcal{R}_{-t\theta_{1d}}\mathbf{R}_m'^{1d} - \mathbf{R}_n'^{1d}), \quad (4.7)$$

$$t_{k,mn}^\theta = \sum_t e^{ikt} t(\mathcal{R}_{-t\theta_{1d}}\mathbf{R}_m'^{1d} - \mathbf{R}_n'^{1d}), \quad (4.8)$$

where t and s are defined as in Eq. (2.14).

4.3 Spectra of bent graphene nanoribbons and comparison with uniform strain

We have calculated the dispersion relations for bent GNRs by solving Eq. (4.6) numerically. This was done both, for width-preserving and for bondlength-preserving bending. In Fig. 4.3, the dependence of the dispersion relation for a ZGNR on the bending parameter is depicted, whereas in Fig. 4.4 this dependence is shown for an AGNR. We will first discuss two general observations that can be deduced from these figures. Then, we will calculate the spectra for uniform strained ribbon, in order to better analyse the results from curvature. Afterwards, we will perform two in-depth analyses. The first is an analysis of the dependence of the bandgaps for AGNRs. The second and most elaborate analysis will be done on the effect of bending on the edge states of ZGNRs.

Let us start with some general remarks. By inspecting Fig. 4.3 and Fig. 4.4, one can observe two effects. The first is a general deviation with respect to the straight dispersion. This deviation, though not everywhere well pronounced or even visible, holds for all bands and at every point in the BZ. This effect is comparable to what happens to the bands when one applies a uniform strain to the ribbon. For a uniform strain, however, all bands generally will move in the same direction, whereas for bending some bands move up and some move down. A more careful treatment of uniform strain is given in the next section. In most cases, the sign of the uniform strain determines whether the absolute energy of a band increases or decreases. A positive strain (stretching) results in a lower absolute energy and a negative strain (compression) leads to an increase in absolute energy. However, as will be shown later, already for uniform strain some bands in AGNRs behave contrarily to this general rule. The difference between the uniform case and the bending is explained by the fact that for a bending deformation, the strain is not uniform. In the outer part of the ribbon, bending causes a positive strain; in the middle there, is a point with no strain, whereas in the inner part the strain is negative. Whether the energy of a state is increased or decreased depends on where they are localised. In general, thus, we expect states that increase (decrease) the absolute value of their energy to be localised more on the inside (outside) part of the ribbon. Interestingly, we can thus learn something about the spacial localisation of a state from studying the effects of a bending deformation on the dispersion and knowing how a reference uniform-strain system behaves.

The second effect that we can observe from looking at Fig. 4.3 and Fig. 4.4 is the splitting of band crossings. Bending seems to lift many of the band degeneracies. This is especially visible at the edge states of the zigzag ribbons, which become significantly gapped already for relatively small bending angles. Because bending breaks the symmetry between the two edges, it can lift these degeneracies. It is interesting to note that some degeneracies are much less sensitive to bending effects than others. This is especially visible in the AGNR

spectrum, Fig. 4.4. Degeneracies that are more stable with respect to bending are expected to be more due to the other symmetries in the ribbons, like the sublattice symmetry. Next to splitting, one can also observe that some degeneracies move their position in k space. It is also curious that the robustness of some degeneracies with respect to bending depends substantially on the bending methods. In particular, the bondlength-preserving bending seems to preserve some degeneracies that the width-preserving bending breaks. This suggests that these degeneracies are possibly more related to the sublattice symmetry, which is preserved more significantly in the bondlength-preserving bending than in the width-preserving bending geometry.

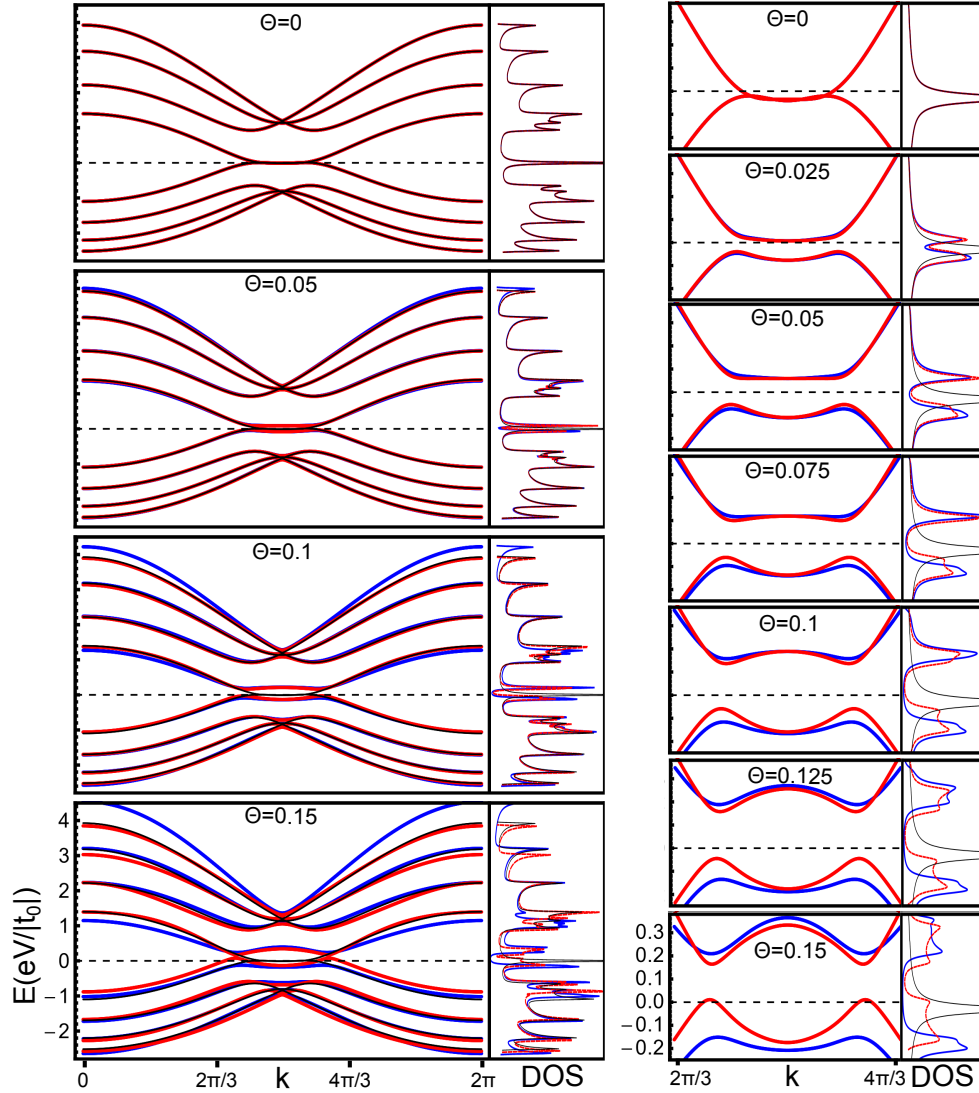


Figure 4.3: Dispersion relations and DOS for a $N = 4$ ZGNR as a function of the bending parameter Θ for width-preserving bending (blue) and bondlength-preserving bending (red). The thin black line corresponds to a straight ribbon. On the left side, we show the spectrum over the complete BZ , for Θ varying from 0 at the top to 0.15 on the bottom panel, with steps of 0.05. On the right side, we zoom in on the edge state with k ranging from $2\pi/3$ to $4\pi/3$, for Θ varying from 0 at the top to 0.15 on the bottom panel, with steps of 0.025. All pictures have the same scale as shown in the bottom. Calculations were made using non-orthogonal parameters with exponential decay, given by Eq. (2.21), and using $s_0 = 0.2$, $\kappa = 2.6$, and ϵ_0 such that the Fermi energy (dotted line) of the straight ribbon lies at zero. The DOS is calculated using a Lorentzian broadening with a width of 0.03 eV (DOS normalized to 1).

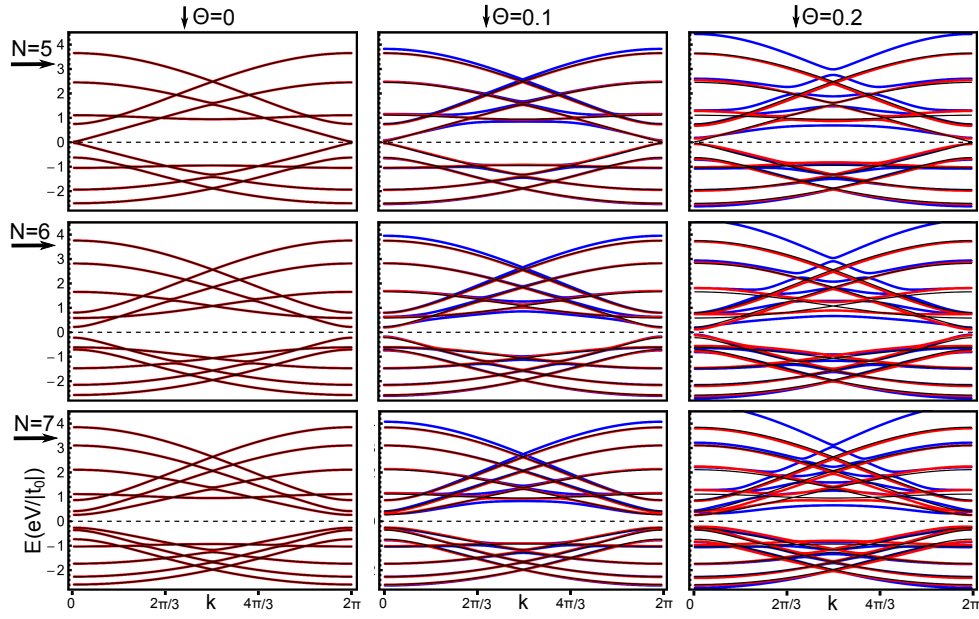


Figure 4.4: Dispersion relations for $N = 5, 6, 7$ AGNR as a function of increasing bending parameter Θ for width preserving bending (blue line) and bondlength-preserving bending (red). The thin black line corresponds to a straight ribbon.. On the top row is shown the spectrum over the complete BZ of a $N = 5$ AGNR and Θ varying from 0 at the top to 0.2 on the bottom picture, with steps of 0.1. The middle row the same for a $N = 6$ AGNR and the bottom for $N = 7$ AGNR. Calculations were made using non-orthogonal parameters with exponential decay, Eq. (2.21), $s_0 = 0.2$, $\kappa = 2.6$, and ϵ_0 such that the Fermi energy (dotted line) of the straight ribbon lies at 0.

Comparison with uniform strain

It is interesting to compare the obtained spectra with spectra obtained from a simple uniform strain in the longitudinal direction. We assume here a strain that is purely longitudinal and does not induce a variation in the transverse direction of the ribbon. This implies that we can write the deformation function as

$$F^\epsilon(\mathbf{r}, \epsilon) = \begin{pmatrix} 1 + \epsilon & 0 \\ 0 & 1 \end{pmatrix} \mathbf{r}, \quad (4.9)$$

with ϵ parameterizing the strain. For negative values bigger than -1 it shrinks the ribbon uniformly in the x -direction (for $\epsilon = -1$ exactly all points are shrunk to the same x coordinate), while for positive values it expands the ribbon in the x -direction. This deformation is a lattice preserving deformation as defined in Eq. (C.2). Therefore we can do a tight-binding calculation on the ribbon when this deformation is applied in an analogous manner as for bent GNR. In fact a uniform strain completely preserves translational symmetry and we can write a reciprocal space for it, so we do not necessarily need to invoke the Bloch's theorem for lattice preserving deformations.

Uniform strain in zigzag ribbons

Fig. 4.5 depicts the effect of positive and negative strain on a $N = 4$ ZGNR. We can see that indeed a negative strain, where lattice sites are brought closer together, results in raising of the absolute value of the energy of all the states. A positive strain, on the other hand, lowers the absolute value of the energy. This effect occurs for all states except for state in the valence bands around the band crossing point at $k = \pi$. Therefore, a raising or lowering of the energy of a state corresponds to a respectively negative or positive strain, as asserted in the previous section.

We now consider the effect of uniform strain on the edge states. We can see that the energy of the edge states increases (decreases) for negative (positive) strain. In fact when we compare these two cases with a ribbon bent using width preserving bending, we can see that the edge states with energy increased after bending agree quite well with the edge states experiencing uniform strain $\epsilon = -0.1$. It is important to note that the dispersion of the top edge states after bending is opposite to those of $\epsilon = -0.1$. On the other hand the edge states with energy decreased after bending agrees well with the edge states experiencing uniform strain $\epsilon = 0.1$. These observations indicate that the dispersion of ribbons bent by Θ is quantitatively related to the dispersion of a uniformly strained ribbon with strain $\epsilon = \pm\Theta$. We can understand this as it has been pointed out earlier that $\epsilon_{in} \approx -\Theta$ and $\epsilon_{out} \approx \Theta$. We are therefore led to think that the edge state decreasing in energy after bending is localised on the outside of the ribbon (experiencing strain Θ) and that the edge state increasing in energy after bending is localised on the outside of the ribbon

(experiencing strain $-\Theta$). This is an example of the principle mentioned before that we can infer the localisation of a state by comparing with uniform strain. Indeed we will later show by direct investigation of the components of the edge state that the lower E edge state is localised on the outside and the higher E edge state is localised on the inside.

Uniform strain in armchair ribbons

Fig. 4.6 depicts the effect of positive and negative strain on $N = 5, 6, 7$ AGNR, respectively representatives of type III, I and II AGNRs, as defined in Sec. 3.2. Similar behaviour as for uniformly strained ZGNR can be observed, with negative strain causing a general increase in energy and positive a decrease.

We first consider the $N = 5$ ribbon which belongs to the metallic (in a NN tight-binding model) type III. For negative strain, we see that all bands act as expected, except the second conduction and second valence band. This is visible at the boundaries of the BZ where we can see that the second conduction band remained almost the same but moved slightly down (opposite to all the other bands) and the second valence band clearly moved up close to the boundaries of the BZ . For positive strain we can see that not only these two bands behave opposite to the general shift down but also the first conduction and first valence band behave opposite close to the boundaries of the BZ . This behaviour obviously has effect on the bandgap, namely for big enough negative strain the initially second conduction and valence band will become the first valence and conduction band and will thus determine the bandgap. It might thus be the case that first the bandgap will increase and later decrease again. For positive strain we can observe a bandgap opening due to the anomalous movement instead of a closing.

Next consider the $N = 6$ AGNR of type I. For negative strain we see that the first and third conduction and valence bands behave anomalous. Therefore the bandgap decreases. Also for positive strain it are these band that behave anomalous causing an initial increase of the bandgap and a later decrease, when the second band takes over determining the band.

Finally consider the $N = 7$ AGNR of type II. For negative strain the second and third band which behave anomalously, in fact for $\epsilon = -0.1$ the initially second band already took over determining the bandgap. Also this has the effect that the bandgap gets smaller. It could however have been, in contrast to the type II bandgap, be preceded by a slight increase in the bandgap when the second band didn't yet take over from the first band. Also for positive strain the second and third behave anomalously. Because the first band behaves as expected for positive strain it decrease the bandgap.

We have thus seen that the different types of AGNR respond quite differently with respect to strain. This is especially visible at the bandgap. In the middle picture of Fig. 4.7 we can see a graph of the bandgap with respect to the longitudinal strain ϵ_x for the three types of AGNR. Indeed we

can see the behaviour described above and the points where the slope of the bandgap changes discontinuously are points where another band takes over determining the bandgap. Also in Fig. 4.7 a graph is shown for strain in the transverse direction ϵ_y , we can see that approximately the bandgap for a certain ϵ_y corresponds to $-\epsilon_x$. Though not shown here this behaviour is repeated for wider ribbons, the anomalous behaving bands are determined by the type of AGNR. This extensive analysis will help us interpret the effect of bending on the bandgap of AGNR.

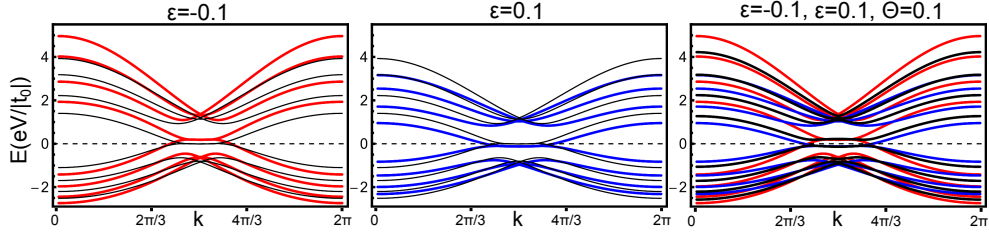


Figure 4.5: Dispersion relations and DOS for a $N = 4$ ZGNR for increasing uniform strain $\epsilon = -0.1$ (left picture, red line) and $\epsilon = 0.1$ (middle picture, blue line). The thinner black line corresponds in the left and middle picture corresponds to the straight ribbon. The right picture shows the $\epsilon = -0.1, 0.1$ (red, blue) and the dispersion after width preserving bending for $\Theta = 0.1$ (black). Calculations were made using non-orthogonal parameters with exponential decay, Eq. (2.21), using $s_0 = 0.2$, $\kappa = 2.6$, and ϵ_0 such that the Fermi energy (dotted line) of the straight ribbon lies at 0.

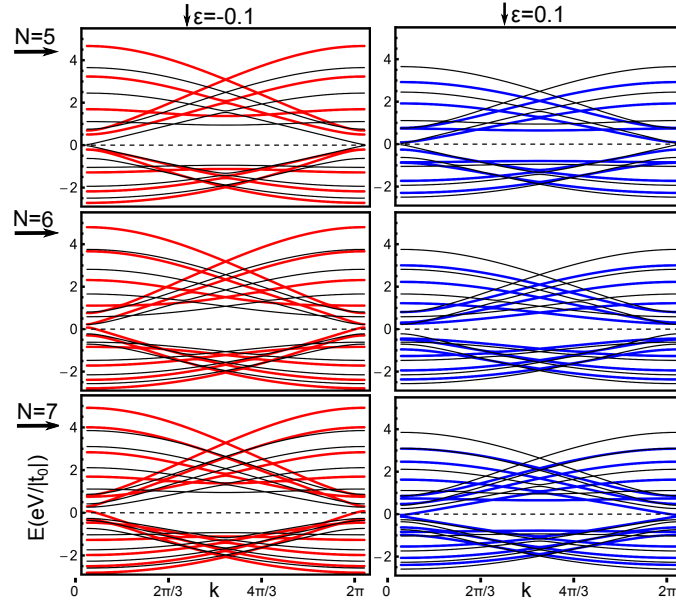


Figure 4.6: Dispersion relations for $N = 5, 6, 7$ AGNR for uniform strain $\epsilon = -0.1$ (left column, red line) and $\epsilon = 0.1$ (right column, blue line). The thinner black line corresponds to the straight ribbon. Calculations were made using non-orthogonal parameters with exponential decay, Eq. (2.21), using $s_0 = 0.2$, $\kappa = 2.6$, and ϵ_0 such that the Fermi energy (dotted line) of the straight ribbon lies at 0.

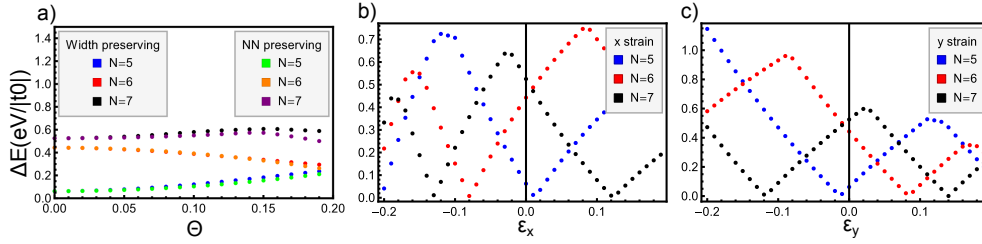


Figure 4.7: a) dependence of bandgap on bending angle for a $N = 5, 6, 7$ AGNR and for width preserving and NN preserving bending. b) Dependence on uniform strain in the x-direction (longitudinal direction). c) Dependence on uniform strain in the y-direction (transverse direction). All data are obtained using our standard set of exponentially decaying non-orthogonal hopping parameters.

4.4 Bent armchair ribbons: Band-gap behaviour

The dependence of the bandgap of AGNRs on bending was studied using a DFT-TB method in Ref.[13]. We considered this problem using our tight-binding model and the two ways of bending. The results are shown in Fig. (4.7). We have taken again the three representatives $N = 5, 6, 7$. We observe that for increased bending the bandgap behaves in the following way:

- For type I ($N = 6$) the bandgap decreases
- For type II ($N = 7$) the bandgap increases slightly and later decreases
- For type III ($N = 5$) the bandgap increases

This behaviour is pretty independent of the two methods of bending. Observe that the behaviour is qualitatively similar to small values of negative longitudinal strain or positive transverse strain, also shown in Fig. (4.7). It is as if the ribbon on the whole experiences an average compressive longitudinal strain.

One thing to note is that the effect is not very big. For $\Theta = 0.1$, which is already a sizeable curvature, the changes are of the order 0.05 eV. We should therefore be careful to infer experimentally observable effects from this prediction. Because it is a small effect it will probably be sensitive to details of the geometry and other electronic effects that are not taking into account in tight-binding.

We can compare our result to the experimental results obtained in Ref. [12] and shown in Fig. 1.2. Note that the units relate to each other by $(1[\text{nm}^{-1}] \approx 0.01[\Theta])$, so the experiments only bent to around $\Theta = 0.02$. The experiments show a type II AGNR (with $N = 7$) of which the bandgap decreases by 3%

after $\Theta \approx 0.02$. Our tight-binding model however predicted an increase. However these changes are small, and the experimental results are still tentative, predicting them exactly would require a subtle and detailed description of the situation. We for instance in our model did not take into account the fact that the sample is situated on a substrate. Also a small difference in the geometry can already give a big change in the predicted effect.

To elucidate the effect of a change in bending geometry it is interesting to compare our results to the one in Ref. [13], obtained using first principle methods. The results in Ref. [13] show that for increasing bending the behaviour of the bandgap is similar in nature to a ribbon that is experiencing a small *positive* longitudinal strain. Our model however predicts that it is similar to a small *negative* longitudinal strain.

The reason for this is probably the different bending geometries used. In Ref. [13] it is stated that their ribbon (the geometry of which is energetically optimized using first-principle calculations) experiences on average a longitudinal strain of $\epsilon_{avg} = \frac{1}{2}\gamma\Theta'^2 \approx \frac{1}{2}\gamma\Theta^2$ with $\gamma = 1.7$, which is positive. It is also mentioned that this stretching effect is the dominant observable effect. Therefore it is not unreasonable that their bandgap behaviour mimics that of a ribbon experiencing uniform positive longitudinal strain. The two bending methods we considered however do not have that big of a positive average strain because we required that the length of the ribbon after bending equals the length before. In fact for the width preserving bending $\epsilon_{avg} = 0$, for the bondlength-preserving bending ϵ_{avg} is slightly positive. Indeed when we look closely we can see that the bondlength-preserving bending shows signs of behaving more similarly to the positive longitudinal strain case than the width preserving bending. We can argue further that in fact it is not unreasonable for us to observe effects similar to $\epsilon_{avg} < 0$ because our relation between strain and hopping is not a linear one but an exponential one. Therefore bond-lengths that get decreased receive a stronger weight when a comparison between a uniform strain is attempted. In this way it can be qualitatively argued that an effective compression is not unlikely.

For a future study it will be good to attempt to change our bending method to see if the first principle results can be reproduced using our tight-binding theory.

We can conclude that the effects of bending on the bandgap are not very big and are sensitive to the exact geometry. The underlying reason for this is that the states that are responsible for the bandgap of AGNRs are bulk states. These are not very sensitive to symmetry breaking between bottom and top edge induced by bending. However in some experimental situations it might be easier to bent a ribbon than to uniformly stretch or compress it. If effects similar to uniform strain in AGNRs are desired it is therefore also an option to bent.

4.5 Bent zigzag ribbons: Edge state dispersion

Also ZGNRs were studied using a DFT-TB method in Ref.[13]. It was found that the most important effect is on the edge states which split and this effect is dominated by the broken symmetry between the edges (in contrast to the effect of stretching). We considered this problem using our tight-binding model and the two ways of bending. We find that we agree with the prediction of Ref.[13] but go further by describing an effective emerging 1D band structure for the edge states.

We have seen in Fig. 4.3 that the edge states split into a band with higher energy and a band lower energy. In Fig. 4.5 we see that the band that goes up in energy is similar to edge states experiencing negative uniform strain whereas the one that goes down in energy is similar to edge states experiencing positive uniform strain. As mentioned before this is observed for both bending methods and therefore we expect that the top band after bending corresponds to localised states on the inner edge of the ribbon and the lower band to states localised on the outer edge. We can confirm this by looking at the real space depiction of the edge state wavefunction in Fig. 4.8.

An even more striking observation from Fig. 4.3 is that the two states do not only split but also develop an opposite dispersion. The top band gets curved downward with the $k = \pi$ at a maximum, the lower band remains curved upwards with the $k = \pi$ point in a minimum. This contrasts to what we see for positive or negative uniform strain in Fig. 4.5. There the edge states get shifted but keep the same dispersion as the unstretched ribbon.

The minimal model to which we could compare the dispersion of the edge states which captures this behaviour is a 1D chain with a NN hopping and an on-site energy. We then use four effective parameters which will depend on Θ : There are two effective parameters for the higher energy band, $t^h(\Theta)$, $\epsilon_0^h(\Theta)$, and two for the lower energy band, $t^l(\Theta)$, $\epsilon_0^l(\Theta)$. The effective dispersion is then given by the 1D NN hopping dispersion

$$E_k^{h/l}(\Theta) = \epsilon_0^{h/l}(\Theta) + 2t^{h/l}(\Theta) \cos(k). \quad (4.10)$$

By just looking at Fig. 4.3 we expect that this can give quite a reasonable approximation of the dispersion of the edge states. A positive or negative $t^{h/l}$ relates to the dispersion that has a respectively upwards or downwards curved dispersion around π .

In Fig. 4.9 we have plotted the fitted parameters for various bending strain Θ . These fittings have been obtained using a relatively wide ZGNR of width $N = 14$, to avoid effects of hybridization across the ribbon. We can see that both the lower and the higher energy edge state start out with the same positive hopping parameter. However, the emergent band structure at the edge depends crucially on the type of bending. We will first discuss width preserving bending.

Effective parameters for width preserving and bondlength-preserving bending. For width preserving bending t^h initially increases slightly but from around $\Theta \approx 0.06$ it starts to decrease and even crosses the 0 for $\Theta \approx 0.16$. ϵ_0^h shows a behaviour approximately proportional to t^h . The t^l on the other hand decreases in a linear-like fashion. For $\Theta > 0.18$ t^l tends to zero for width preserving bending. However for such a high bending parameter the edge states hybridise with other bands. ϵ^l behaves again proportionally to t^l .

For bondlength-preserving t^h decreases approximately linear and crosses 0 for $\Theta \approx 0.12$. ϵ_0^h is again proportional to t^h but crosses 0 for $\Theta \approx 0.08$. t^l and ϵ^l on the other hand increase linearly.

The most striking difference between the two bending methods is thus that for the lower edge state an opposite development of the effective parameters with bending is observed. The two bending methods agree that the higher edge state effective parameters decrease and even become 0 for increased bending but width preserving does not show as much of a linear behaviour as bondlength preserving.

A most important observation is that, in both bending schemes, t^h crosses zero. This means that for a certain bending parameter the band becomes dispersionless. This is an interesting observation as many-body effects can be expected to become important for that bending parameter.

The difference between bond-length and width preserving bending.

We would like to understand the difference between the two bending methods. One reason could be the fact that the width and bondlength-preserving bending schemes produce different strain on the edges (ϵ_{in} , ϵ_{out}). This is, as mentioned in section 4.9, because the bondlength-preserving bending decreases the width of the ribbon and thus has smaller values for ϵ_{in} , ϵ_{out} . To check if this explains the difference we have also plotted the effective fitted parameters directly against the strain (shown in the insets in Fig. 4.9). We can clearly see that this does not change the behaviour significantly and cannot explain the difference.

We can conclude from this that the difference in behaviour is solely due to the fact that the width preserving bending also perturbs the nearest neighbors. The complicated nonlinear behaviour is therefore due to the change of the nearest neighbor distance whereas changes in the higher distances cause a more linear behaviour.

At this stage it is useful to consider the localisation of the edge state. These are explicitly depicted the edge states in Fig. 4.8. Here the orbital components of the eigenstates of four edge states, $c_{t,n}$, as defined in Eq. (4.4), are plotted for increasing Θ . The width preserving bending scheme was used for these pictures. First, we note that the edge state are localised on one sublattice at each edge. With increasing bending we can see that states that were initially a combination between a state localised on one edge and a state localised on

the other are transformed into a high energy state localised on the inner edge and a low energy state localised on the outer edge. It is interesting to note that this process takes place already for the very small bending parameter of $\Theta = 0.0001$ we can see that the edge states start to become localised only on one edge. Another interesting observation is that for the $k = 7\pi/8$ states after bending the state on the inner edge shows a slower decay of intensity towards the middle as the state localised on the outer edge. It is not depicted here but a similar plot after bondlength-preserving bending would also show a slightly slower decay of intensity but the difference is smaller than for width preserving bending.

We can now understand better what to expect for the change of the edge dispersion and why there is a difference in the two methods. Because the edge states are localised on a single sublattice for each edge, we expect that a perturbation in the NN distance does have an effect mainly through the hybridization between the edge states on opposite sides (the two edge states are localised on different sublattices). This is a more complicated effect and it is therefore understandable that it appears in non-linear behaviour of the effective parameters for width-preserving bending. Also this effect will be very dependent on the width of the ribbon and is expected to decrease as the ribbon gets wider. A perturbation in the NNN hopping however has a more basic effect because it works on the energy of a localised edge state directly. Therefore we will here only attempt to explain the effect of the change in NNN hopping and focus on the results of the bondlength-preserving bending.

Understanding the effective parameters for bondlength-preserving bending. As has been stated for bondlength-preserving bending that effective hopping at the inner edge linearly decreases and changes sign whereas the hopping at the outer edge linearly increases. We could try to understand this behaviour by assuming a perfectly localised edge state. The inner edge experiences a negative strain, so the hopping will become more negative and the 1D dispersion would curve downwards. This indeed corresponds to what we observe in Fig. 4.9. Assuming a perfect localised edge state, the hopping at the outer edge will decrease because the distance increases and therefore a flat band should develop. However, for bondlength-preserving bending, the opposite behaviour is visible in Fig. 4.9. It is also good to remark that this argument would fail to predict the effective positive dispersion for straight ribbons as explained in Sec. 3.2. Still a perfect localisation gives the right prediction for the inner edge. This is because in that case the site at the complete inner edge experiences most strain and the amplitude of the wavefunction of the edge state will be the dominant one in determining how the energy will change. On the other hand at the outer edge the weight of the wavefunction on sites closer to the bulk become more important in determining the energy of the state. This is because at the complete outer edge the

atoms move away from each other, decreasing the hopping between them, and thus the amplitude of the edge state on the outer edge becomes less important in determining the energy. However the amplitude of the wavefunction on sites closer to the bulk become more important. Thus the fact that the edge state becomes less localised as it gets further from $k = \pi$ becomes more important. This enhances the effect that was already seen for straight ribbons and causes an increasing effective positive hopping. In conclusion we there is a competition between two effects due to NNN hopping and strain:

1. An effective positive hopping for increasing negative strain because of the increasing delocalisation nature of the edge state as it gets further from $k = \pi$.
2. An effective negative hopping for increasing negative strain because the edge state is localised in the first place.

For the edge state localised on the outer edge the first effect is always dominant and becomes even more dominant after bending. For the inner edge the second effect becomes dominant over the first after a certain bending parameter. This is also why the dispersion of the inner edge has to go through a point at which it is non-dispersive.

This qualitative argument explains the trends of the effective bondlength-preserving parameters. A careful perturbation theory would have to be done to make these statements quantitative.

We can conclude that bending has an interesting effect on the edge states. The effects are more pronounced than those for AGNRs because the effect is due to the breaking of the symmetry between the edges whereas the effects for AGNRs (at least for the bandgap) were dominated by the average stretching or compression of the ribbon. Experimentally it would therefore be probably more interesting to study the effects of bending on ZGNRs rather than AGNRs.

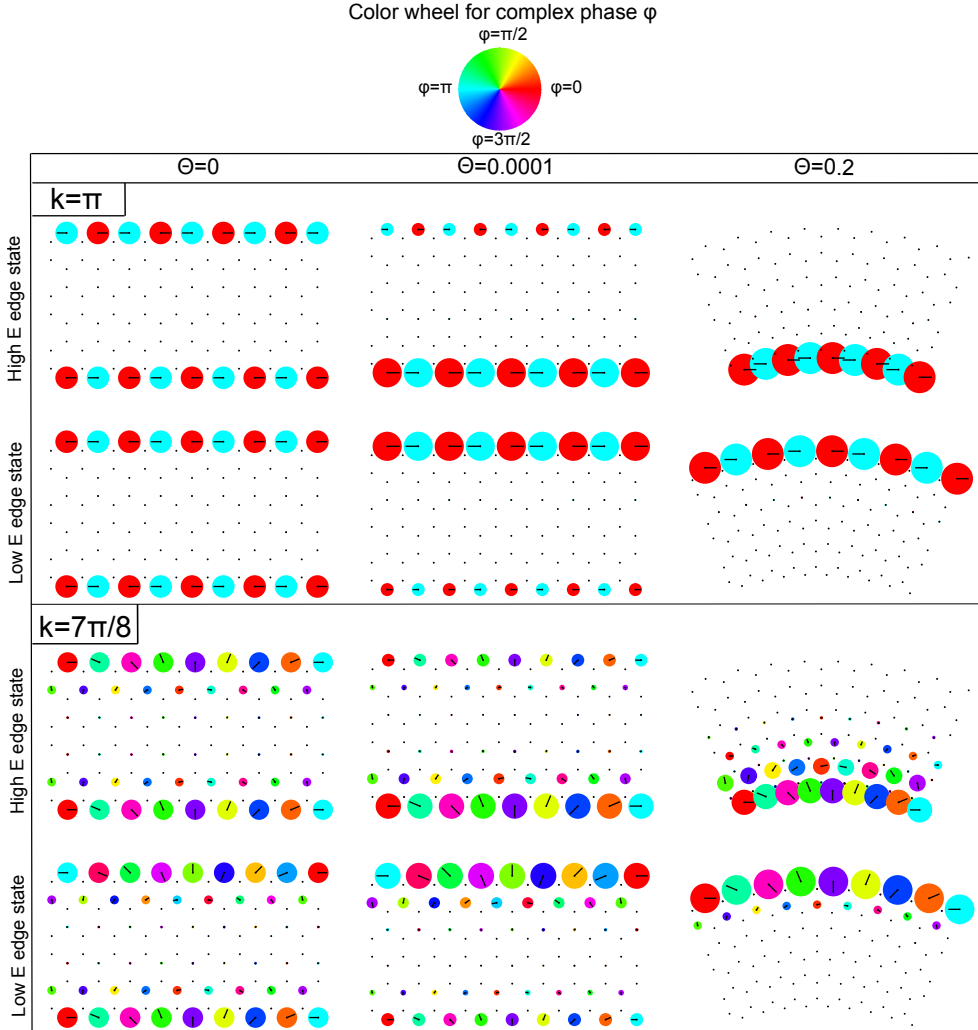


Figure 4.8: Edge states in the real space: Components $c_{t,n}$ of edge states for a section of the ribbon at $k = \pi$ and $k = 7\pi/8$ mapped to the corresponding \mathbf{r}_i points of the bent GNR for different bending parameter values Θ . The width preserving bending scheme was used here in combination with our standard orbital hopping parameters. $c_{t,n}$ are related to the eigenvector through the definition Eq. (4.4) and satisfy Eq. (4.5). The diameter of the disk is proportional to the absolute value of $c_{t,n}$ and the color to the phase is determined by the color wheel, one can also look at the little black lines at each point which are complex vectors that are proportional to $c_{t,n}$. The phase is chosen such that the lower left lattice site has phase zero. The top rows of the $k = \pi$ and $k = 7\pi/8$ panels correspond to the high energy edge state and the bottom to the lower energy edge states.

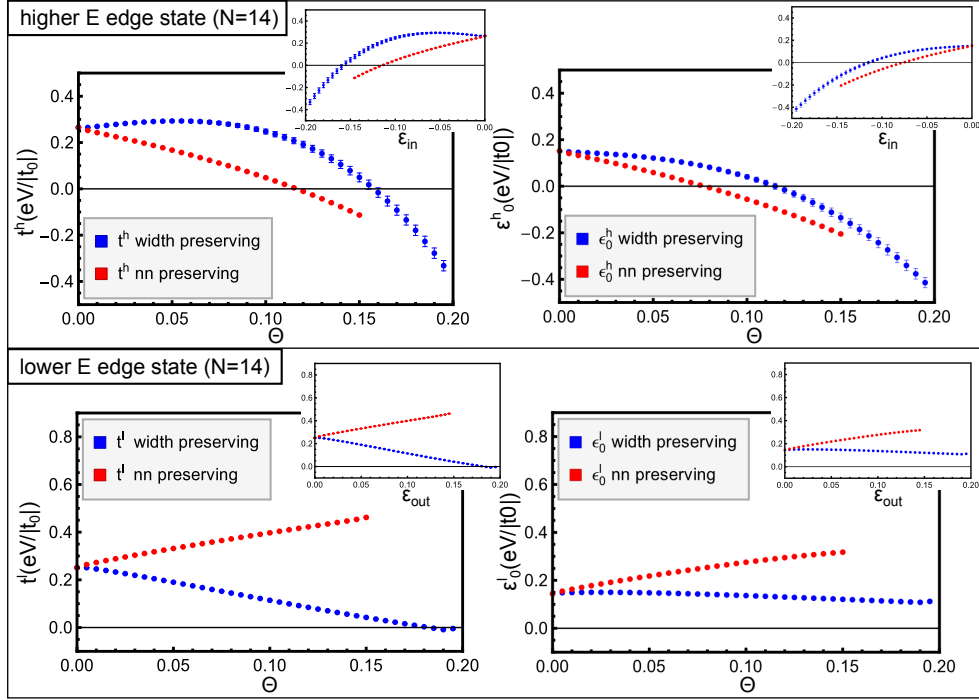


Figure 4.9: Fittings of the effective 1D parameters t^h, ϵ_0^h (upper rectangular panel) and t^l, ϵ_0^l (lower rectangular panel) versus the bending parameter Θ . These parameters are defined in Eq. (4.10). Fittings have been made for width-preserving bending (blue dots) and bondlength-preserving bending (red dots). The insets of each panel show these parameters with respect to the strain on the inner edge ϵ_{in} for the higher energy edge state and with respect to the strain on the outer edge ϵ_{out} for the lower energy edge states. The relation between $\epsilon_{in}, \epsilon_{out}$ and Θ is as explained in section . Fittings were done for a ZGNR of width $N = 14$, and are based on data points chosen in the region around π given by $k \in [2.41, 3.86]$. Error bars are obtained from the standard deviation between the fitted spectra and the numerics on the lattice. All calculations were done using our standard set of exponentially decaying orbital hopping parameters.

Chapter 5

Continuum model for bent graphene nanoribbons

In this chapter we introduce the Dirac fermion description of graphene. We review the treatment of ZGNRs and AGNRs using boundary conditions in combination with the Dirac equation. We then introduce a gauge field that effectively acts as a strain. This gauge field results in a pseudo-magnetic field preserving time-reversal symmetry. We will argue that the width preserving bending results in an approximate constant pseudo-magnetic field in this description. Then we solve the Dirac equation including this constant pseudo-magnetic field using the ZGNRs and AGNRs boundary conditions. Both turn out to be exactly solvable using special functions but their dispersion is expressed in terms of difficult transcendental equations. The ZGNR dispersion is still solvable using simple algorithms however the AGNRs dispersion turns out to be too difficult. However the results of the ZGNR do not obviously compare with results obtained from our tight-binding calculations, and we discuss reasons for this behaviour.

5.1 Dirac fermions in graphene

Next to the tight-binding description graphene's electronic properties are often described using a continuum model. This continuum model is only valid for electrons close to the Fermi surface and is given by a massless Dirac Hamiltonian in 2 dimensions. This is the reason that electrons in graphene are often described as massless Dirac fermions. Usually this effective continuum model is derived from a NN tight-binding model with orthogonal basis state. This effective model is however also valid for the tight-binding model with non-orthogonal basis states and higher neighbor hopping, at least if we only consider NN and NNN hopping and NN overlap. The tight-binding model was reduced to solving the matrix equation Eq. (2.17) which produces the dispersion $E_{\mathbf{k}}^{\lambda}$ given by Eq. (2.18). We will first show that the K_{\pm} points lie

on the Fermi surface. Because the nearest neighbor hopping terms are dominant $E_{\mathbf{k}}^- \leq E_{\mathbf{k}}^+$. The Fermi surface is therefore given by points \mathbf{k} in which $H(\mathbf{k}) = 0$, where $H(\mathbf{k})$ is the function defined in Eq. (2.19). To prove that this is zero we look at $f_n(K_{\pm})$ for each n , where $f_n(\mathbf{k})$ is as defined in Eq. (2.5). It will be convenient to define

$$\tilde{f}_n(\mathbf{k}) = e^{-i\mathbf{k} \cdot (\delta_B - \delta_A)} f_n(\mathbf{k}) = \sum_{\langle l \rangle_n} e^{-i\mathbf{k} \cdot \mathbf{r}_l^B}, \quad (5.1)$$

where \mathbf{r}_l^B are points in the B sublattice such that $|\mathbf{r}_l^B| = d_n$ for some constant distance d_n . Because of the lattice symmetries then also $|\mathcal{R}\mathbf{r}_l^B| = |\mathcal{R}^2\mathbf{r}_l^B| = d_n$, where $\mathcal{R} = \mathcal{R}_{-2\pi/3}$ is the clockwise rotation matrix that rotates by $2\pi/3$. These are all distinct so the sum in \tilde{f}_n over $\langle l \rangle_n$ should include these points at least. Suppose we have only one of such a triplet, then we can write

$$\tilde{f}_n(\mathbf{k}) = \sum_{s=0}^{s=2} e^{-i\mathbf{k} \cdot \mathcal{R}^s \mathbf{r}_l^B}. \quad (5.2)$$

Now, $\mathbf{r}_l^B = i\mathbf{a}_1 + j\mathbf{a}_2 + (\delta_B - \delta_A)$ for some pair of integers i, j , $\delta_B - \delta_A = (\mathbf{a}_1 + \mathbf{a}_2)/3$, $K_{\pm} = \pm \frac{4\pi}{3|\mathbf{a}_1|^2}(\mathbf{a}_1 - \mathbf{a}_2)$. Using these identities we get

$$\begin{aligned} \tilde{f}_n(K_+) &= \sum_{s=0}^{s=2} e^{-i \frac{4\pi}{3|\mathbf{a}_1|^2} (\mathbf{a}_1 - \mathbf{a}_2) \cdot \mathcal{R}^s \left((i + \frac{1}{3})\mathbf{a}_1 + (j + \frac{1}{3})\mathbf{a}_2 \right)} = \\ &= \sum_{s=0}^{s=2} e^{-i \frac{2\pi}{3} (i - j + 1 - s)} = 0. \end{aligned}$$

Because this is the hermitian conjugate also $\tilde{f}_n(K_-) = 0$. Thus we can conclude that K_{\pm} lies on the Fermi surface even if higher hoppings and overlaps are taking into account.

We now perform a linear approximation to the matrix hamiltonian of Eq. (2.17) but we will restrict this to NN hopping and thus only look at $f_1(\mathbf{k})$. We will expand the $f_1(\mathbf{k})$ function and not the $\tilde{f}_1(\mathbf{k})$ because it results in an easier effective hamiltonian [24].

$$\begin{aligned} f_1(K_+ + \mathbf{q}) &= 1 + e^{-i\mathbf{a}_1 \cdot \mathbf{K}_{\pm} + \mathbf{k}} + e^{-i\mathbf{a}_2 \cdot \mathbf{K}_{\pm} + \mathbf{k}} \approx -i(e^{-i\mathbf{a}_1 \cdot \mathbf{K}_{\pm}} \mathbf{a}_1 \cdot \mathbf{k} + e^{-i\mathbf{a}_2 \cdot \mathbf{K}_{\pm}} \mathbf{a}_2 \cdot \mathbf{k}) = \\ &= -\frac{3a}{2}i(\mathbf{k} \cdot \mathbf{a}_x (-e^{-i\mathbf{a}_2 \cdot \mathbf{K}_{\pm}} + e^{-i\mathbf{a}_1 \cdot \mathbf{K}_{\pm}}) / \sqrt{3} + \mathbf{k} \cdot \mathbf{a}_y (-e^{-i\mathbf{a}_2 \cdot \mathbf{K}_{\pm}} - e^{-i\mathbf{a}_1 \cdot \mathbf{K}_{\pm}})) = \\ &= -\frac{3a}{2}i(\mp i\mathbf{a}_x \cdot \mathbf{k} + \mathbf{a}_y \cdot \mathbf{k}) = -\frac{3a}{2}(\pm q_x + iq_y), \quad (5.3) \end{aligned}$$

where $\mathbf{a}_y = -(\mathbf{a}_1 + \mathbf{a}_2)/(3a)$ and $\mathbf{a}_x = (\mathbf{a}_1 - \mathbf{a}_2)/(\sqrt{3}a)$. So $\gamma(\mathbf{K}_{\pm} + \mathbf{k}, \phi) \approx \frac{3a}{2}e^{i\phi}(\pm \mathbf{k} \cdot \mathbf{a}_x + i\mathbf{k} \cdot \mathbf{a}_y)$. We have here chosen our coordinates such that the x-axis is parallel to \mathbf{a}_x and the y-axis parallel tot \mathbf{a}_y . Note that this is not the

same coordinate system as was defined in Fig. 2.1a. The most common form of the effective hamiltonian also has the A and B sublattices exchanged with respect to the basis we just defined. If we adopt the standard convention we arrive at the usual form of the effective hamiltonian,

$$\mathcal{H}_{\mathbf{q}}^{eff,\mu} = v_F \begin{pmatrix} 0 & \mu q_x - i q_y \\ \mu q_x + i q_y & 0 \end{pmatrix}. \quad (5.4)$$

Here we defined the Fermi velocity as $v_F = -\frac{3ta}{2}$ and t is NN hopping. We also introduced $\mu = \pm$ which denotes the linearization around the K_{\pm} point this degree of freedom is called the valley pseudospin. This indeed is the same hamiltonian as the massless dirac hamiltonian in 2 dimensions. If we replace $q_x \rightarrow -i\partial_x$ and $q_y \rightarrow -i\partial_y$ we arrive at the continuum real space dirac hamiltonian. We stress that it is with respect to a specific coordinate system that this hamiltonian is valid, this becomes important when we look at finite size systems because then we have to know the basis to describe the boundary condition. Namely, for Eq. (5.4) to hold we have to use the coordinates defined in Fig. 2.1a but then shifted 30° anticlockwise. We can combine the valley dependent Hamiltonian in one form working on the state $(\psi_A, \psi_B, \psi'_A, \psi'_B)^t$ by defining

$$\mathcal{H}_{\mathbf{q}} = v_F(\tau_z \otimes q_x \sigma_x + \tau_0 \otimes q_y \sigma_y). \quad (5.5)$$

Here σ_x and σ_y are the standard Pauli matrices, τ_z is the sigma-z matrix, τ_0 the identity two by two matrix and \otimes a tensor product between matrices. In fact it is possible and sometimes more convenient to write the Dirac Hamiltonian in the so-called valley isotropic form, it then works on the state $(\psi_A, \psi_B, -\psi'_B, \psi'_A)$ and is given by

$$\mathcal{H}_{\mathbf{q}}^{iso} = v_F \tau_0 \otimes \boldsymbol{\sigma} \cdot \mathbf{q}. \quad (5.6)$$

Here, $\boldsymbol{\sigma} = (\sigma_x, \sigma_y)^t$. It is useful to square this matrix,

$$\mathcal{H}_{\mathbf{q}}^2 = v_F^2 (q_x^2 + q_y^2). \quad (5.7)$$

From this we can calculate the energy dispersion,

$$E_{\mu}^{\lambda}(\mathbf{q}) = \lambda v_F |\mathbf{q}|. \quad (5.8)$$

Note the inclusion of both the *lattice pseudospin* λ and the *valley pseudospin* μ as degrees of freedom. The energy eigenstates are given by $\psi_{\mathbf{q},\lambda}^{\mu=+} = \frac{1}{2}(1, \lambda e^{i\phi_{\mathbf{q}}}, 0, 0)$ and $\psi_{\mathbf{q},\lambda}^{\mu=-} = \frac{1}{2}(0, 0, -\lambda e^{i\phi_{\mathbf{q}}}, 1)$, with $\phi_{\mathbf{q}} = \arctan(q_y/q_x)$.

5.2 Dirac fermions in straight ribbon geometry

We have shown that graphene at low energies is described by massless Dirac fermions. However we are mainly interested in GNRs in this thesis. So far we

studied the GNRs in a tight-binding model that was reduced to the matrix equations Eq. (3.8) and Eq. (4.5) for respectively straight and bent ribbons. The matrices in these equations are of size $2N \times 2N$. It is not obvious if we can derive a continuum model that approximates these equations as well. However, as it turns out this can be done by adding boundary conditions to the solutions of the Dirac equation [25]. These boundary conditions depend on the termination of the GNR. We will not try to motivate this directly from the tight-binding model but instead apply it to zigzag and armchair GNRs to demonstrate that this gives reasonable results.

Dirac fermions in zigzag nanoribbons

We can write the wave function in real space in the following spinor form:

$$\begin{pmatrix} \Psi_A(\mathbf{r}) \\ \Psi_B(\mathbf{r}) \end{pmatrix} = e^{i\mathbf{K}^+ \cdot \mathbf{r}} \begin{pmatrix} \psi_A(\mathbf{r}) \\ \psi_B(\mathbf{r}) \end{pmatrix} + e^{i\mathbf{K}^- \cdot \mathbf{r}} \begin{pmatrix} \psi'_A(\mathbf{r}) \\ \psi'_B(\mathbf{r}) \end{pmatrix} \quad (5.9)$$

Where ψ_A and ψ_B are spinor wave functions of hamiltonian $\mathcal{H}_{\mathbf{q}}^{eff,+}$ and ψ'_A and ψ'_B of $\mathcal{H}_{\mathbf{q}}^{eff,-}$ of Eq. (5.4) and $K_{\pm} = (\pm \frac{4\pi}{3\sqrt{3}a}, 0)$. In the coordinate system in which Eq. (5.4) holds a zigzag termination results in a translational symmetry along the x axis. Therefore we can write

$$\psi^{(\prime)}(\mathbf{r}) = e^{ik_x x} \begin{pmatrix} \phi_A^{(\prime)}(y) \\ \phi_B^{(\prime)}(y) \end{pmatrix} \quad (5.10)$$

Because of the zigzag edges have to use the boundary conditions (See Ref. [25] for motivation),

$$\Psi_A(y = L) = 0, \quad \Psi_B(y = 0) = 0. \quad (5.11)$$

It is important to not that here L is not the same as the L defined in chapter 4. From now on L as the length of the ribbon if one layer of atoms as added below and above the ribbon. For ZGNR this means that $L = (3N/2 + 1)a$. We can argue that these boundary conditions are reasonable because in our coordinate orientation we can position a zigzag ribbon with an extra row of B sites at the bottom and A at the top. Then the wavefunction at this added bottom and top row should be zero because these sites do not actually exist and should not contribute to the hopping. If we assume that this is the case we can combine Eq. (5.9) and (5.10) such that,

$$\phi_A(L) = \phi'_A(L) = \phi_B(0) = \phi'_B(0) = 0. \quad (5.12)$$

To get an expression for $\phi(y)$ we use that they are eigenfunctions of the Hamiltonian (5.6) and the squared Hamiltonian (5.7). In the position representation we exchange q_y for $-i\partial_y$ and q_x for $k_x - i\partial_x$. This results in the differential equations

$$\begin{aligned} (-\partial_y^2 + q_x^2)\phi_B &= \tilde{E}^2\phi_B, & \tilde{E}\phi_A &= (q_x - \partial_y)\phi_B, \\ (-\partial_y^2 + q_x^2)\phi_B &= \tilde{E}^2\phi_A, & \tilde{E}\phi_B &= (q_x + \partial_y)\phi_A, \end{aligned} \quad (5.13)$$

where $\tilde{E} = \frac{E}{v_F}$. And similar for the K' valley with q_x replaced by $-q_x$. Using the boundary conditions we can see that if $\tilde{E} = 0$, ϕ_A and ϕ_B only have the trivial solution which is non-normalizable. If $\tilde{E} \neq 0$ the solution has the form

$$\phi_B = Ae^{zy} + Be^{-zy} \quad \text{with} \quad \tilde{E}^2 = q_x^2 - z^2. \quad (5.14)$$

Note that $z = 0$ also gives non-normalizable solutions, therefore we can assume $\tilde{E} \neq 0$ and $z \neq 0$. Thus from the boundary conditions $A + B = 0$ and $(q_x - z)Ae^{zL} + (q_x + z)Be^{-zL} = 0$ which leads to an equation relating z to q_x

$$e^{-2zL} = \frac{q_x - z}{q_x + z}. \quad (5.15)$$

The solution to this transcendental equation determines the energy spectrum of the ribbon. If we split z in a real and imaginary part $z = \alpha + i\beta$, after rewriting we obtain two equations:

$$\begin{aligned} ((q_x + \alpha)^2 + \beta^2) \cos(\beta L) \sin(\beta L) &= \beta q_x e^{2\alpha L}, \\ ((q_x + \alpha)^2 + \beta^2) (2 \cos^2(\beta L) - 1) &= (q_x^2 - \alpha^2 - \beta^2) e^{2\alpha L}. \end{aligned} \quad (5.16)$$

This set of equations only has solutions when $\alpha\beta = 0$, otherwise E is imaginary. Therefore z is purely imaginary or purely real. Using this fact, we find two types of solutions:

$$\begin{aligned} e^{-2\alpha L} &= \frac{q_x - \alpha}{q_x + \alpha}, \quad \text{with} \quad \beta = 0, \\ q_x \sin(\beta L) &= \beta \cos(\beta L), \quad \text{with} \quad \alpha = 0. \end{aligned} \quad (5.17)$$

The purely real solutions correspond to the edge states and the purely complex solutions to the confined modes. These two equations can be solved numerically to give the spectrum depicted in Fig. (5.1). We have to calculate this spectrum only for one L . This is because a multiplication cL results in the same dispersion only with a rescaling of $E \rightarrow E/c$ and $q_x \rightarrow q_x/c$. In the semi-infinite case find that there are bulk states for each q_x of $E > q_x$ and edge states for all $q_x > 0$, with $E = 0$. The edge state are given in real space by

$$\begin{aligned} \phi_b(y) &\propto \sinh(zy), \\ \phi_a(y) &= -\text{sign}(\tilde{E})\phi_b(L - y). \end{aligned} \quad (5.18)$$

Because $e^{zL}(q_x + z)$ is positive we see that, when t is negative, an antibonding combination between an edge state on the A edge and B edge is the higher energy state and a bonding the lower energy state. We can apply the same procedure to ϕ' , which is obtained by $q_x \rightarrow -q_x$. Note that the ϕ and ϕ' solutions are independent solutions of the system. In Fig. 3.3 we compare the Dirac dispersion around K and K' to a NN tight-binding model. Close to $k = 2\pi/3$ and $k = 4\pi/3$ there is a fairly good agreement especially for low energies. Note that the edge state dispersion is reproduced rather well.

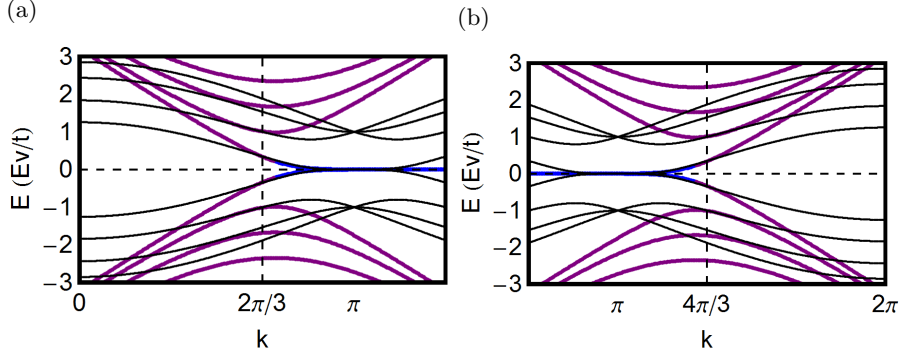


Figure 5.1: Dispersion obtained from the continuum description using zigzag boundary condition, Eq. (5.12). Here $L = 7$ and $v_f = 3/2$. The edge states correspond to the thick blue line, the bulk states are thick purple. The black line is the dispersion of a NN tight-binding model of an $N = 4$ zigzag ribbon with $t = -1$. The horizontal k axes lies in the 1D BZ of the ribbon. (a) The Dirac dispersion around the K point. We used that $q_x = k - 2\pi/3$ (b) Similar around the K' point, now $q_x = k + 2\pi/3$.

Armchair nanoribbons in linear approximation

For an AGNR there is translational symmetry in the y direction if we use the coordinate system for which Eq. (5.4) holds. That ensures that the spinor wave functions of Eq. (5.9) can be written as

$$\psi^{(\prime)}(\mathbf{r}) = e^{ik_y y} \begin{pmatrix} \phi_A^{(\prime)}(x) \\ \phi_B^{(\prime)}(x) \end{pmatrix} \quad (5.19)$$

In the armchair case the boundary conditions of the dirac equation are [25],

$$\Psi_A(x=0) = \Psi_B(x=0) = \Psi_A(x=L) = \Psi_B(x=L) = 0. \quad (5.20)$$

Here L now is the length of the AGNR plus two additional lines at the upper and lower edge of A and B sites, so $L = (N + 1)\sqrt{3}a/2$. Notice that now A and B are both zero at both edges in contrast to the boundary conditions of a zigzag ribbon. In terms of $\phi^{(\prime)}$:

$$\phi_{A/B}(0) + \phi'_{A/B}(0) = 0, \quad e^{iKL}\phi_{A/B}(L) + e^{-iKL}\phi'_{A/B}(L) = 0, \quad (5.21)$$

where $\mu = A, B$. From 5.4 we see that ϕ and ϕ' satisfy:

$$\begin{aligned} (-\partial_x^2 + q_y^2)\phi_B &= \tilde{E}^2 \phi_B, & \tilde{E}\phi_A &= (-i\partial_x - iq_y)\phi_B, \\ (-\partial_x^2 + q_y^2)\phi'_B &= \tilde{E}^2 \phi'_B, & \tilde{E}\phi'_A &= (i\partial_x - iq_y)\phi'_B. \end{aligned} \quad (5.22)$$

The corresponding solutions are,

$$\begin{aligned}
 \phi_B &= Ae^{iq_n x} + Be^{-iq_n x} \\
 \phi'_B &= Ce^{iq_n x} + De^{-iq_n x} \\
 \tilde{E}\phi_A &= (q_n - iq_y)Ae^{iq_n x} - (q_n + iq_y)Be^{-iq_n x} \\
 \tilde{E}\phi'_A &= -(q_n + iq_y)Ce^{iq_n x} + (q_n - iq_y)De^{-iq_n x}
 \end{aligned} \tag{5.23}$$

The dispersion is given by $\tilde{E}^2 = q_y^2 + q_n^2$. From the boundary conditions of Eq. (5.21) it follows that

$$\begin{aligned}
 A + D + B + C &= 0 \\
 \tilde{E}(A + D) &= 0 \\
 \tilde{E}A \sin((q_n + K)L) + \tilde{E}C \sin((q_n - K)L) &= 0 \\
 (q_n - ik_y)\tilde{E}A \sin((q_n + K)L) - (q_n + iq_y)\tilde{E}C \sin((q_n - K)L) &= 0.
 \end{aligned} \tag{5.24}$$

Using these equations reduce to $\tilde{E} \sin[(q_n + K)L] = 0$. If $\tilde{E} = 0$ we can derive that $q_n = q_y = 0$ and $\sin[(K)L]$. Therefore all solutions are given by, $\sin[(q_n + K)L] = 0$. In contrast to the zigzag case this is easy to solve exactly as the sine function equals zero only for real $q_n = \frac{n\pi}{L} - \frac{4\pi}{3a}$. In contrast to the zigzag case we do not get two separate dispersions for both valleys, but only one, because the K and K' valley mix due to the boundary conditions. Note also that the armchair ribbon does not have a simple scaling relation between L and E . Instead also this model reproduces the three types of ribbons that were discussed earlier in section 3.2. For instance ribbons with $N = 3r + 2$ are metallic. Fig. (5.2) shows the Dirac dispersion for AGNR for ribbons of length $N = 5, 6, 7$ representing the three types. The NN tight-binding model is shown for comparison. We observe that the correspondence is good only at exactly $k = 0$ and at the lower bands the dispersions. In general the tight-binding dispersion seems to increase slower as a function of k than the Dirac dispersion. Notice that the correspondence between the two dispersions is in general better for the zigzag case than for the armchair case.

5.3 Dirac equation with pseudo-magnetic field

It is a standard procedure to include the effects of strain in the Dirac hamiltonian by adding a gauge field [14]. This gauge field is such that it does not break time-reversal symmetry and its curl represents the so-called pseudo-magnetic field. We can include the gauge field through a procedure similar to a Peierls substitution but with a field opposite in sign around the K and K' point. The hamiltonian is given by

$$\mathcal{H}_{\mathbf{q}}^{\mu} = v_F(\mu(q_x - \mu A_x)\sigma^x + (q_y - \mu A_y)\sigma^y). \tag{5.25}$$

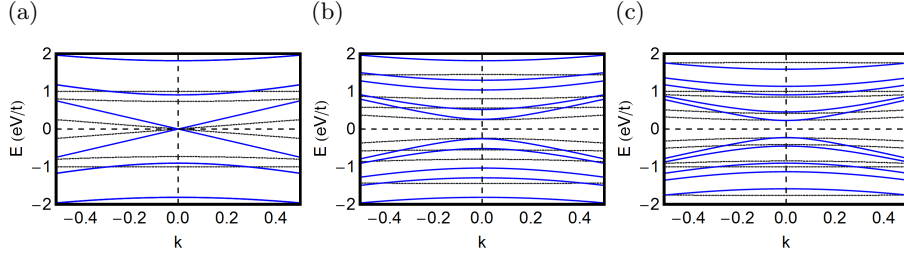


Figure 5.2: Dispersion obtained from the Dirac equation with armchair boundary condition, Eq. (5.21). Here $v_f = 3/2$. The Dirac dispersion is depicted with a thick blue line. The black line is the dispersion of a NN tight-binding model with $t = -1$. The horizontal k axes lies in the 1D BZ of the ribbon and we used that $q_y = k$ for armchair ribbons. (a) A ribbon of length $N = 5$ (b) $N = 6$ (c) $N = 7$

Here μ denotes the pseudo spin degree of freedom. The gauge field $\mathbf{A} = (A_x, A_y)$ is related to the strain through [26]

$$\mathbf{A} = \frac{\kappa}{a} \begin{pmatrix} u_{xx} - u_{yy} \\ -2u_{xy} \end{pmatrix}. \quad (5.26)$$

Here $\kappa = -\partial \ln t / \partial \ln a \approx 2.6$ is the exponential decay rate of hopping parameter, defined in Eq. (2.21). If the deformations are only in plane, as is the case for the bending deformations we consider,

$$u_{ij} = \frac{1}{2}(\partial_i u_j + \partial_j u_i), \quad u_j = F_j(\mathbf{r}) - r_j. \quad (5.27)$$

u_j is the j th component of the displacement, whose relation to the deformation function \mathbf{F} , defined earlier in section 4.9, is specified.

The derivation of Eq. (5.25) and Eq. (5.26) is rather subtle, especially for non-uniform strain. We will not reproduce it here. A detailed derivation is given in references [27] [28]. As is explained in these references Eq. (5.25) and Eq. (5.26) are only part of the effect of strain. Other important effects include a space dependent renormalisation of the Fermi velocity and terms of higher order in strain in Eq. (5.26). However we study a minimal model first given by Eq. (5.25) and Eq. (5.26).

We now calculate the gauge field for the width preserving bending that was defined in Eq. (4.2)

$$\mathbf{A}(\Theta) = \frac{2\kappa\Theta y}{aW} \begin{pmatrix} \cos(2\Theta x/W) \\ \sin(2\Theta x/W) \end{pmatrix}, \quad (5.28)$$

where Θ is the bending parameter and W the width of the ribbon, defined in section 4.9. We changed convention with respect to Eq. (4.2) such that

$r_x = x$ and $r_y = y$. We now assume that $W/2\Theta \gg x$, this seems reasonable if we consider a ribbon that has a finite length and is not too narrow and has a bending with a not too high bending parameter. Using this assumption we can do a first order approximation that reduces the gauge field to

$$\mathbf{A}(\Theta) \approx \frac{2\kappa\Theta y}{aW} \begin{pmatrix} 1 \\ 0 \end{pmatrix} = \begin{pmatrix} -\bar{B}y \\ 0 \end{pmatrix}. \quad (5.29)$$

Here $\bar{B} = \partial_x A_y - \partial_y A_x = -2\kappa\Theta/(aW)$ is the pseudo-magnetic field. So $\mathbf{A}(\Theta)$ is approximately a gauge field that corresponds to a constant pseudo-magnetic field in the Landau gauge. It is possible to solve the dirac equation within a ribbon geometry in this gauge. A constant pseudo-magnetic field has been studied in reference [29]. However they assumed a semi-infinite ribbon geometry which we will not. First we solve the dirac equation with a gauge field given by Eq. (5.29) for graphene. Then we add the boundary conditions of the ribbon.

Constant pseudo-magnetic field in graphene

In order to find the spectrum of the hamiltonian (5.25) we first square the hamiltonian,

$$\begin{aligned} (\mathcal{H}_{\mathbf{q}}^\mu)^2 &= v_F^2((q_x - \mu A_x)^2 + (q_y - \mu A_y)^2 + i\sigma^z([q_y, A_x] - [q_x, A_y])) \\ &= v_F^2((q_x - \mu A_x)^2 + (q_y - \mu A_y)^2 - \bar{B}\sigma^z). \end{aligned} \quad (5.30)$$

If we insert the gauge field of Eq. (5.29) we see that there is a translational symmetry in the x direction and we can again assume Eq. (5.10). In the real space representation Eq. (5.30) and Eq. (5.25) then reduce to

$$\begin{aligned} (\mathcal{H}_{\mathbf{q}}^\mu)^2 &= v_F^2((q_x + \mu\bar{B}y)^2 - \partial_y^2 - \bar{B}\sigma^z), \\ \mathcal{H}_{\mathbf{q}}^\mu &= v_F(\mu(q_x + \mu\bar{B}y)\sigma^x - (i\partial_y)\sigma^y). \end{aligned} \quad (5.31)$$

This is the same problem as that of a quantum harmonic oscillator. We introduce the coordinate transformation

$$\xi^\mu = \sqrt{2}(y/l_{\bar{B}} + \text{sign}(\bar{B})\mu l_{\bar{B}}q_x), \quad (5.32)$$

with the magnetic length $l_{\bar{B}} = 1/|\bar{B}|^{1/2}$. Leaving out the superscript μ of ξ , we rewrite the hamiltonian,

$$\begin{aligned} \mathcal{H}_{\mathbf{q}}^2 &= \omega_c^2 \left(\frac{\xi^2}{4} - \partial_\xi^2 - \frac{\text{sign}(\bar{B})}{2}\sigma^z \right), \\ \mathcal{H}_{\mathbf{q}} &= \omega_c \left(\text{sign}(\bar{B})\sigma^x \frac{\xi}{2} - \sigma^y i\partial_\xi \right). \end{aligned} \quad (5.33)$$

where $\omega_c = \sqrt{2}v_F/l_{\bar{B}}$ is the cyclotron frequency. If we assume a positive \bar{B} then this second-order differential equation in combination with normalizability implies that

$$E^2 = \omega_c^2 N,$$

$$\phi_{N,A} = c_1 \psi_N(\xi/\sqrt{2}), \quad \phi_{N,B} = c_2 \psi_{N-1}(\xi/\sqrt{2}),$$

for some constants c_1 and c_2 . Here, $\psi_N(x) = 2^{-N/2}(N!)^{-1/2}e^{-x^2/2}H_N(x)$ for $N \in \mathbb{N}_{>0}$ are the normalized 1D harmonic oscillator eigenstates and we also define $\psi_{-1}(x) = 0$. Next to that

$$\omega_c \left(\frac{\xi}{2} - \partial_\xi \right) \phi_{N,B} = c_2 \omega_c \left(\frac{\xi}{2} - \partial_\xi \right) \psi_{N-1}(\xi/\sqrt{2}) =$$

$$c_2 \omega_c \sqrt{N} \psi_N(\xi/\sqrt{2}) = c_2 \omega_c \sqrt{N} \phi_{N,A} / c_1 = E \phi_{N,A},$$

hence $c_2 \omega_c \sqrt{N} = c_1 E$. For ϕ' the same eigenstates are found with ξ^- instead of ξ^+ . Combining we find a doubly degenerate spectrum with spectrum with,

$$\phi_{N,\pm}(y, q_x) = \frac{1}{\sqrt{2}} \begin{pmatrix} \psi_N(\xi^+) \\ \pm \psi_{N-1}(\xi^+) \end{pmatrix},$$

$$\phi'_{N,\pm}(y, q_x) = \frac{1}{\sqrt{2}} \begin{pmatrix} \psi_N(\xi^-) \\ \pm \psi_{N-1}(\xi^-) \end{pmatrix},$$
(5.34)

whose energies are the pseudo-landau levels given by

$$E_{\pm}^{\mu}(N) = \pm \omega_c \sqrt{N}. \quad (5.35)$$

Note that these two degenerate eigenstates do not mix for graphene, they are separate solutions. We can see from Eq. 5.33 that a negative \bar{B} -field is equivalent to a sublattice interchange combined with a space inversion $y \rightarrow -y$. Thus for negative \bar{B} we find the same dispersion as Eq. (5.35). But the corresponding eigenstates have their sublattices interchanged and y is changed to $-y$ with respect to the states of Eq. (5.34).

It is interesting to remark that the lowest pseudo-landau level is localised on the same sublattice for both the K and K' valley. This is in contrast to the lowest landau level for a real magnetic field [30]. Eventhough this analysis concerned graphene it does give us the prediction that at least for wide ribbons we should see these pseudo-landau level emerging in the bandstructure of bent GNRs.

Zigzag ribbon in a constant pseudo-magnetic field

We can also solve the Dirac equation with magnetic field in a zigzag ribbon geometry using the boundary conditions of Eq. (5.12). If we choose a positive

\bar{B} the equation for the K valley, ϕ , becomes

$$\begin{aligned} \left(\partial_\xi^2 - \frac{\xi^2}{4} + \frac{1}{2}\sigma^z + \tilde{\epsilon}^2 \right) \phi &= 0 \\ \left(-i\partial_\xi \sigma^y + \frac{\xi}{2}\sigma^x \right) \phi &= \tilde{\epsilon}\phi, \end{aligned} \quad (5.36)$$

where $\tilde{\epsilon} = E/\omega_c$. Now we cannot easily conclude that the eigenstates should be 1D harmonic oscillator states because in a finite geometry these are not the only normalizable states. The second-order equation in Eq. (5.36) is called Webers equation and its general solution can be given in terms of parabolic cylindrical functions [31]:

$$\begin{aligned} \phi_A(\xi) &= AU\left(-\frac{1}{2} - \tilde{\epsilon}^2, \xi\right) + \bar{B}V\left(-\frac{1}{2} - \tilde{\epsilon}^2, \xi\right) \\ \phi_B(\xi) &= CU\left(\frac{1}{2} - \tilde{\epsilon}^2, \xi\right) + DV\left(\frac{1}{2} - \tilde{\epsilon}^2, \xi\right) \end{aligned} \quad (5.37)$$

Here U is a function that is asymptotic to $e^{-\frac{\xi^2}{4}}$ as $\xi \rightarrow \infty$ and V to $e^{\frac{\xi^2}{4}}$. By using the first-order differential relation between sublattice state and the properties of U and V it follows that,

$$\begin{aligned} [-\partial_\xi + \frac{\xi}{2}]\phi_B(\xi) &= CU\left(-\frac{1}{2} - \tilde{\epsilon}^2, \xi\right) + D\tilde{\epsilon}^2V\left(-\frac{1}{2} - \tilde{\epsilon}^2, \xi\right) = \tilde{\epsilon}\phi_A. \\ [\partial_\xi + \frac{\xi}{2}]\phi_A(\xi) &= A\tilde{\epsilon}^2U\left(\frac{1}{2} - \tilde{\epsilon}^2, \xi\right) + \bar{B}V\left(\frac{1}{2} - \tilde{\epsilon}^2, \xi\right) = \tilde{\epsilon}\phi_B. \end{aligned} \quad (5.38)$$

Therefore $C = \tilde{\epsilon}A$, $\tilde{\epsilon}^2D = \tilde{\epsilon}B$ and $B = \tilde{\epsilon}D$, $A\tilde{\epsilon}^2 = \tilde{\epsilon}C$. We eliminate C and B in terms of A and D . Now we need to solve for the zigzag boundary conditions. Around the K point $\xi = \sqrt{2}(\frac{y}{l_B} + l_B q_x)$, as in Eq. 5.32. Therefore the boundary conditions translate in the equations

$$\begin{aligned} AU\left(-\frac{1}{2} - \tilde{\epsilon}^2, k' + L'\right) + \tilde{\epsilon}DV\left(-\frac{1}{2} - \tilde{\epsilon}^2, k' + L'\right) &= 0 \\ \tilde{\epsilon}AU\left(\frac{1}{2} - \tilde{\epsilon}^2, k'\right) + DV\left(\frac{1}{2} - \tilde{\epsilon}^2, k'\right) &= 0, \end{aligned} \quad (5.39)$$

where $k' = \sqrt{2}l_B q_x$ and $L' = \sqrt{2}L/l_B$. Non-trivial solutions of these equations are at the zero points of the function

$$\begin{aligned} F_K(k', \tilde{\epsilon}, L') &= U\left(-\frac{1}{2} - \tilde{\epsilon}^2, k' + L'\right)V\left(\frac{1}{2} - \tilde{\epsilon}^2, k'\right) - \\ &\quad \tilde{\epsilon}^2V\left(-\frac{1}{2} - \tilde{\epsilon}^2, k' + L'\right)U\left(\frac{1}{2} - \tilde{\epsilon}^2, k'\right) \end{aligned} \quad (5.40)$$

Solution to this transcendental equation determine the spectrum $E^+(q_x)$. From this spectrum we also derive the spectrum around the K' point. The only difference with respect to the spectrum around the K point lies in the definition

of ξ^- with respect to ξ^+ . We see there that if we change $q_x \rightarrow -q_x$ in the spectrum around the K point we should get the spectrum around the K' point, $E^-(q_x) = E^+(-q_x)$.

Also the solutions for $\bar{B} < 0$ can be derived from these. If we change $y \rightarrow L - y$ and $q_x \rightarrow q_x - \mu L|\bar{B}|$ and interchange the sublattices we get the exact same equations and boundary conditions as for the positive \bar{B} case. Therefore $E_{\bar{B}<0}^\mu(q_x) = E^\mu(q_x + \mu L|\bar{B}|)$.

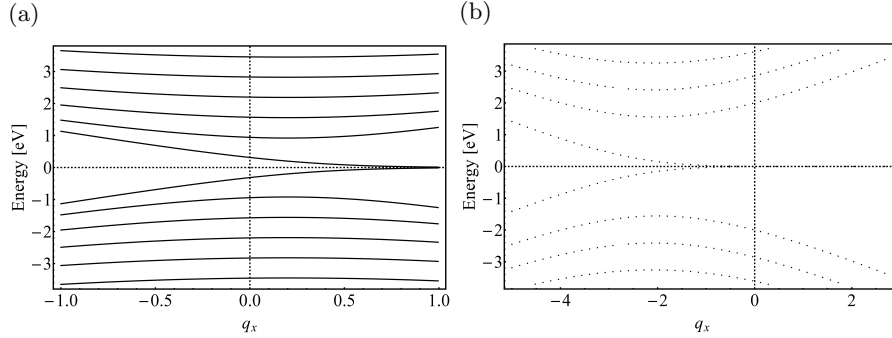


Figure 5.3: (a) Spectrum of ZGNR of $L = 5$ around K point using Dirac equation and zigzag boundary conditions with $v_F = 1$. (b) Spectrum including a pseudo magnetic field $\bar{B} = 1$, obtained from solving Eq. 5.53

We would like to see if the spectrum obtained by inclusion of a pseudo magnetic field reproduces the effects observed from our tight-binding calculations, i.e. the splitting of the edge state and the emerging band structure. To study this we need to know how the spectrum scales with varying \bar{B} field, however there is no simple relation between this. If we multiply \bar{B} by a factor such that $\bar{B} \rightarrow \alpha\bar{B}$, then we have to solve 5.53 only with $\tilde{\epsilon} \rightarrow \tilde{\epsilon}/\sqrt{\alpha}$, $k' \rightarrow k'/\sqrt{\alpha}$ and $L' \rightarrow \sqrt{\alpha}L'$. The changes in $\tilde{\epsilon}$ and k' could be easily taken care of by rescaling the E and q_x axes accordingly in the dispersion, but because L' also changes this is not the complete solution. A simultaneous change of \bar{B} with a factor α and a change in L with a factor $1/\alpha$ would leave the dispersion as it is with only a rescaling of the axes by α . This is to be expected as a narrower ribbon should separate the levels more.

Therefore we have to solve Eq. 5.53 explicitly for different values of \bar{B} . Results are depicted in Fig. 5.3 for $\bar{B} = 0$ and $\bar{B} = 1$. We have not attempted here to relate this value of \bar{B} to our bending parameter Θ . This we have not done because it is already visible from this case that we do not reproduce the splitting and therefore also not the emergent band structure. The thing we observe in Fig. 5.3 is that the spectrum for non-zero \bar{B} experiences a shift of the edge states to the left and an increase in the distance between the bands. One can also see a flattening developing around the valley of the bands. This becomes flatter for largen \bar{B} (not depicted here). We can interpret these

flattening bands as emerging Landau levels. A more detailed quantitative comparison between the tight-binding spectrum and the dirac spectrum could reveal that these two effects are also visible in tight-binding. However we currently wanted to check if the emergent band-structure could be explained from the pseudo-magnetic field but this seems not to be the case.

The reason for this discrepancy is most likely because the Dirac equation is derived from a NN tight-binding theory. However in our explanation of the emergent band structure for the edge states we emphasized the importance of the NNN hopping. It should be investigated whether inclusion of the NNN hopping can be included in the continuum model combined with strain.

Armchair ribbon in a pseudo-magnetic field

If one want to use Eq. (5.25) for an AGNR one has to position the ribbon with its long side along the y -axis. The width preserving bending is then identical to Eq. 5.28 but with the $x \rightarrow -y$ and $y \rightarrow x$. In this case the pseudo gauge field becomes $\mathbf{A} = (0, \bar{B}x)$. Replacing $q_y \rightarrow q_y$ and $q_x \rightarrow -i\partial_x$ this gives

$$\begin{aligned}\mathcal{H}_{\mathbf{q}}^2 &= v_F^2((q_y - \bar{B}x)^2 - \partial_x^2 - \bar{B}\tau^z \otimes \sigma^z), \\ \mathcal{H}_{\mathbf{q}} &= v_F(-\tau^z \otimes (i\partial_x)\sigma^x + id \otimes (q_y - \bar{B}x)\sigma^y).\end{aligned}\quad (5.41)$$

If we now make the coordinate transformation $\xi = \sqrt{2}(\text{sign}(\bar{B})\frac{x}{l_B} - l_B q_y)$ we get:

$$\begin{aligned}\mathcal{H}_{\mathbf{q}}^2 &= \omega_c\left(\frac{\xi}{4} - \partial_\xi^2 - \frac{\text{sign}(\bar{B})}{2}\tau^z \otimes \sigma^z\right), \\ \mathcal{H}_{\mathbf{q}} &= \omega_c(-id \otimes \frac{\xi}{2}\sigma^y - \text{sign}(\bar{B})\tau^z \otimes (i\partial_\xi)\sigma^x).\end{aligned}\quad (5.42)$$

Notice that the squared Hamiltonian is identical to the zigzag one, Eq. (5.42). Let us now consider $\bar{B} > 0$. Then we get for ϕ and ϕ'

$$\begin{aligned}\left(\partial_\xi^2 - \frac{\xi^2}{4} + \frac{1}{2}\sigma^z + \tilde{\epsilon}^2\right)\phi &= 0 & \left(\partial_\xi^2 - \frac{\xi^2}{4} - \frac{1}{2}\sigma^z + \tilde{\epsilon}^2\right)\phi' &= 0 \\ \left(-\frac{\xi}{2}\sigma^y - i\partial_\xi\sigma^x\right)\phi &= \tilde{\epsilon}\phi & \left(-\frac{\xi}{2}\sigma^y + i\partial_\xi\sigma^x\right)\phi' &= \tilde{\epsilon}\phi',\end{aligned}\quad (5.43)$$

hence again, for ϕ Eq. (5.37) holds but now Eq. (5.38) changes to

$$\begin{aligned}i[-\partial_\xi + \frac{\xi}{2}]\phi_B(\xi) &= iCU\left(-\frac{1}{2} - \tilde{\epsilon}^2, \xi\right) + iD\tilde{\epsilon}^2V\left(-\frac{1}{2} - \tilde{\epsilon}^2, \xi\right) = \\ & \tilde{\epsilon}\phi_A. \\ -i[\partial_\xi + \frac{\xi}{2}]\phi_A(\xi) &= -iA\tilde{\epsilon}^2U\left(\frac{1}{2} - \tilde{\epsilon}^2, \xi\right) - i\bar{B}V\left(\frac{1}{2} - \tilde{\epsilon}^2, \xi\right) = \\ & \tilde{\epsilon}\phi_B.\end{aligned}\quad (5.44)$$

Therefore $iC = \tilde{\epsilon}A$, $i\tilde{\epsilon}^2D = \tilde{\epsilon}B$ and $-iB = \tilde{\epsilon}D$, $-iA\tilde{\epsilon}^2 = \tilde{\epsilon}C$. Therefore, we can write

$$\begin{aligned}\phi_A(\xi) &= AU(-\frac{1}{2} - \tilde{\epsilon}^2, \xi) + i\tilde{\epsilon}DV(-\frac{1}{2} - \tilde{\epsilon}^2, \xi) \\ \phi_B(\xi) &= -i\tilde{\epsilon}AU(\frac{1}{2} - \tilde{\epsilon}^2, \xi) + DV(\frac{1}{2} - \tilde{\epsilon}^2, \xi)\end{aligned}\quad (5.45)$$

Around K' we find again the roles of the sublattices interchanged in the squared Hamiltonian, say

$$\begin{aligned}\phi'_A(\xi) &= C'U(\frac{1}{2} - \tilde{\epsilon}^2, \xi) + D'V(\frac{1}{2} - \tilde{\epsilon}^2, \xi) \\ \phi'_B(\xi) &= A'U(-\frac{1}{2} - \tilde{\epsilon}^2, \xi) + B'V(-\frac{1}{2} - \tilde{\epsilon}^2, \xi)\end{aligned}\quad (5.46)$$

and

$$\begin{aligned}i[\partial_\xi + \frac{\xi}{2}]\phi'_B(\xi) &= i\tilde{\epsilon}^2A'U(\frac{1}{2} - \tilde{\epsilon}^2, \xi) + iB'V(\frac{1}{2} - \tilde{\epsilon}^2, \xi) = \\ & \tilde{\epsilon}\phi'_A. \\ -i[-\partial_\xi + \frac{\xi}{2}]\phi'_A(\xi) &= -iC'U(-\frac{1}{2} - \tilde{\epsilon}^2, \xi) - i\tilde{\epsilon}^2D'V(\frac{1}{2} - \tilde{\epsilon}^2, \xi) = \\ & \tilde{\epsilon}\phi'_B.\end{aligned}\quad (5.47)$$

Therefore $i\tilde{\epsilon}^2A' = \tilde{\epsilon}C'$, $iB' = \tilde{\epsilon}D'$ and $-iC' = \tilde{\epsilon}A'$, $-i\tilde{\epsilon}^2D' = \tilde{\epsilon}B'$. So we can write

$$\begin{aligned}\phi'_A(\xi) &= i\tilde{\epsilon}A'U(\frac{1}{2} - \tilde{\epsilon}^2, \xi) + D'V(\frac{1}{2} - \tilde{\epsilon}^2, \xi) \\ \phi'_B(\xi) &= A'U(-\frac{1}{2} - \tilde{\epsilon}^2, \xi) - i\tilde{\epsilon}D'V(-\frac{1}{2} - \tilde{\epsilon}^2, \xi)\end{aligned}\quad (5.48)$$

Now we want to impose the armchair boundary conditions, given by Eq. (5.21). These boundary condition translate into the four equations

$$\begin{aligned}AU_{\xi_0}^a + i\tilde{\epsilon}DV_{\xi_0}^a + i\tilde{\epsilon}A'U_{\xi_0}^{a+1} + D'V_{\xi_0}^{a+1} &= 0 \\ -i\tilde{\epsilon}AU_{\xi_0}^{a+1} + DV_{\xi_0}^{a+1} + A'U_{\xi_0}^a - i\tilde{\epsilon}D'V_{\xi_0}^a &= 0 \\ e^{iKL}(AU_{\xi_L}^a + i\tilde{\epsilon}DV_{\xi_L}^a) + e^{-iKL}(i\tilde{\epsilon}A'U_{\xi_L}^{a+1} + D'V_{\xi_L}^{a+1}) &= 0 \\ e^{iKL}(-i\tilde{\epsilon}AU_{\xi_L}^{a+1} + DV_{\xi_L}^{a+1}) + e^{-iKL}(A'U_{\xi_L}^a - i\tilde{\epsilon}D'V_{\xi_L}^a) &= 0,\end{aligned}\quad (5.49)$$

where for convenience we denoted $V_\xi^a = V(-\frac{1}{2} - \tilde{\epsilon}^2, \xi)$ and $\xi_0 = \xi(x=0)$, $\xi_L = \xi(x=L)$. We can rewrite the boundary conditions to eliminate two of the constants, namely D' and D . We find

$$\begin{aligned}D(\tilde{\epsilon}^2(V_{\xi_0}^a)^2 - (V_{\xi_0}^{a+1})^2) &= A'(U_{\xi_0}^a V_{\xi_0}^{a+1} - \tilde{\epsilon}^2 U_{\xi_0}^{a+1} V_{\xi_0}^a) + i\tilde{\epsilon}A(U_{\xi_0}^a V_{\xi_0}^a - U_{\xi_0}^{a+1} V_{\xi_0}^{a+1}) \\ D'(\tilde{\epsilon}^2(V_{\xi_0}^a)^2 - (V_{\xi_0}^{a+1})^2) &= A(U_{\xi_0}^a V_{\xi_0}^{a+1} - \tilde{\epsilon}^2 U_{\xi_0}^{a+1} V_{\xi_0}^a) - i\tilde{\epsilon}A'(U_{\xi_0}^a V_{\xi_0}^a - U_{\xi_0}^{a+1} V_{\xi_0}^{a+1}) \\ D(\tilde{\epsilon}^2(V_{\xi_L}^a)^2 - (V_{\xi_L}^{a+1})^2) &= e^{-2iKL}A'(U_{\xi_L}^a V_{\xi_L}^{a+1} - \tilde{\epsilon}^2 U_{\xi_L}^{a+1} V_{\xi_L}^a) + i\tilde{\epsilon}A(U_{\xi_L}^a V_{\xi_L}^a - U_{\xi_L}^{a+1} V_{\xi_L}^{a+1}) \\ D'(\tilde{\epsilon}^2(V_{\xi_L}^a)^2 - (V_{\xi_L}^{a+1})^2) &= e^{2iKL}A(U_{\xi_L}^a V_{\xi_L}^{a+1} - \tilde{\epsilon}^2 U_{\xi_L}^{a+1} V_{\xi_L}^a) - i\tilde{\epsilon}A'(U_{\xi_L}^a V_{\xi_L}^a - U_{\xi_L}^{a+1} V_{\xi_L}^{a+1})\end{aligned}\quad (5.50)$$

As the D 's should be equal this leads to two equations in A and A' , for convenience cal $f_\xi^a = U_\xi^a V_\xi^{a+1} - \tilde{\epsilon}^2 U_\xi^{a+1} V_\xi^a$ and $g_\xi^a = U_\xi^a V_\xi^a - U_\xi^{a+1} V_\xi^{a+1}$, then

$$\begin{aligned} A'(f_{\xi_0}^a - e^{-2iKL} f_{\xi_L}^a) + i\tilde{\epsilon}A(g_{\xi_0}^a - g_{\xi_L}^a) &= 0 \\ -i\tilde{\epsilon}A'(g_{\xi_0}^a - g_{\xi_L}^a) + A(f_{\xi_0}^a - e^{2iKL} f_{\xi_L}^a) &= 0 \end{aligned} \quad (5.51)$$

To find non-trivial solutions of this we have to find zeros of the function

$$F(q', \tilde{\epsilon}) = -\tilde{\epsilon}^2 (g_{\xi_0}^a - g_{\xi_L}^a)^2 + (f_{\xi_0}^a)^2 + (f_{\xi_L}^a)^2 - 2f_{\xi_0}^a f_{\xi_L}^a \cos(2KL) \quad (5.52)$$

This is function of order 4 in terms of the parabolic cylindrical functions U, V . If we define $u_\xi^a = (U_\xi^a)^2 - \tilde{\epsilon}^2 (U_\xi^{a+1})^2$ and $v_\xi^a = (V_\xi^{a+1})^2 - \tilde{\epsilon}^2 (V_\xi^a)^2$, then we can rewrite

$$F(q', \tilde{\epsilon}) = u_{\xi_0}^a v_{\xi_0}^a + u_{\xi_L}^a v_{\xi_L}^a + \tilde{\epsilon}^2 g_{\xi_0}^a g_{\xi_L}^a - 2f_{\xi_0}^a f_{\xi_L}^a \cos(2KL) \quad (5.53)$$

For positive \bar{B} -field $\xi_0 = -\sqrt{2}(l_{\bar{B}} q_y) = -q'$ and $\xi_L = \sqrt{2}(\frac{L}{l_{\bar{B}}} - l_{\bar{B}} q_y) = L' - q'$. Again we can look for the roots of this function numerically, see Fig. (5.3).

We would now like to compare the dispersion one would obtain from Eq. 5.53 with the results obtained from our tight-binding theory. Especially we would like to look at the $q = 0$ point and study the bandgap. However in their current form these transcendental equations seemed to be too difficult to solve using our numerical software. We do expect the results for the bandgap to maybe be in better comparison with the results from tight-binding as in contrast to edge states of the ZGNRs the bandgap of AGNRs is not as crucially dependent on NNN hopping.

Chapter 6

Conclusions and outlook

6.1 Conclusions

In this thesis we studied the electronic band structure of an in-plane bent GNR. This we mainly did using a tight-binding model. We made first steps in studying this system using the Dirac equation. Specifically we studied the dependence on the bending of the bandgap for AGNRs and of the edge states for ZGNRs. We used two different bending geometries: width-preserving and bond-length-preserving bending.

We conclude that a tight-binding model that assumes non-zero hopping and overlap which decay exponentially is a minimal tight-binding model with three parameters that can be used to study a system that is both geometrically confined and strained. Using the fact that our two bending geometries have a rotational symmetry we can reduce this tight-binding model to the numerically inexpensive problem of solving a matrix equation with $2N \times 2N$ matrices (with $2N$ the number of sites in the unit cell of the GNR). From this model we observe two general effects for both AGNRs and ZGNRs

- Bands move up or down with respect to the straight dispersion. If the deviations are comparable after both bending methods one can attempt to predict whether the state is localised more on the inside or the outside of the bent ribbon. This is done by comparing the deviation to the deviation of the band due to uniform longitudinal strain.
- Some degeneracies in the band structure split because of the breaking of the symmetry between the top and bottom edge of the ribbon.

We conclude that the effects of bending on the bandgap of AGNRs as calculated by our tight-binding model are not very big because the states determining the bandgap are bulk states. Details of the exact geometry used for bending become important. In the two bending geometries we consider the following effects are observed:

- The bandgap for width preserving and bondlength-preserving bending increases with bending for type I, increases and then decreases for type II, and decreases for III AGNRs.
- This behaviour is reminiscent of uniform negative strain (compression) in the longitudinal direction or uniform positive strain (stretching) in the transverse direction.

We conclude that there are interesting effects of bending on the edge states of ZGNRs as calculated by our tight-binding model. This is because edge states are sensitive to the symmetry breaking between the top and bottom edge. We observe the following effects. Both width preserving and bondlength-preserving bending predict a splitting of the two edge states (without considering interactions). A lower energy edge state localises on the outer edge and a higher energy edge state on the inner edge. In fact, there is an emergent band structure of the edge states that can be fitted to the tight-binding dispersion of a 1D chain with an effective hopping and on-site energy parameter. The dependence of these parameters on the degree of bending depends on the method of bending though both do predict that the higher energy edge state localised on the inner edge will have a hopping that gradually changes sign. Because of this there is a degree of bending where the band is effectively flat and interesting interaction effect are expected. The difference between the bending methods is due to extra hybridisation effects that occur for the width preserving bending, which cause a more complicated and width dependent relation between bending angle and effective parameter. We can understand the effects of bending on the emergent band structure that are due to the NNN hopping as a competition between the decreasing localisation for k -values differing from π and the localised character of the edge state.

In chapter 5 we studied bent GNR by including a pseudo magnetic field in the Dirac hamiltonian and used the boundary conditions for AGNRs and ZGNRs. We approximated the gauge field by one that produces a constant pseudo-magnetic field. In conclusion we can say that:

- Simply combining the boundary conditions of AGNRs and ZGNRs with a constant pseudo magnetic field allows one to solve the Dirac equation exactly using parabolic harmonic functions.
- For ZGNRs: The dispersion starts to develop pseudo-Landau levels and shifts the starting point of edge states or ZGNRs. However no splitting of the edge state is observed nor an emerging band structure.
- For AGNRs: The equations are currently too difficult to solve using simple algorithms.

One possible explanation for the difference between the tight-binding model and the continuum model can be the importance of the NNN hopping in the

tight-binding model. A second reason can be that the assumption of a constant pseudo-magnetic field is not valid. Another can be the incomplete inclusion of strain effects when only considering the gauge field, a more full treatment would for instance also include a recanalization of the Fermi velocity. Finally the boundary conditions could change when one considers a bent geometry.

6.2 Outlook

Emergent band structure of edge states

Probably the most interesting result of this thesis is the emergent band structure that is observable for the edge states of a ZGNR.

For future research into this area it would first of all be beneficial to understand more clearly the exact relation between the bending parameter and the effective parameters. We have explained it qualitatively in this thesis as a competition between two effects resulting in a positive and negative hopping. We have not discussed how to understand the effective on-site energy that was observed to develop in a similar fashion with respect to bending as the effective hopping. One way to predict the effective parameters would be to develop a perturbation theory on the exact solution of a straight ribbon with NN hopping. From this one could more clearly understand what effects of the change in NN hopping due to bending and the effects of the change in NNN hopping due to bending.

A next step would be to include interaction effects as these are important for edge states. One could try to answer the question how bending combines with the known effect of magnetic polarisation of the edge states [4].

Continuum model

We have seen that we can solve the Dirac equation for massless fermions with a constant pseudo-magnetic field and AGNR and ZGNR boundary conditions. However it is currently unclear how these relate to the physically more transparent tight-binding results.

One could first try to solve the Dirac equation (numerically) without making the assumption of a constant pseudo magnetic field. Next different boundary conditions could be tried.

To include effects of NNN neighbor in the Dirac hamiltonian extra terms could be added, see section 2.2 of Ref. [32]. However one would also need to think how to combine this NNN neighbor term with strain.

Finite-size effects and geometry

We show in the appendix B that for straight ribbons at least the DOS of finite ribbons approach that of period ribbons. However we haven't discussed

in this thesis the relation between finite sized bent ribbons and period bent ribbons. It would be interesting to investigate if we still can see remains of the emergent band structure. Next to that, using molecular dynamics we could try to answer to what extend a lattice preserving bending is accurate.

Another future research area could be the study of different but related geometries. We can use almost the exact same tight-binding model, with the same computational effort, to study the p_z electrons of other lattice preserving deformation (appendix C). For instance, we could study a helically twisted GNR. This has been studied but without an emphasize on the edge states within ZGNRs in Ref. [33], also descriptions of this system using Dirac theory have been made [34].

Acknowledgement

In the first place I would like to thank my supervisor Cristiane for a very pleasant supervision. I really appreciate the way you care about your students and am inspired by all the different collaborations and projects you participate in. Even though at times it was hard for me to progress at the end I can look back on a great learning experience and my first taste of real science. I also would like to thank my co-supervisor Vladimir. You always had time to discuss the technical side of my thesis and have guided me to the interesting parts of my results, which I'm very thankful for. Next to that I would very much like to thank the other members of the group, Carmine, Emilio, Marco, Leandro, Natalia, Anton, Guido and Floor. There are many different projects in the group, it was great to see the exchange of ideas between members. Next to that I'm very thankful for the collaboration with the experimentalists, Daniël, Ingmar, and Peter. The closeness of my project to experiments was one of the things I most enjoyed. Peter, I learned very much from our close collaboration and am always impressed by the scope of your knowledge, from chemistry to theory. Not least, I would like to thank the many other students of the theoretical physics master for discussions and especially coffee.

Appendix A

Relation between orbital- and orthogonal-hopping parameters in graphene

By comparing Eq. (2.6) and Eq. (2.18), we can see how the tight-binding model assuming orthogonal basis states and the tight-binding model assuming non-orthogonal basis states are related in graphene. Namely, both secular equations give the same spectrum if we require that

$$\mathcal{S}_{\mathbf{k}}^{-1/2} \mathcal{H}_{\mathbf{k}} \mathcal{S}_{\mathbf{k}}^{-1/2} = H_{\mathbf{k}}, \quad (\text{A.1})$$

where $H_{\mathbf{k}}$ is the second-quantized Hamiltonian matrix. This identity is permitted because $\mathcal{S}_{\mathbf{k}}^{-1/2} \mathcal{H}_{\mathbf{k}} \mathcal{S}_{\mathbf{k}}^{-1/2}$ is automatically hermitian. The eigenstates \bar{C} of $\mathcal{S}_{\mathbf{k}}^{-1/2} \mathcal{H}_{\mathbf{k}} \mathcal{S}_{\mathbf{k}}^{-1/2}$, and thus of $H_{\mathbf{k}}$ if Eq. (A.1) is satisfied, are related to the states C that solve Eq. (2.11) by $\bar{C} = \mathcal{S}_{\mathbf{k}}^{1/2} C$. Thus if the second- and first-quantized matrices satisfy Eq. (A.1) they describe the same system and we have shown how they are related.

In graphene $\mathcal{S}_{\mathbf{k}}^{-1}$ commutes with $\mathcal{H}_{\mathbf{k}}$. This is because $s_{\mathbf{k}}^{AB} t_{\mathbf{k}}^{AB*} = s_{\mathbf{k}}^{AB*} t_{\mathbf{k}}^{AB}$ and because the diagonal elements of $\mathcal{S}_{\mathbf{k}}$ and $\mathcal{H}_{\mathbf{k}}$ are all identical, computing $\mathcal{S}_{\mathbf{k}}^{-1}$ one can see that it therefore should commute with $\mathcal{H}_{\mathbf{k}}$. It is a theorem from linear algebra that because $\mathcal{S}_{\mathbf{k}}^{-1}$ is a positive semidefinite matrix also $\mathcal{S}_{\mathbf{k}}^{-1/2}$ commutes with $\mathcal{H}_{\mathbf{k}}$. Therefore $\mathcal{S}_{\mathbf{k}}^{-1/2} \mathcal{H}_{\mathbf{k}} \mathcal{S}_{\mathbf{k}}^{-1/2} = \mathcal{S}_{\mathbf{k}}^{-1} \mathcal{H}_{\mathbf{k}} = H_{\mathbf{k}}$. As $\mathcal{S}_{\mathbf{k}}$ is a 2×2 matrix we can easily compute its inverse. Using definitions from Eqs. (2.13) and (2.14) we find that

$$\epsilon_0 \mathbf{I} + \frac{1}{s_{\mathbf{k}}^{AA^2} - s_{\mathbf{k}}^{AB*} s_{\mathbf{k}}^{AB}} \begin{pmatrix} s_{\mathbf{k}}^{AA} & -s_{\mathbf{k}}^{AB} \\ -s_{\mathbf{k}}^{AB*} & s_{\mathbf{k}}^{AA} \end{pmatrix} \begin{pmatrix} t_{\mathbf{k}}^{AA} & t_{\mathbf{k}}^{AB} \\ t_{\mathbf{k}}^{AB*} & t_{\mathbf{k}}^{AA} \end{pmatrix} = \begin{pmatrix} H_{\mathbf{k}}^{AA} & H_{\mathbf{k}}^{AB} \\ H_{\mathbf{k}}^{AB*} & H_{\mathbf{k}}^{AA} \end{pmatrix} \quad (\text{A.2})$$

So we see that the two type of parameters are related by,

$$H_{\mathbf{k}}^{AA} = \frac{s_{\mathbf{k}}^{AA}t_{\mathbf{k}}^{AA} - s_{\mathbf{k}}^{AB}t_{\mathbf{k}}^{AB*}}{s_{\mathbf{k}}^{AA^2} - s_{\mathbf{k}}^{AB*}s_{\mathbf{k}}^{AB}} + \epsilon_0, \quad H_{\mathbf{k}}^{AB} = \frac{s_{\mathbf{k}}^{AA}t_{\mathbf{k}}^{AB} - s_{\mathbf{k}}^{AB}t_{\mathbf{k}}^{AA}}{s_{\mathbf{k}}^{AA^2} - s_{\mathbf{k}}^{AB*}s_{\mathbf{k}}^{AB}}. \quad (\text{A.3})$$

This relation is still expressed in \mathbf{k} space, to find the actual n-neighbor hopping on the left from this k dependent function we need to calculate its fourier transform. The n-th neighbor inter-sublattice hopping term is given by

$$t_n = \int H_{\mathbf{k}}^{AB} e^{-i\mathbf{k}\cdot R_i} d\mathbf{k} \quad (\text{A.4})$$

such that $|R_i|$ is the n-th neighbor distance.

We would like to give a motivation for the assumption of exponentially decaying first-quantized hopping and overlap parameters, given by Eq. 2.21. One strategy is to calculate the second-quantized hopping parameters and compare these to the ab-initio calculations of [16]. There the first five hopping parameters are calculated to be -3.00236 , 0.20509 , -0.22464 , 0.05205 , 0.06912 . The values for the first-quantized parameters that we use are $t_0 = -2.5$ eV, $s_0 = 0.36$, $\kappa = 1.5$. If we calculate the first five second-quantized hopping parameters that belong to those we get the list -3.09216 , 0.228831 , -0.222085 , 0.0484246 , 0.0343871 . We can see that the general features of the first list are reproduced. Namely, the same pattern of negative and positive signs are observed and a similar decrease in amplitude. These are however not the same parameters that we used for our analysis as we have decided to remain closer to the reference non-orthogonal parameters of [20]. It does however show that an exponential decay is not an unreasonable assumption.

Appendix B

Comparing the spectra of graphene, periodic ribbons and finite ribbons

Our model to treat GNRs and bent GNRs assumed periodic boundary conditions in order to treat them as a 1D crystal. This enabled us to reduce the tight-binding problem from solving a matrix equation with $\bar{N} \times \bar{N}$ matrices, where \bar{N} is the total number of sites of the ribbon, to a matrix equation involving $2N \times 2N$ matrices, where $2N$ is the number of atoms in the 1D unit cell of the ribbon. In this appendix we give an extra justification of this assumption by showing that for long ribbons the density of states of finite ribbons approaches that of ribbons with periodic boundary conditions.

Tight-binding model for finite graphene nanoribbons

Actual experimental samples are of course never completely periodic, therefore it is useful to also investigate the electronic properties of finite GNRs. We start again by assuming the general first-quantized tight-binding wavefunction. In contrast to our starting wavefunction, given by Eq. (2.9), we do not explicitly make a distinction between the two sublattices. Our starting tight-binding wavefunction is therefore given by

$$\psi(\mathbf{r}) = \sum_i c_i \phi(\mathbf{r} - \mathbf{r}_i). \quad (\text{B.1})$$

Here, i runs over the atoms in the GNR, the positions of the ions are given by \mathbf{r}_i , and c_i are the coefficients of the orbitals.

We cannot use Bloch's theorem to simplify this wave function as there is no translation symmetry for a finite ribbon. We can understand the finite GNR

also as a zero dimensional (0D) system with a unit cell which contains all the points of the finite GNR. As we did for graphene and for GNR with a periodic boundary condition, we now look for solutions of the time-independent Schrödinger equation by multiplying it by $\psi^*(\mathbf{r})$ and integrating over space. We then obtain

$$\int d\mathbf{r}\psi^*(\mathbf{r})\mathcal{H}\psi(\mathbf{r}) = E \int d\mathbf{r}\psi^*(\mathbf{r})\psi(\mathbf{r}),$$

with \mathcal{H} the Hamiltonian given by Eq. (2.8). Using the tight-binding assumption, we can rewrite this as

$$c^\dagger H c = E c^\dagger S c, \quad (\text{B.2})$$

where c is the vector with orbital components and E is the eigenenergy. H and S are both $N \times N$ size matrices, where N is the number of atoms in the ribbon. They are given by

$$H^{ij} = \epsilon_0 S^{ij} + T^{ij}, \quad (\text{B.3})$$

with $j, i \in \{1, \dots, N\}$ and

$$\begin{aligned} S^{ij} &= s(\mathbf{r}_j - \mathbf{r}_i), \\ T^{ij} &= t(\mathbf{r}_j - \mathbf{r}_i). \end{aligned} \quad (\text{B.4})$$

Here, $t(\mathbf{R})$ and $s(\mathbf{R})$ are defined as earlier in Eq. (2.14). From Eq. (B.3) we get the secular equation

$$\det[T - (E - \epsilon_0)S] = 0. \quad (\text{B.5})$$

Since these matrices are always large, it is not obvious how to solve Eq. (B.5) analytically. Using numerical methods, however, we can solve the matrix Eq. (B.2) directly. This is equivalent to finding the spectrum of $S^{-1}\mathcal{H}$. Because there is no translation symmetry, there is no exact reciprocal space and no dispersion relation. However, we can use the density of states (DOS) to compare the spectrum with periodic systems.

Comparison using the density of states

The three cases studied so far, namely graphene, GNRs with periodic boundary condition and finite GNRs, all yield a secular equation, Eqs. (2.12), (3.9) and (B.5), respectively. These secular equations determine the eigenenergies of the spectrum and from them the corresponding eigenstates can be determined. The equations were solved either analytically (graphene) or numerically (GNRs with periodic boundary condition and finite GNRs). Now, we would like to compare these different systems. We expect that for large systems the two GNR solutions become equivalent to the graphene solution. One

way to compare the different systems is by calculating their density of states (DOS).

If we want to compare the DOS for the three different systems, we have to be cautious, because the systems have different dimensions: graphene is 2D, the GNRs with a periodic boundary condition are 1D, and the finite GNRs are 0D. The DOS depends strongly on this. We will define an approximation of the DOS that takes this dimensionality into account and allows us to compare systems of different dimensionality. One can define the DOS as follows:

$$\mathcal{D}(E) = \sum_{\lambda} \frac{1}{N_{bands}\Omega_{BZ}} \int_{BZ} \delta(E - E_{\mathbf{k}}^{\lambda}) d\mathbf{k}. \quad (\text{B.6})$$

Here, λ denotes a sum over the bands and Ω_{BZ} denotes the volume of the Brillouin zone, with N_{bands} the number of bands (which is also the number of states in the unit cell). In this definition, the DOS is normalized such that the total number of states, $\int_{-\infty}^{\infty} \mathcal{D}(E) dE = 1$. In principle, we could apply this definition to our three systems. However, due to the different dimensions, we will obtain very different Van Hove singularities within the DOS. The DOS of a finite GNR would, for instance, only consist of delta functions. Therefore, only if one takes the limit to infinite system size one would expect the DOS of the finite ribbon to converge to the DOS of graphene. This DOS, therefore, is not a good tool to compare the three systems.

One way to circumvent the problem is to regularize the Van Hove singularities by convoluting the DOS with a decreasing symmetric function that is normalized to one. This procedure, basically attributes a certain width to every value in the DOS. This makes the Van Hove singularities spread out and lose their singular character, turning them into finite sized peaks instead. One can choose different functions for this convolution. We will use the Lorentzian and define the Lorentzian DOS as

$$\mathcal{D}^{\Delta}(E) = \int \mathcal{D}(E') L^{\Delta}(E - E') dE', \quad (\text{B.7})$$

where $L^{\Delta}(x)$ is the Lorentzian of width Δ , given by

$$L^{\Delta}(x) = \frac{1}{\pi} \frac{\Delta/2}{(x)^2 + (\Delta/2)^2}. \quad (\text{B.8})$$

The Lorentzian DOS is a function that approaches the actual DOS in the limit $\Delta \rightarrow 0$. However, for non-zero Δ the Lorentzian DOS is an approximation of the DOS that should converge steadily for our different systems even though they are of different dimensionality.

A last difficulty is to calculate the Lorentzian DOS for the systems with a continuous spectrum, i.e. graphene and the GNRs with a periodic boundary condition. We would first have to do the integral in Eq. (B.6) to calculate the DOS. This integral is difficult to perform for graphene because the analytical

solution is a complicated function. For the spectrum of the GNRs with a periodic boundary condition this is completely impossible, as we do not even have an analytical solution. For the finite GNRs, however, the DOS is easily given because it is just a sum of delta functions. In order to calculate the DOS for the continuous spectra, we discretize by sampling a set of energies from the spectrum. We have to make sure that this set is not biased towards certain types of states. Because the states are evenly distributed with respect to the \mathbf{k} vectors (graphene) or \mathbf{k}^{1d} vectors (GNRs with a periodic boundary condition), we sample by choosing an evenly distributed list of \mathbf{k} - or \mathbf{k}^{1d} vectors and calculate the corresponding energies. Then, we calculate the DOS as if the spectrum consisted just of the sampled energies. The DOS thus becomes a sum of delta functions localized at the sampled energies. Obviously, the larger the discretization set, the better is the final result. The Lorentzian DOS now simply becomes a sum of Lorentzians localised at the sampled energies.

In Fig. B.1 we plot $\mathcal{D}^\Delta(E)$ for different systems and system sizes. All the underlying spectra are calculated using exponentially decaying orbital-hopping and overlap parameters with $t_0 = -2.5$ eV, $s_0 = 0.36$, $\kappa = 1.5$, and $\epsilon_0 = -2.76$. These are parameters slightly different from the ones used in the rest of this thesis but they do not show a big difference in result with the other parameters. We used a Lorentzian widening of $\Delta = 0.1$ eV. In Fig. B.1a we can see that the longer we make a finite GNR, the more the Lorentzian DOS starts to look like the Lorentzian DOS of the GNR with a periodic boundary condition. The large peak around the Fermi energy corresponds to the edge states of the GNR. Notice also the signatures of the Van Hove singularities left and right of the Fermi energy. These are due to confinement in one direction, but are not real singularities because we are plotting the Lorentzian DOS instead of the exact DOS. The periodic modulation of the smallest finite GNR is an artifact of our procedure. In Fig. B.1b we can see that also for armchair GNRs the Lorentzian DOS of a finite GNR approaches that of the GNR with a periodic boundary condition. The peak at the Fermi energy is due to the edge states on the zigzag termination at the ends of the armchair ribbon. We see that for longer AGNRs these states become less pronounced. We also see the signatures of the Van Hove singularities to the right and left of the Fermi energy due to confinement. In Fig. B.1c, we see that the wider a ZGNR with a periodic boundary condition is, the more its Lorentzian DOS approaches that of graphene. In addition the edge states become less significant as the ribbon gets wider. We can also observe that the signatures of the Van Hove singularities that are due to the confinement increase in density but become less pronounced when the ribbon becomes wider because the number of bands increases. Fig. B.1d shows that this holds also for the AGNRs.

In conclusion, we can say that the Lorentzian DOS of finite GNRs approaches that of GNRs with a periodic boundary condition with increasing GNR length and that the Lorentzian DOS of GNRs with periodic boundary conditions approaches that of graphene with increasing width. If the

Lorentzian DOS approaches the graphene Lorentzian DOS, the DOS in the limit of large system size will be equal to that of graphene for all the systems.

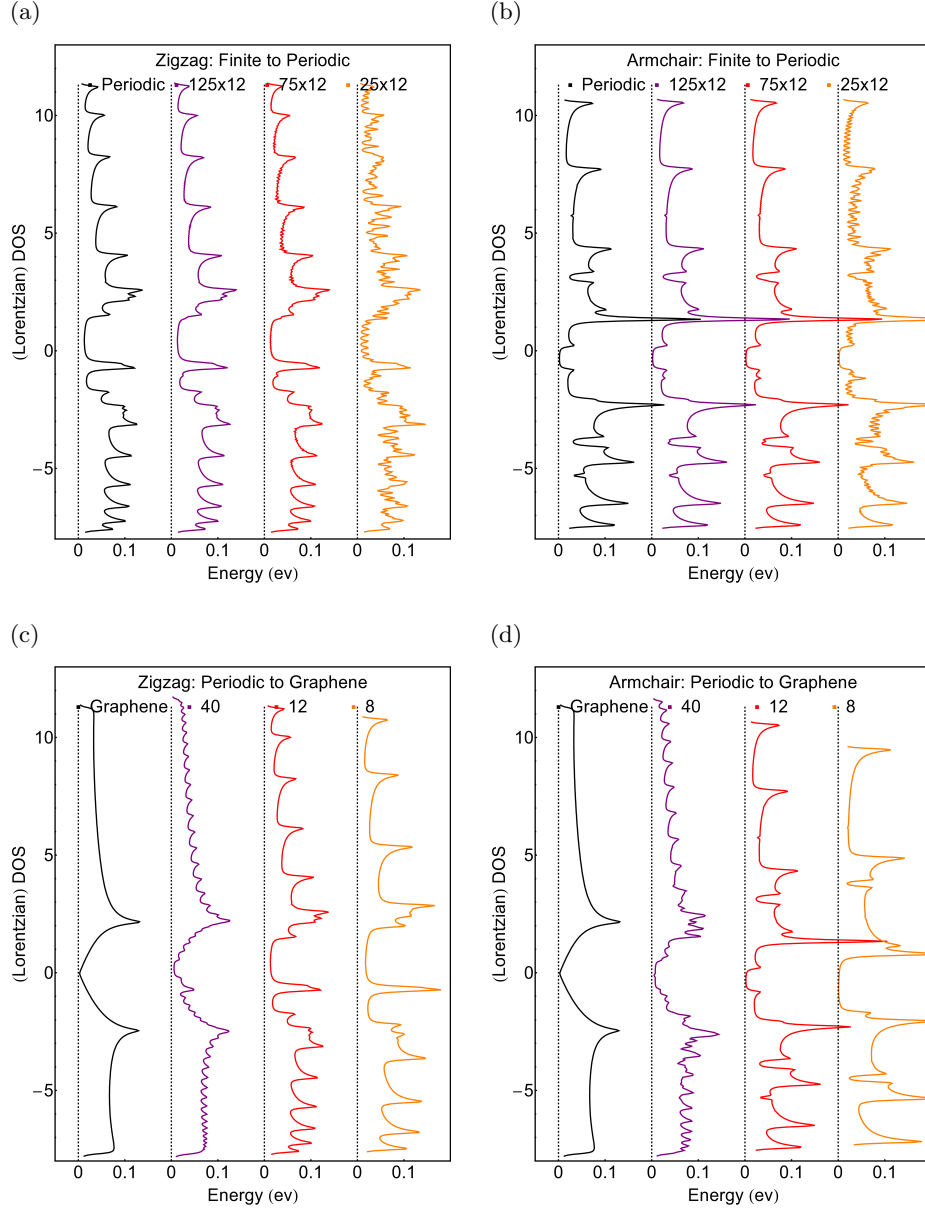


Figure B.1: DOS calculated with Lorentzian broadening of $\Delta = 0.1$ eV . All calculations were based on non-orthogonal parameters with exponential decay using $t_0 = -2.5$ eV, $s_0 = 0.36$, $\kappa = 1.5$, and $\epsilon_0 = -2.76$. (a) A ZGNR of width $N = 12$, from left to right: period, length $N^u = 25, 75, 125$ (as defined in Sec. 3.2). (b) Similar to (a), but for an AGNR of width $N = 12$ (c) The width of a zigzag GNR with a periodic boundary condition is increased from right to left with $2N_u$ equal to 8, 12 and 40, respectively. The most left curve is for graphene (d) Similar to (c), but for an armchair GNR with a periodic boundary condition.

Appendix C

Bloch's theorem for lattice-preserving deformations

In general after a deformation we have to find the spectrum of a deformed hamiltonian given by

$$\hat{\mathbf{H}}_{\mathbf{F}} = -\frac{\hbar}{2m}\nabla^2 + \sum_i V(\mathbf{F}(\mathbf{r}_i) - \mathbf{r}). \quad (\text{C.1})$$

Here \mathbf{F} is the deformation, i runs over the lattice sites and \mathbf{r} is the position. Because a deformed Hamiltonian is not strictly periodic anymore Bloch's theorem doesn't directly apply. We can however use a corollary of Bloch's theorem which applies to lattices after a specific type of deformation, which we will call a lattice preserving deformation. We will show that although the deformed hamiltonian does not commute with the ordinary translation operator $\hat{\mathbf{T}}$ it will commute with another type of translation operator $\hat{\mathbf{T}}_{\mathbf{F}}$. We first define the ordinary translation operator $\hat{\mathbf{T}}$ such that $\hat{\mathbf{T}}\psi(\mathbf{r}) = \psi(\mathbf{r} + \mathbf{a})$, with \mathbf{a} the 1D lattice vector. A deformation $\mathbf{F}(\mathbf{r})$ is called lattice preserving with respect to the translation operator $\hat{\mathbf{T}}$ if for all \mathbf{r}_1 and \mathbf{r}_2 :

$$|\mathbf{F}(\mathbf{r}_1) - \mathbf{F}(\mathbf{r}_2)| = |\mathbf{F}(\mathbf{r}_1 + \mathbf{a}) - \mathbf{F}(\mathbf{r}_2 + \mathbf{a})|. \quad (\text{C.2})$$

Examples of this kind of transformation are all the linear transformations, e.g. rotations, uniform strains. But this transformation is more general and also entails the bending deformation that satisfies the discrete rotational symmetry. Another deformation that satisfies this definition is a deformation where the edge atoms of a ribbon are shifted such that they have a shorter bond-length. This is in reality actually the case for GNRs as remarked earlier. Lets also define a transformation function $\mathbf{T}_{\mathbf{F}}(\mathbf{r}) = \mathbf{F}(\mathbf{F}^{-1}(\mathbf{r}) + \mathbf{a})$. Using this function we define a transformation operator, called the deformed translation, that acts

in the following way on a wave function,

$$\hat{\mathbf{T}}_{\mathbf{F}}\psi(\mathbf{r}) = \psi(\mathbf{F}(\mathbf{F}^{-1}(\mathbf{r}) + \mathbf{a})) = \psi(\mathbf{T}_{\mathbf{F}}(\mathbf{r})). \quad (\text{C.3})$$

Now it is important to observe that from the definition of a lattice preserving \mathbf{F} , Eq. (C.2), it follows that the function $\mathbf{T}_{\mathbf{F}}$ is an isometry. This follows from the fact that $\mathbf{F}(\mathbf{r} + \mathbf{a}) = \mathbf{T}_{\mathbf{F}}(\mathbf{r})$. Because $\mathbf{T}_{\mathbf{F}}$ is an isometry we can write $\mathbf{T}_{\mathbf{F}} = \mathbf{A}\mathbf{r} + \mathbf{b}$, for some orthogonal matrix \mathbf{A} and vector \mathbf{b} . The most important observation now is that the deformed translation commutes with the deformed hamiltonian, assuming that the potentials are circular symmetric. We'll first show that the $\hat{\mathbf{T}}_{\mathbf{F}}$ commutes with the potential energy part of the hamiltonian:

$$\begin{aligned} \hat{\mathbf{T}}_{\mathbf{F}} \left[\sum_i V(|\mathbf{F}(\mathbf{r}_i) - \mathbf{r}|) \right] \psi(\mathbf{r}) &= \\ \left[\sum_i V(|\mathbf{F}(\mathbf{r}_i) - \mathbf{F}(\mathbf{F}^{-1}(\mathbf{r}) + \mathbf{a})|) \right] \psi(\mathbf{F}(\mathbf{F}^{-1}(\mathbf{r}) + \mathbf{a})) &= \\ \left[\sum_i V(|\mathbf{F}(\mathbf{r}_i + \mathbf{a}) - \mathbf{F}(\mathbf{F}^{-1}(\mathbf{r}) + \mathbf{a})|) \right] \hat{\mathbf{T}}_{\mathbf{F}}\psi(\mathbf{r}) &= \\ \left[\sum_i V(|\mathbf{F}(\mathbf{r}_i) - \mathbf{r}|) \right] \hat{\mathbf{T}}_{\mathbf{F}}\psi(\mathbf{r}). \end{aligned}$$

Here in the second to third line we used that the original lattice is preserved after a shift of \mathbf{a} and in the third to fourth line we used the fact that \mathbf{F} satisfies Eq. (C.2). Next we can show that $\hat{\mathbf{T}}_{\mathbf{F}}$ commutes with ∇^2 :

$$\begin{aligned} \hat{\mathbf{T}}_{\mathbf{F}}[\nabla^2\psi(\mathbf{r})] &= \hat{\mathbf{T}}_{\mathbf{F}}[\nabla_i\nabla_i\psi(\mathbf{r})] = (\nabla_k\nabla_l\hat{\mathbf{T}}_{\mathbf{F}}\psi(\mathbf{r}))\nabla_i(\mathbf{T}_{\mathbf{F}}(\mathbf{r}))_k\nabla_i(\mathbf{T}_{\mathbf{F}}(\mathbf{r}))_l = \\ &= (\nabla_k\nabla_l\hat{\mathbf{T}}_{\mathbf{F}}\psi(\mathbf{r}))\nabla_i(A_{km}r_m + b_k)\nabla_i(A_{ln}r_n + b_l) = \\ &= (\nabla_k\nabla_l\hat{\mathbf{T}}_{\mathbf{F}}\psi(\mathbf{r}))A_{ki}A_{li} = (\nabla_k\nabla_l\hat{\mathbf{T}}_{\mathbf{F}}\psi(\mathbf{r}))\delta_{kl} = \nabla^2[\hat{\mathbf{T}}_{\mathbf{F}}\psi(\mathbf{r})]. \end{aligned}$$

Here we used the Einstein notation with solely lower indices, which is allowed because we keep the basis constant. From the first to second line we used the fact that $\mathbf{T}_{\mathbf{F}}$ is an isometry. In the third line we used the fact that \mathbf{A} is an orthogonal matrix. These two derivations demonstrate that the Hamiltonian and the deformed translation operator commute and are therefore simultaneously diagonalizable. The eigenstates of the deformed translation can be derived using Bloch's theorem. To see this we define a deformed wavefunction $\psi_{\mathbf{F}}$ such that

$$\psi_{\mathbf{F}}(\mathbf{r}) = \psi(\mathbf{F}(\mathbf{r})). \quad (\text{C.4})$$

Then $\hat{\mathbf{T}}_{\mathbf{F}}\psi(\mathbf{r}) = \hat{\mathbf{T}}\psi_{\mathbf{F}}(\mathbf{F}^{-1}\mathbf{r})$, so an eigenstate of $\hat{\mathbf{T}}_{\mathbf{F}}$ is an eigenstate of $\hat{\mathbf{T}}$ but evaluated at the point $\mathbf{F}^{-1}\mathbf{r}$. But these eigenstates we know as they are the standard Bloch states that are labeled by \mathbf{k} , where \mathbf{k} lies in the undeformed $1d$ BZ associated with the translation operator $\hat{\mathbf{T}}$. Therefore we can label the eigenstates of the deformed hamiltonian also in terms of these \mathbf{k} . They are given by,

$$\psi^{\mathbf{k}}(\mathbf{r}) = e^{i\mathbf{k}\cdot(\mathbf{F}^{-1}\mathbf{r})}u(\mathbf{F}^{-1}\mathbf{r}). \quad (\text{C.5})$$

In this way we map our eigenstates to the original undeformed reciprocal space. Note that for linear deformations \mathbf{F} this is unconventional as these deformed lattices have themselves a well defined reciprocal space, given by $\{\mathbf{F}^{-1}(\mathbf{k})\}$, where \mathbf{k} are in the original reciprocal space. However this procedure results in the same eigenstates and energies, only the labelling is different. When we make a tight-binding assumption we can further pin down the form of the eigenstate. In tight-binding we assume

$$\psi(\mathbf{r}) = \sum_{t,n} c_{t,n} \phi_n(\mathbf{R}'_t - \mathbf{r}) \quad (\text{C.6})$$

where n runs over the 1D unit cell and ϕ_n is the n -th localized wave function in the unit cell, and $\mathbf{R}'_t = \mathbf{F}(\mathbf{R}_t) = \mathbf{F}(t\mathbf{a})$ is the 1D bravais lattice. For this state to be an eigenstate it has to satisfy (Eq. C.5) and therefore $c_{t,n} = e^{it\mathbf{k}\cdot\mathbf{a}} c_{\mathbf{k},n}$, and we get

$$\psi^{\mathbf{k}}(\mathbf{r}) = \sum_{t,n} e^{it\mathbf{k}\cdot\mathbf{a}} c_{\mathbf{k},n} \phi_n(\mathbf{R}'_t - \mathbf{r}). \quad (\text{C.7})$$

Bibliography

- [1] K. S. Novoselov, A. K. Geim, S. V. Morozov, D. Jiang, Y. Zhang, S. V. Dubonos, I. V. Grigorieva, and A. A. Firsov. Electric field effect in atomically thin carbon films. *Science*, 306(5696):666–669, 2004.
- [2] A. K. Geim. Graphene: Status and prospects. *Science*, 324(5934):1530–1534, 2009.
- [3] M. Fujita, K. Wakabayashi, K. Nakada, and K. Kusakabe. Peculiar localized state at zigzag graphite edge. *Journal of the Physical Society of Japan*, 65(7):1920–1923, 1996.
- [4] Y. Son, M. Cohen, and S. Louie. Energy gaps in graphene nanoribbons. *Phys. Rev. Lett.*, 97:216803, Nov 2006.
- [5] X. Wang, Y. Ouyang, X. Li, H. Wang, J. Guo, and H. Dai. Room-temperature all-semiconducting sub-10-nm graphene nanoribbon field-effect transistors. *Phys. Rev. Lett.*, 100:206803, May 2008.
- [6] C. L. Kane and E. J. Mele. Size, shape, and low energy electronic structure of carbon nanotubes. *Phys. Rev. Lett.*, 78:1932–1935, Mar 1997.
- [7] V. M. Pereira and A. H. Castro Neto. Strain engineering of graphene’s electronic structure. *Phys. Rev. Lett.*, 103:046801, Jul 2009.
- [8] N. Levy, S. A. Burke, K. L. Meaker, M. Panlasigui, A. Zettl, F. Guinea, A. H. Castro Neto, and M. F. Crommie. Strain-induced pseudomagnetic fields greater than 300 tesla in graphene nanobubbles. *Science*, 329(5991):544–547, 2010.
- [9] Z. Qi, D. K. Campbell, and H. S. Park. Atomistic simulations of tension-induced large deformation and stretchability in graphene kirigami. *Phys. Rev. B*, 90:245437, Dec 2014.
- [10] M. Blees, P. Rose, A. Barnard, S. Roberts, and P. L. McEuen. graphene kirigami. Bulletin of the American Physical Society, 2014. Available at meetings.aps.org/link/BAPS.2014.MAR.L30.11.
- [11] World’s thinnest material stretches, bends, twists. *Sciencenews.org*.

- [12] P. Jacobse. Strain engineering graphene nanoribbons by scanning probe manipulation. Masters thesis, Utrecht University, 2014.
- [13] P. Koskinen. Graphene nanoribbons subject to gentle bends. *Phys. Rev. B*, 85:205429, May 2012.
- [14] A. H. Castro Neto, F. Guinea, N. M. R. Peres, K. S. Novoselov, and A. K. Geim. The electronic properties of graphene. *Rev. Mod. Phys.*, 81:109–162, Jan 2009.
- [15] M. O. Goerbig. Electronic properties of graphene in a strong magnetic field. *Rev. Mod. Phys.*, 83:1193–1243, Nov 2011.
- [16] J. Jung and A. H. MacDonald. Tight-binding model for graphene pi-bands from maximally localized wannier functions. *Phys. Rev. B*, 87:195450, May 2013.
- [17] M. Brandbyge, J. Mozos, P. Ordejón, J. Taylor, and K. Stokbro. Density-functional method for nonequilibrium electron transport. *Phys. Rev. B*, 65:165401, Mar 2002.
- [18] V. M. Pereira, A. H. Castro Neto, and N. M. R. Peres. Tight-binding approach to uniaxial strain in graphene. *Phys. Rev. B*, 80:045401, Jul 2009.
- [19] J. G. Aiken, J. A. Erdos, and J. A. Goldstein. On lwdin orthogonalization. *International Journal of Quantum Chemistry*, 18(4):1101–1108, 1980.
- [20] S. Reich, J. Maultzsch, C. Thomsen, and P. Ordejón. Tight-binding description of graphene. *Phys. Rev. B*, 66:035412, Jul 2002.
- [21] C. Bena and L. Simon. Dirac point metamorphosis from third-neighbor couplings in graphene and related materials. *Phys. Rev. B*, 83:115404, Mar 2011.
- [22] K. Wakabayashi, K. Sasaki, T. Nakanishi, and T. Enoki. Electronic states of graphene nanoribbons and analytical solutions. *Science and Technology of Advanced Materials*, 11(5):054504, 2010.
- [23] G. Z. Magda, X. Jin, I. Hagymási, P. Vancsó, Z. Osváth, P. Nemes-Incze, C. Hwang, L. P. Biró, and L. Tapasztó. Room-temperature magnetic order on zigzag edges of narrow graphene nanoribbons. *Nature*, 514(7524):608–611, 2014.
- [24] C. Bena and G. Montambaux. Remarks on the tight-binding model of graphene. *New Journal of Physics*, 11(9):095003, 2009.
- [25] L. Brey and H. A. Fertig. Electronic states of graphene nanoribbons studied with the dirac equation. *Phys. Rev. B*, 73:235411, Jun 2006.

- [26] F. Guinea, M. I. Katsnelson, and A. K. Geim. Energy gaps and a zero-field quantum hall effect in graphene by strain engineering. *Nature Physics*, 6(1):30–33, 2009.
- [27] F. de Juan, M. Sturla, and M. A. H. Vozmediano. Space dependent fermi velocity in strained graphene. *Phys. Rev. Lett.*, 108:227205, May 2012.
- [28] M. R. Masir, D. Moldovan, and F. M. Peeters. Pseudo magnetic field in strained graphene: Revisited. *Solid State Communications*, 175176(0):76 – 82, 2013. Special Issue: Graphene V: Recent Advances in Studies of Graphene and Graphene analogues.
- [29] P. Ghaemi, S. Gopalakrishnan, and S. Ryu. Stability of edge states in strained graphene. *Phys. Rev. B*, 87:155422, Apr 2013.
- [30] L. Brey and H. A. Fertig. Edge states and the quantized hall effect in graphene. *Phys. Rev. B*, 73:195408, May 2006.
- [31] NIST Digital Library of Mathematical Functions. <http://dlmf.nist.gov/>, Release 1.0.9 of 2014-08-29.
- [32] J. Wurm. PhD thesis.
- [33] D. Zhang and T. Dumitric. Effective-tensional-strain-driven bandgap modulations in helical graphene nanoribbons. *Small*, 7(8):1023–1027, 2011.
- [34] D. Zhang, G. Seifert, and K. Chang. Strain-induced pseudomagnetic fields in twisted graphene nanoribbons. *Phys. Rev. Lett.*, 112:096805, Mar 2014.